Alma Mater Studiorum – Università di Bologna

DOTTORATO DI RICERCA IN GEOFISICA

Ciclo XXX

Settore Concorsuale: **04/A4**

Settore Scientifico Disciplinare: **GEO/10**

Modelling ash cloud dispersion and the impact of ash aggregation during volcanic eruptions

Presentata da: **Matthieu Poret**

Coordinatore Dottorato

Prof. Nadia Pinardi

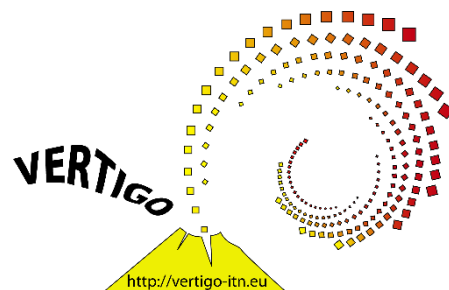Supervisore

Dr. Antonio Costa (INGV)

Co-supervisore

Prof. Michele Dragoni (UNIBO)

Esame finale anno 2018

Department of Geophysics

University of Bologna

Bologna, Italy

Modelling ash cloud dispersion and the impact of ash aggregation during volcanic eruptions

Matthieu Poret

Ph.D. supervision

Supervisor: Dr. Antonio Costa   *INGV – Bologna*
Co-supervisor: Prof. Michele Dragoni   *University of Bologna*

Examination

Reviewer: Dr. Giovanni Macedonio   *INGV – OV – Naples*
Reviewer: Dr. Larry Mastin   *USGS – Vancouver (USA)*

Jury

Dr. Alberto Amigliato   *University of Bologna*
Dr. Umberto Giostra   *University of Bologna*
Dr. Andrea Tallarico   *University of Bari*

" La Recherche ? C'est cartographier le terrain de la Vie ! "

Margaux Leygonie

Riassunto

Il continuo miglioramento nella caratterizzazione dei processi eruttivi è tipicamente ottenuto attraverso l'integrazione di analisi di dati di campagna, strumenti di telerilevamento, esperimenti di laboratorio e modelli numerici. Da un punto di vista computazionale, l'interdipendenza dei principali parametri vulcanologici rende ardua la valutazione della dispersione e della sedimentazione del tefra, a partire dai quali vengono stimati il tasso di eruzione di massa, la massa totale eruttata e la distribuzione granulometrica totale (TGSD). Questa tesi mira a vincolare meglio la valutazione dei parametri della sorgente eruttiva (ESP) e in particolare della TGSD, di solito derivata utilizzando solo dati dall'analisi dei campioni di campo. In particolare la stima della frazione di cenere finissima (cioè <30 μm), all'interno del TGSD, soffre comunemente della mancanza di dati di campo distale, specialmente per le eruzioni basaltiche che contengono poco materiale fine. Inoltre, l'aggregazione delle particelle vulcaniche influenza la dispersione delle ceneri e quindi la deposizione. Sebbene le simulazioni numeriche possano tenere conto dell'aggregazione delle ceneri, hanno bisogno di una TSGD accurato come input. Qui, utilizzo il modello FALL3D insieme a dati satellitari e di campagna per quantificare i) la frazione di cenere finissima e l'effetto sui risultati della simulazione e ii) l'occorrenza e la rilevanza nei processi di trasporto dell'aggregazione delle ceneri. Innanzitutto, mi concentro sull'integrazione dei dati di campo e da satellite per stimare meglio la TGSD e in particolare la frazione di PM_{10}. La metodologia, che integra le misurazioni di campo e i dati satellitari per migliorare la caratterizzazione del TGSD iniziale, viene applicata prima al parossismo dell'Etna del 23 febbraio 2013 ed in secondo luogo all'eruzione dell'Etna del 23 novembre 2013. Queste due eruzioni sono state considerate perché hanno beneficiato del trasporto dovuto all'azione di venti nord-orientali che hanno disperso il tefra verso la regione Puglia (Italia meridionale, ~ 410 km dalla sorgente), consentendo una raccolta di campioni fino a zone molto distali. Poi sono stati studiati i processi di aggregazione delle ceneri che hanno caratterizzato l'eruzione esplosiva di La Soufrière Saint Vincent il 26 aprile 1979. Durante questo evento, è stata osservata una significativa frazione di ceneri aggregate che ha contribuito a una prematura ricaduta del tefra dalla bocca eruttiva all'Isola di Bequia (36 km a sud). Ho selezionato questa eruzione per studiare l'effetto dell'uso di vari TGSD insieme a diversi schemi di aggregazione sul risultante carico di tefra e sulla dispersione di cenere.

Abstract

Improvements for characterizing eruption processes are made commonly through field data analysis, remote-sensing instruments, lab experiments and numerical models. From a computational point of view, the inter-dependency of the main volcanological parameters makes challenging the assessment of tephra dispersion and sedimentation, from which mass eruption rate, total erupted mass, and Total Grain-Size Distribution (TGSD) are typically estimated. This thesis aims at better constraining Eruption Source Parameters (ESP) and in particular the TGSD, usually derived from field sample analysis only. The estimation of very fine ash (i.e. < 30 μm) fraction, within the TGSD, commonly suffers from the lack of distal field data, especially for basaltic eruptions, which contain a small fraction of fine ash. Besides, particle-particle aggregation affects ash dispersal and deposition. Although numerical simulations can account for ash aggregation, they need an accurate TSGD as input. Here, I report the use of the FALL3D model together with airborne and ground-based data in order to quantify i) the very fine ash and the effect on the simulation results and ii) the occurrence of ash aggregation during ash transport. I focus on the integration of field and satellite data to better estimate the TGSD and the PM_{10} fraction especially. The methodology, which integrates the field, ground-based and satellite measurements to improve the characterization of the initial TGSD, is applied first to the 23rd February 2013 Etna paroxysm, then to the 23rd November 2013 Etna eruption. These two eruptions were considered because they benefited from north-easterly winds which dispersed the tephra towards the Puglia region (southern Italy; ~410 km from source), allowing collection of field samples to very distal areas. Then, I studied ash aggregation processes characterizing the explosive eruption of La Soufrière Saint Vincent on 26th April 1979. During this event, a significant aggregate fraction was observed contributing to premature tephra fallout from the vent to Bequia Island (36 km southwards). This eruption was selected to investigate the effect of various TGSD together with different aggregation schemes on the resulting tephra loading and ash dispersal.

Preamble

This study reports the results obtained using both volcanic plume (FPlume) and tephra dispersal models (FALL3D) to numerically reconstruct the main eruption features (e.g. bulk tephra loading, airborne ash spreading, Total Grain-Size Distribution – TGSD and ash aggregation). The work brings together studies based on the quantification of fine ash fraction and the effect of ash aggregation on the tephra dispersal and sedimentation. Chapter I is a review of the literature about tephra characterization and tephra hazards. Chapter II is an overview of the approach used for tephra dispersal models. Chapter III describes the available observational data (e.g. field samples, ground-based and satellite remote sensing systems) that can be used to solve an inverse problem aimed to estimate the Eruption Source Parameters (ESP). Chapter IV is a study that aims at integrating field and satellite measurements for characterizing the TGSD and thereby the airborne ash fraction through numerical simulations. Chapter IV is under review for publication to Journal of Geophysical Research – Solid Earth. Chapter V proposes a method to reconstruct the TGSD by means of field, weather radar and satellite data, evaluating quantitatively the airborne ash mass. Chapter V is accepted for publication to Atmospheric Chemistry and Physics Discussions journal. Chapter VI studies ash aggregation implemented within numerical models. Chapter VI is published in Journal of Volcanology and Geothermal Research. Chapter VII reports the findings of this study and highlights the outlook for future work. Only minor changes have been made for adapting to the overall structure of the manuscript.

1. **Poret M.**, Costa A., Andronico D., Scollo S., Gouhier M. and Cristaldi A. Modelling eruption source parameters by integrating field, ground-based and satellite-based measurements: The case of the 23rd February 2013 Etna paroxysm. *J. Geophys. Res. – Solid Earth, Accepted pending revision.*

2. **Poret M.**, Corradini S., Merucci L., Costa A., Andronico D., Vulpiani G., Scollo S., Montopoli M. and Freret V. Magma fragmentation assessed from field, ground-based and satellite data: Application to the 23rd November 2013 Etna paroxysm. *Atmos. Chem. Phys. Discuss., In press.* doi:10.5194/acp-2017-1146

3. **Poret M.**, Costa A., Folch A. and Martí A. Modelling tephra dispersal and ash aggregation: The 26th April 1979 eruption, La Soufrière St. Vincent. *J. Volcanol. Geotherm. Res.* 347, 207–220. doi:10.1016/j.jvolgeores.2017.09.012

Acknowledgments

I would like to thank my supervisor Dr. Antonio Costa for giving me the opportunity to carry out my research studies within the ITN VERTIGO project. I enjoyed every single day being aware about how lucky I was to share such large-scale experiences with you the last three years. I also acknowledge my co-supervisor Prof. Michele Dragoni for having helped me providing advice and feedback during my thesis.

Je remercie Margaux, mon amie, mon équipière, mon aventurière, ma Red, pour m'avoir accompagné et surtout m'avoir écouté sans jamais faillir depuis que tu es à mes côtés ! Tu as su faire preuve de patience et d'organisation pour optimiser (organiser??) notre expérience qu'on continue ensemble.

I would like to warmly thank the entire VERTIGO group that offered the full experience for researchers all around the world. Indeed, thank you Ulli, Diego and Greta for having wished for such a network! VERTIGO does not only mean "Volcanic ash: fiEld, expeRimenTal and numerIcal investiGations of prOcesses during its lifecycles" but also Basti, Stefano, Andreas, Vale, Pablo, Inga, Joalie, Katrin, Ines, Pierre-Yves, Antonio, Ka Lok!

Great thanks also to the volcanologists I met all around the world, Marco, Boris, Antonio, Jon, Costanza, Tullio, Jacopo, Pierre, Yujiro, Stefano, Luca, Mark, Claire, Antonio and so many others who showed me this amazing world.

A special thanks goes to INGV (Bologna section), Dr. Francesca Quareni, for having hosted me these last three years and supported me for travelling around the world. Thanks to INGV–OE (Catania section), Daniele Andronico and Simona Scollo for having hosted me during 1 month of secondment offering me the possibility to discover research near an active volcano. Thanks to the Civil Protection Department (Rome), Drs. Mauro Rosi, Stefano Ciolli, Gianfranco Vulpiani, Antonio Ricciardi and Damiano Piselli for having hosted me in your department for a month of training. The team completed by Domenico Mangione and Luigi Coppola taught me for example on how to share a real coffee.

Thanks to the 80-90's department of the INGV of Bologna, i.e. Letizia, Julie & Carmine, Valentina, Brunella, Francesca, Giulia, Tahira, Pablo, Davide, Paolo, Simone and Sarfraz for having shared all these moments with me inside and outside the institute.

I would like to acknowledge Dr. Giovanni Macedonio (INGV–OV, Naples, Italy) and Dr. Larry Mastin (USGS, Vancouver, USA) for having accepted to review my thesis manuscript.

Table of Contents

List of Figures

List of Tables

List of Notations

Notation	Definition	Unit
AAM:	Airborne Ash Mass	kg
AC	Ash Cloud	
ADS	Advection, Diffusion and Sedimentation	
AERONET:	AErosol RObotic NETwork	
AOD	Aerosol Optical Depth	dimensionless
a.s.l.	Above sea level	km
BPT	Buoyant Plume Theory	
BTD	Brightness Temperature Difference	
ECMWF	European Center for Medium-range Weather Forecasts	
ESP	Eruption Source Parameters	
IC	Ice/gas Cloud	
INGV – OE	Istituto Nazionale di Geofisica e Vulcanologia – Osservatorio Etneo	
GSD	Grain-Size Distribution	
L-band	L-band Doppler radar – VOLDORAD 2B	
MER	Mass Eruption Rate	kg/m^2
MOCAGE	MOdèle de Chimie Atmosphérique à Grande Echelle	
MSG	Meteosat Second Generation	
NAME	Numerical Atmospheric-dispersion Modelling Environment	
NASA	National Aeronautics and Space Administration	
NSEC	New South-East Crater	
OPGC	Observatoire de Physique du Globe de Clermont-Ferrand	

PHOTONS	PHotométrie pour le Traitement Opérationnel de Normalisation Satellitaire	
PM_{10}	Particle Matter below 10 µm	µm
PM_{20}	Particle Matter below 20 µm	µm
PSD	Particle-Size Distribution	
RMSE	Root Mean Square Error	dimensionless
SEVIRI	Spinning Enhanced Visible and Infrared Imager	
TEM	Total Erupted Mass	kg
TGSD	Total Grain-Size Distribution	
TIR	Thermal InfraRed	
TTest	Student T test	dimensionless
UTC	Coordinated Universal Time	hh:mm
VAAC	Volcanic Ash Advisory Center	
VATD	Volcanic Ash Transport and Dispersion	
Vis	Visible	
wt%	Percentage in weight	%
X-band	X-band weather radar	

Chapter I – Introduction

I.1   Eruption style

In volcanology, eruption is a common phenomenon occurring through various styles and intensities [Walker, 1973; 1980]. While the hot spot volcanoes (e.g. Kilauea in Hawai'i or Piton de la Fournaise in Reunion Island) are characterized by effusive eruptions with low viscous lava flows and gas plumes, the explosive eruptions are signatures of composite volcanoes and high magma viscosities (e.g. Vesuvius or Etna in Italy, La Soufrière Saint Vincent in West Indies). Although the latter can emplace lava flows, they are well-known for producing volcanic plumes by injecting the erupted material (hereinafter tephra) within the atmosphere. The eruption styles are classified from Hawaiian to Plinian following the scheme proposed by Walker [1980] and Pyle [1989]. Figure I.1 summarizes the associated common eruption features from the magma chamber (#11), the projection of volcanic bombs in the very proximal area (#5) to the tephra dispersion with deposition downwind (#4).
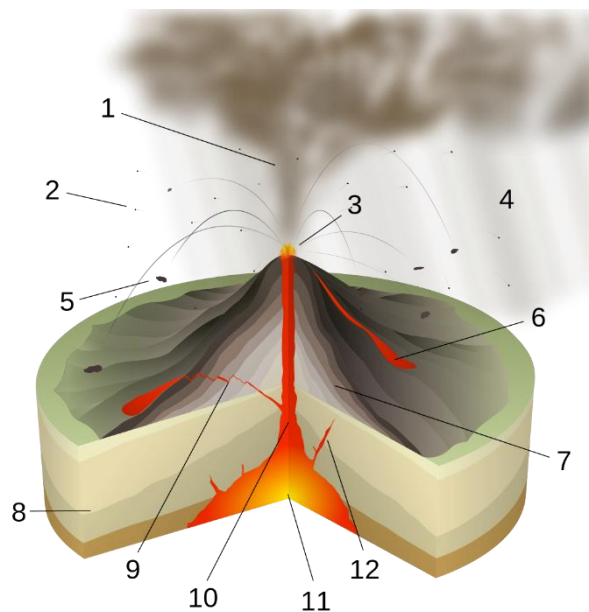
Figure I.1: Scheme of an explosive volcano and its products. 1. Ash plume, 2. Lapilli, 3. Lava fountain, 4. Ash, 5. Bomb, 6. Lava flow, 7.Erupted material layers, 8. Stratum, 9. Sill, 10. Conduit, 11. Magma chamber, 12. Dyke. [Wikimedia Commons]

I.2   Tephra classification

Tephra is produced from the magma fragmentation [Dingwell, 1996] as the results of a rapid ascension towards the surface of the melted mixture leading to a magma decompression in the conduit and the gas over-pressurization [Melnik et al., 2004]. Regarding the grain-size (i.e. diameter $- d$) of the fragmented magma and lithic, we can distinguish volcanic blocks or bombs

(i.e. $d \geq 64$ mm or $\Phi \leq -6$) from lapilli (i.e. $2 \leq d \leq 64$ mm or $-1 \geq \Phi \geq -6$) or ash (i.e. $d < 2$ mm or $\Phi > -1$). Among the broad term of ash, it is worth distinguishing coarse (i.e. $1 \leq d < 2$ mm or $0 \geq \Phi > -1$), fine (i.e. 30 µm $\leq d < 1$ mm or $5 \geq \Phi > 0$) and very fine ash (i.e. $d < 30$ µm or $\Phi > 5$) [e.g. Rose and Durant, 2009; Poret et al., 2017; 2018]. The grain-size spectrum is summarized in Figure I.2 through the two different units used in volcanology. In fact, although the metric units are used in some cases, the particle-sizes are typically expressed in Φ-units [Krumbein, 1934] by the following relationship:

$$d = 2^{-\Phi}$$

(I.1)

where d is expressed in mm. Although the largest objects follow a ballistic trajectory, such classification aims at better describing how the released material behaves from the source towards distal areas [Rose et al., 2001; 2003]. Indeed, lapilli and ash are conveyed upwards within the plume through the ambient air and the volcanic mixture until a point from which the atmospheric environment (e.g. wind speed, wind direction, wind shear, temperature, and air moisture) takes the lead of the particle transport by dispersing particles downwind [e.g. Costa et al., 2013]. Particle properties (i.e. density – ρ, shape, and d) are controlling the settling velocity leading to a sorted deposition with distance [Durant et al., 2009; Watt et al., 2015]. According to the terminal fall velocity, lapilli and coarse ash, for example for a sub-Plinian eruption [e.g. Bonadonna and Costa, 2013; Costa et al., 2016a], are expected to fall within few minutes to hours near the source (i.e. tens of km), whereas the fine and very fine ash can remain into the atmospheric layers for days to months dispersing at continental or global scales [e.g. Folch, 2012]. In other words, volcanic eruptions can affect very local to global scale depending on the eruption intensity, magma fragmentation, and wind field.
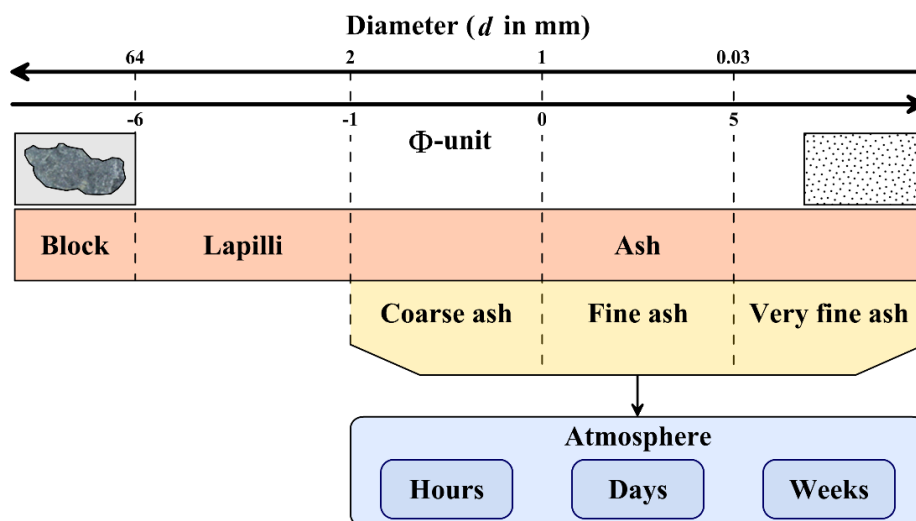
Figure I.2: Classification of the volcanic products.

I.3   Volcanic ash hazard

During an explosive eruption, volcanic hazards are related to tephra injection into the atmosphere. Tephra affects mostly proximal (i.e. within tens of km) and medial (i.e. first hundreds of km) but also distal areas. Deposition and accumulation of tephra can cause roof collapses [e.g. Macedonio and Costa, 2012], be remobilized by water producing lahars [e.g. Lecointre et al. 2004], damage infrastructures (e.g. electrical systems; Wilson et al. [2012]), disrupt communications and transportation (e.g. loss of visibility, roads, railways, runways; Guffanti et al. [2009]), contaminate water-supply systems, affect the environment [Ayris and Delmelle, 2012], damage agriculture [Wilson et al., 2011] and affect respiratory system [Horwell et al., 2007; 2013; 2017; Rose and Durant, 2009; Andronico and Del Carlo, 2016; Tomašek et al., 2016].

In addition, the large atmospheric residence time of the very fine ash and volcanic aerosols affects aviation hazards and climate. Indeed, the release of a large quantity of gas (e.g. H_2O, SO_2, H_2SO_4) and ash (e.g. PM_{20}, PM_{10}) into the atmosphere is now well-known to affect aviation by damaging fuselages, turbine blades, navigation instruments and by melting in high-bypass jet turbines [Casadevall, 1994; Casadevall et al., 1999; Bonadonna et al., 2012]. Such effects demonstrate the necessity for improving ash plume characterization in terms of ash concentration and plume dispersion to prevent potential ash encounters, as testified by several cases worldwide in the last decades [Prata, 1989a; Grindle and Burcham, 2003; Guffanti et al., 2010] and more recently with the 2010 Eyjafjallajökull eruption [Folch et al., 2012] and the 2011 Cordón-Caulle eruption [e.g. Folch et al., 2014; Bonadonna et al., 2015a; 2015b].

Besides aviation, the injection of volcanic ash or gas (e.g. sulphate aerosols) into the stratosphere has implications on the climate by modifying the radiative forcing for months to years [Robock, 2000; Kravitz et al., 2010], as in the 1991 Pinatubo and 2008 Okmok eruptions.

The volcanic hazards mentioned above motivate the development of numerical tools to forecast the tephra dispersal and deposition in order to mitigate such risks. Tephra dispersal models were designed for such purposes by computing the transport and consequently the deposition [Folch, 2012] making use of input parameters (e.g., meteorological conditions, Eruption Source Parameters – ESP). ESP include the eruption starts and duration, the column height, the Mass Eruption Rate (MER), which can be estimated from column height [e.g. Costa et al., 2016b], and the Total Grain-Size Distribution (TGSD), which includes the very fine ash fraction (i.e. PM_{20} and PM_{10}). Considering there is no operational single-instrument or method capable to describe fully the volcanic eruption processes, track the plume and assess the ESP, the estimation of ESP values can only be obtained through an integrated approach. In fact, during a volcanic crisis, alerting air traffic control centres to volcanic ash clouds is done worldwide by nine VAACs (Volcanic Ash Advisory Centers), which use operational satellite retrievals [e.g. Witham et al., 2007] and Volcanic Ash Transport and Dispersion (VATD) models, such as

NAME (Numerical Atmospheric-dispersion Modelling Environment; Witham et al. [2007]) or MOCAGE (MOdèle de Chimie Atmosphérique à Grande Echelle; Sič et al. [2015]) for London and Toulouse VAACs, respectively. However, the VAAC models assume a standard grain-size distribution from a pre-existing eruption [Maryon et al., 1999]. Besides NAME and MOCAGE models, FALL3D [Costa et al., 2006; Folch et al., 2009] is also operational at the Buenos Aires and Darwin VAACs. For the first two models, the fine ash percentage likely to reach the distal cloud is arbitrarily taken as 5 wt%.

I.4   Magma fragmentation – Total Grain-Size Distribution

Eruptions are commonly classified by, among other things, Total Erupted Mass (TEM), which is usually retrieved from field measurements only by integrating the deposit coverage [Bonadonna and Costa, 2013]. However, such a method highly depends on the possibility to access and measure tephra deposits (e.g. atmospheric conditions, land/sea, slopes, urbanization or deposits contamination). In addition to the TEM, the field samples provide geolocalized particle Grain-Size Distribution (GSD) permitting the TGSD to be estimated [Bonadonna and Houghton, 2005; Bonadonna et al, 2015c]. In fact, TGSD is commonly reconstructed on the basis of field samples analysis only [Brazier et al., 1982; Bonadonna et al., 2002; Bonadonna and Phillips, 2003; Andronico et al., 2008a; 2008b; Scollo et al., 2013]. As a consequence, the field-derived TGSD (Figure I.3) highly depends on the sampling distance from the source [Andronico et al., 2014a; Costa et al., 2016a], the spatial distribution, and the density of samples [Bonadonna et al., 2015c; Spanu et al., 2016]. Although the TGSD is complex to accurately assess, it is worst for the fine particle classes, which suffer much more uncertainty [Bonadonna et al., 2011; 2015c]. These observations raise questions about the need for an integrated approach to better assess the TGSD by increasing the grain-size spectrum coverage. This aim motivates this study to use the field measurements together with other sensors, such as ground- and satellite-based instruments to better constrain the TGSD, and the other ESPs.

Before initiating any integrated approach to assess the TGSD, the field-derived TGSD can be reconstructed through general distributions (Figure I.3), which better account for the fine ash distribution [Costa et al., 2016a; 2017]. They also show how the presence of two sub-populations within the TGSD is a common feature for most eruptions when they are properly sampled up to distal regions. This study reconstructs the field-based TGSD through the sum of either two lognormal distributions (bi-Gaussian in Φ; hereinafter bi-Gaussian distribution) or two Weibull distributions (bi-Weibull in Φ; hereinafter bi-Weibull distribution) by the following equations:

$$f_{bi-Gaussian}(\Phi) = p\frac{1}{\sigma_1\sqrt{2\pi}}e^{-\frac{(\Phi-\mu_1)^2}{2\sigma_1^2}} + (1-p)\frac{1}{\sigma_2\sqrt{2\pi}}e^{-\frac{(\Phi-\mu_2)^2}{2\sigma_2^2}}$$

(I.2)

where Φ denotes particle diameters, p and (1-p) are the fractions of each sub-population, μ_1, μ_2 and σ_1, σ_2 represent, respectively, the mean and standard deviation of the two Gaussian distributions in Φ-units;

$$f_{bi-Weibull}(d) = q\frac{1}{n_1^{\frac{1}{n_1}}\Gamma\left(1+\frac{1}{n_1}\right)}\frac{1}{\lambda_1}\left[\frac{d}{\lambda_1}\right]^{n_1}e^{-\frac{1}{n_1}\left(\frac{d}{\lambda_1}\right)^{n_1}} +$$

$$(1-q)\frac{1}{n_2^{\frac{1}{n_2}}\Gamma\left(1+\frac{1}{n_2}\right)}\frac{1}{\lambda_2}\left[\frac{d}{\lambda_2}\right]^{n_2}e^{-\frac{1}{n_2}\left(\frac{d}{\lambda_2}\right)^{n_2}}$$

(I.3)

where, q and (1-q) are the fraction of each sub-population, λ_1, λ_2, and n_1, n_2 represent, respectively, the scale and shape parameters of the two distributions.

Tephra dispersal models use the input TGSD as discrete size bins. They can use the field-based TGSD which provides the fraction for each bin (or half bin) or the fraction derived from either the bi-Gaussian or bi-Weibull distributions estimated through the equations (I.2) and (I.3), respectively.
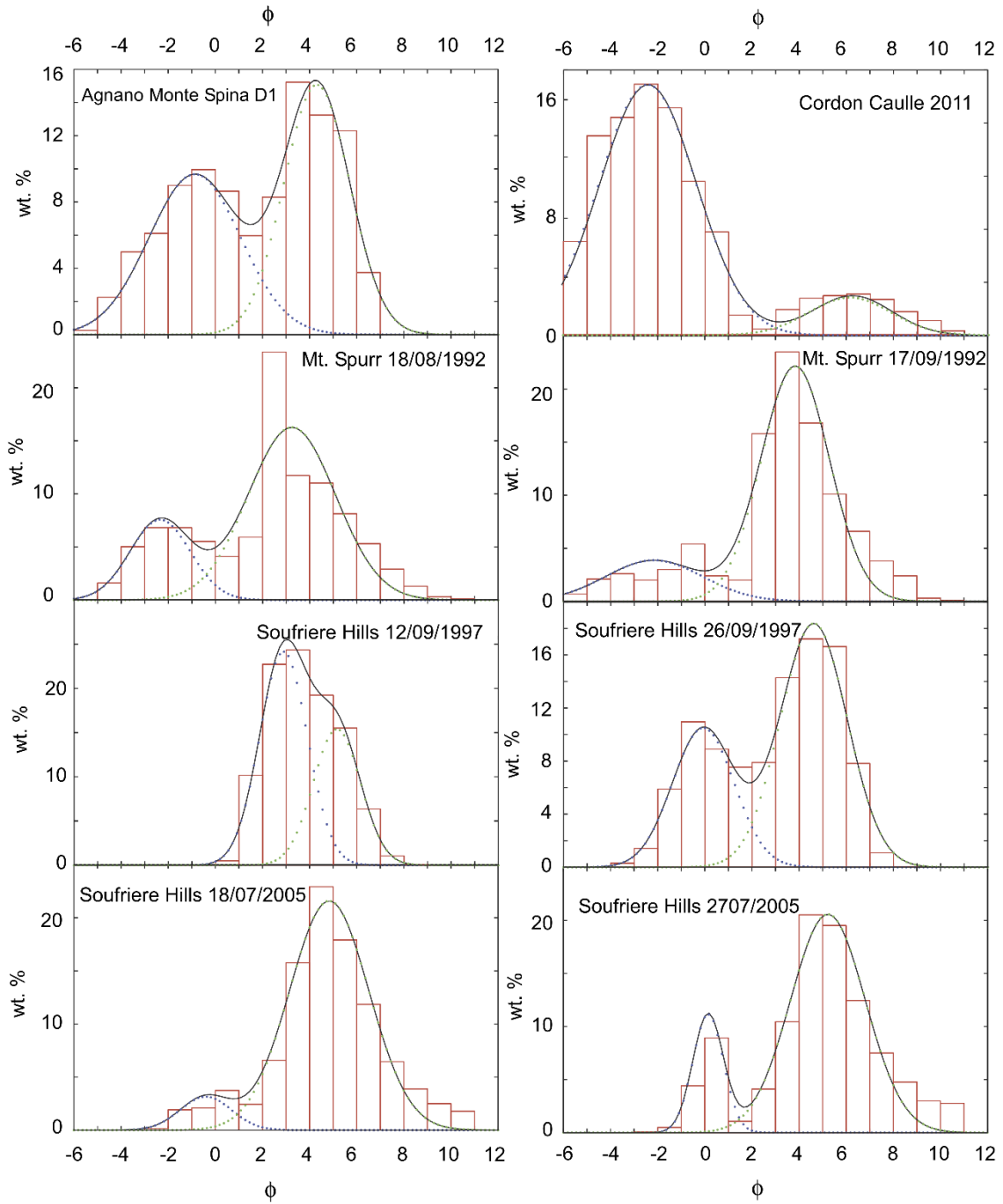
Figure I.3: Field-based TGSDs for different eruptions with the best-fitting distributions through two lognormal distributions (solid lines). [Costa et al., 2016a – Figure 2 modified]

I.5   Volcanic ash aggregation

Regarding the ash dispersal and deposition, the GSD together with the atmospheric conditions control the sedimentation processes and, consequently, the tephra residence time in the atmosphere [Watt et al., 2015]. However, it has been demonstrated that during eruptions, the fine and very fine ash particles typically interact, leading to aggregation through surface liquid layers [Costa et al., 2010; Van Eaton et al., 2012; Mueller et al., 2016; 2017a] or electrostatic forces [Taddeucci et al., 2011; Brown et al., 2012; Del Bello et al., 2015]. The attraction of the electrostatic forces are weaker than the liquid binder and are assumed to be negligible in presence of water [Folch et al., 2016; Mueller et al., 2016].

The term "ash aggregate" may refer to different volcanic products [Brown et al.; 2012, Van Eaton et al., 2012; Mueller et al., 2016]. According to the nomenclature, aggregates can be distinguished by considering the liquid water interaction that bonds the particles together. Under wet conditions, aggregates show compact texture and sub-spherical shape, and are called accretionary pellets (panel a in Figure I.4). Contrarily, dry conditions give particle clusters which are poorly bounded and are characterized by low densities and non-spherical morphologies (panel b in Figure I.4).

During an eruption, ash aggregation depletes the erupted mixture of fine ash resulting in premature fallout of the primary particles [Durant et al., 2009; Mastin et al., 2016]. Among the aggregation processes, particle-particle attraction plays a crucial role in the size and the stability of the aggregates [Mueller et al., 2017a; 2017b]. While electrostatic forces have a long-range attraction, capillary forces have shorter stronger ones, explaining the size and stability differences between the accretionary pellets and the particle clusters (Figure I.4). In addition, aggregate stability is controlled by the ratio between the dispersive and the attractive forces [Costa et al., 2010].
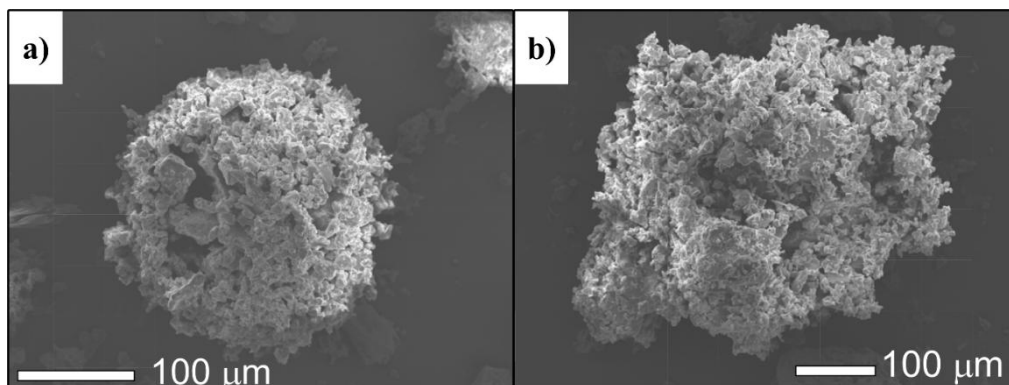
Figure I.4: a) Accretionary pellet, b) ash cluster. [Bonadonna et al., 2011 – Figure 7 modified]

The typical dominance of wet over dry conditions in volcanic plumes may justify the assumption to consider wet aggregation only. We consider water from both the atmosphere and the magma. Figure I.5 shows the different schemes for producing aggregates, highlighting the diversity of aggregates, which increase the complexity to compute ash aggregation within tephra dispersal models.

The efficiency of occurrence of ash aggregation depends on the magma type. In fact, a basaltic eruption injects typically < 5 wt% of ash, whereas a silicic produces > 30 wt% [Rose and Durant, 2009]. Moreover, aggregation can also increase the hazards in the proximal-medial areas by modifying the particle properties (e.g. density, shape and diameter). Indeed, aggregating particles an aggregate alters its properties, which results on premature fallout. From a computational point of view, tephra dispersal models neglecting aggregation may result in a significant tephra loading under-estimation in proximal areas accompanied by an over-estimation of the airborne ash mass at large distances from source [Folch et al., 2010; Brown et al., 2012; Van Eaton et al., 2012; Folch et al., 2016]. These observations argue the necessity to, first, better characterize the fine and very fine ash fractions potentially involved in the ash aggregation, and second, be able to capture the aggregation effects in tephra dispersal models.
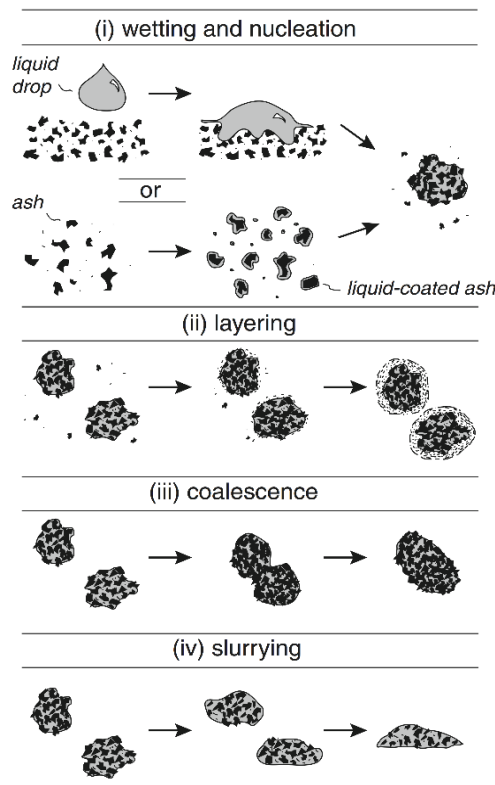
Figure I.5: Growth of liquid-bound ash aggregates: i) Nucleation of clusters during particle collisions through liquid drops (top) or liquid condensation. ii) Larger clusters capture smaller particles, generating concentric structure. iii) Cohesive collisions between similar primary clusters produce coalescent aggregates. iv) Slurring is obtained at high water content. [Van Eaton et al., 2012 – Figure 1 modified]

Chapter II – Tephra dispersal modelling

Tephra dispersal models are typically designed to simulate the transport and deposition of tephra associated with an explosive volcanic eruption for given meteorological conditions. Such models are widely used for assessing hazards. Model accuracy is of high importance, among others, to forecast tephra dispersal and deposition [Witham et al., 2007; Scollo et al., 2009], constrain the ESPs of past (or ongoing) volcanic events [Costa et al., 2014; Folch et al., 2014; Martí et al., 2016] and to assess volcanic hazards [Scollo et al., 2013; Macedonio et al., 2016]. A review of the tephra dispersal models is available in Folch [2012]. The new generation of tephra dispersal models depends on i) source term, ii) meteorological fields and iii) transport processes parameterizations (e.g. settling velocity).

II.1 The source terms

Plume height, eruption start and duration and TGSD are the main source terms, described by means of plume models for assessing the vertical mass distribution along the main axis [e.g. Folch et al., 2016].

A simple approach consists of assuming a geometric vertical mass distribution, such as the point source or the Suzuki parameterization as defined below [Suzuki, 1983; Pfeiffer et al., 2005]:

$$S_0(z) = S_0' \left\{ \left(1 - \frac{z}{H}\right) e^{A\left(\frac{z}{H}-1\right)} \right\}^{\lambda}$$

(II.1)

where S_0 is the derivative of mass with z, S_0' is the vertical integration of the S_0, H stands for the column height and A and λ are the Suzuki parameters (Figure II.1), which control the height of the maximum concentration and how the mass is distributed around it, respectively [Pfeiffer et al., 2005].
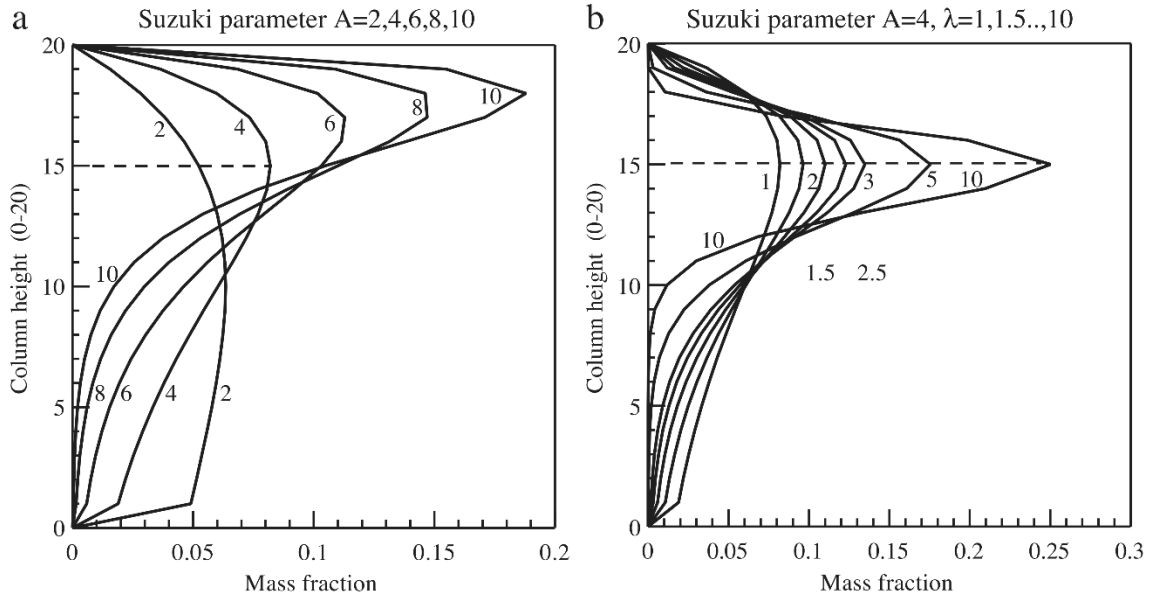
Figure II.1: Suzuki parameters. [Pfeiffer et al., 2005 – Figure 1 modified]

Another approach is based on the radial averaged solution of the Buoyant Plume Theory (BPT) equations in terms of mass, momentum and energy [Bursik, 2001; Folch et al., 2016]. Such models can also account for bent-plume effects due to wind, presence of water and the discretization of the vertical mass distribution by considering the particle velocity. Other more sophisticated computational plume models aim at describing more realistically the fluid dynamics and more complete physics of the transport processes of the volcanic mixture, such as ATHAM [Herzog and Graf, 2010], PDAC [Esposti Ongaro et al., 2007] and FPlume models [Folch et al., 2016]. Although such models are physically more realistic, they require numerous parameters and are computationally very expensive.

Among the input parameters required by the tephra dispersal models, the MER can be assessed through the use of a plume model. Although several empirical relationships between the MER and the column height have been proposed [Mastin et al., 2009; Degruyter and Bonadonna, 2012; Woodhouse et al., 2013], which are compared in Costa et al. [2016b], this study uses the FPlume model [Folch et al., 2016] for the source term characterization. FPlume (Figure II.2) is a steady-state 1D cross-section-averaged eruption column model based on the buoyant plume theory [Morton et al., 1956]. It accounts for additional processes affecting substantially the tephra loading and particle distribution along the plume (e.g. wind coupling, air moisture, particle re-entrainment, and ash aggregation under wet conditions). However, in the occurrence of ash aggregation, FPlume does not account for disaggregation phenomena, i.e. decomposing aggregates from particle collisions, implying that aggregates are transported and deposited without being altered [Folch et al., 2016]. The MER for a given wind profile [Folch et al., 2016] is calculated through the following equation:

$$\widehat{M} = \pi r^2 \hat{\rho} \hat{u} = \sum \widehat{M}_i + \widehat{M}_w + \widehat{M}_a$$

(II.2)

where $\widehat{M}$ is the MER, r refers to the plume radius assumed as axial symmetric, $\hat{\rho}$ is the mixture density (kg/m^3), $\hat{u}$ is the mixture velocity along the plume axis (m/s). The MER can also be expressed as the sum of the mass flow rate of particles of class i ($\widehat{M}_i$), the mass flow rate of volatiles ($\widehat{M}_w$) and the mass flow rate of entrained air ($\widehat{M}_a$). FPlume estimates the MER considering two turbulent air entrainment coefficients (i.e. radial − α and cross-flow − β coefficients, respectively). These two parameters aim at describing the air mixing in the plume [Bursik, 2001; Suzuki and Koyaguchi, 2015]. FPlume is run prior the tephra dispersal model providing the source terms. As input, the plume model requires information about the magma water content, initial magma temperature, ejection velocity and a meteorological profile.
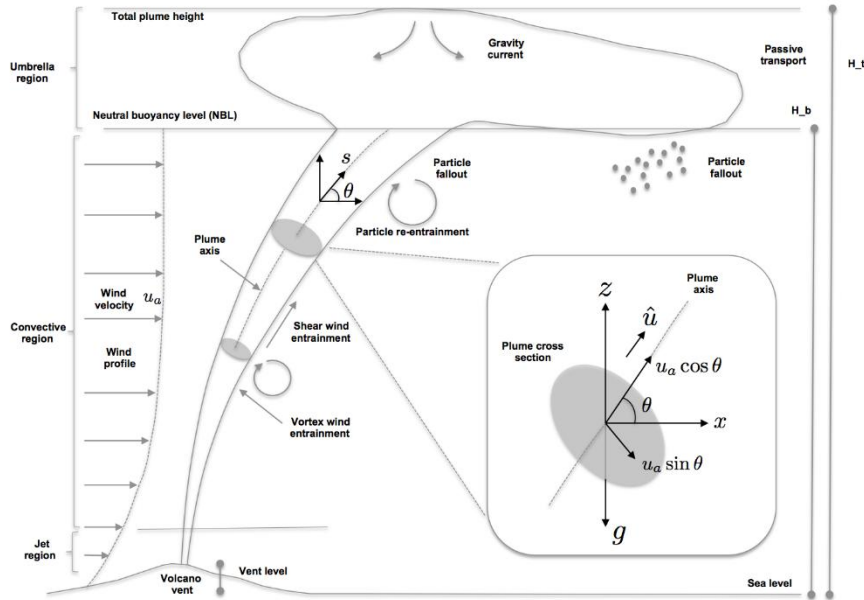
Figure II.2: Scheme of the FPlume model. [Folch et al., 2016 – Figure 1]

II.2   Meteorological fields

Tephra dispersal models need, as input, meteorological fields (e.g. wind, temperature, air moisture, boundary layer heights) over the studied domain. Depending on the application, the meteorological database can be at local, meso or global scale and can be obtained from numerical weather prediction or re-analysis models, for forecast or reconstruction purposes, respectively. Two strategies are typically used to model tephra dispersal as explained in Folch [2012]: i) the on-line and ii) the off-line strategy. Although the on-line strategy benefits from the best modelling accuracy (based on the synchronization of the tephra dispersal model with

the numerical weather prediction model) [Martí et al., 2016], the off-line strategy is widely used, being a good compromise between the computational time and the model resolution. The off-line strategy consists of reading the meteorological variables over the domain through fixed points and regular time-intervals. It is worth noting that such a strategy usually implies discrepancy between the spatial resolution of the tephra dispersal model and the meteorological database.

II.3 Formulation of tephra dispersal models

The first models designed for assessing the sedimentation from volcanic plumes were by Suzuki [1983], Carey and Sparks [1986], Wilson and Walker [1987] and Armienti et al. [1988]. Then the models were improved to better simulate deposits by implementing processes such as the convection and gravitational effects or the variability of the terminal fall velocity [Bursik et al., 1992; Sparks et al., 1992; Bonadonna and Phillips, 2003]. Eulerian, Lagrangian and Hybrid models have been introduced.

II.3.1 Eulerian approach

Eulerian models are based on the solution of the Advection-Diffusion-Sedimentation (ADS) equation, dividing the Earth's atmosphere into a fixed 3D grid and solving for flux between grid cells. The equation consists on the principle of the particle mass conservation moving inside a volume of fluid (e.g. atmospheric fluid: air). Such approach solves for the following equation:

$$\frac{\partial C}{\partial t} = -\frac{\partial (u_x C)}{\partial x} - \frac{\partial (u_y C)}{\partial y} - \frac{\partial (u_z C)}{\partial z} + \frac{\partial}{\partial x}\left(K_h \frac{\partial C}{\partial x}\right) + \frac{\partial}{\partial y}\left(K_h \frac{\partial C}{\partial y}\right) + \frac{\partial}{\partial z}\left(K_v \frac{\partial C}{\partial z}\right) + \frac{\partial (u_s C)}{\partial z}$$
$$+ S_0 + S_k$$

(II.3)

where C refers to the particle mass concentration, t is the time, $u = (u_x, u_y, u_z)$ is the wind velocity, K = diag(K_h, K_h, K_v) with K_h and K_v are the horizontal and vertical turbulent diffusion coefficients, respectively, u_s is the sedimentation term, S_0 is the source term (i.e. production of particles) and S_k is the sink term (i.e. loss of particles).

II.3.2 Analytical model

Analytical models are based on assumptions that simplify Equation II.3: i) the vertical wind (u_z) and diffusion (K_v) coefficients are equal to 0, ii) the wind is homogeneous horizontally for the two components (i.e. $u_x = u_x(z)$ and $u_y = u_y(z)$), iii) the horizontal turbulent diffusion is constant (i.e. $K_h = K$), iv) the settling velocity divergence term is neglected and v) all the

particles are released vertically at a source point (i.e. $S_0 = \delta_0$). It follows that Equation II.3 becomes:

$$\frac{\partial C}{\partial t} = -u_x \frac{\partial C}{\partial x} - u_y \frac{\partial C}{\partial y} + u_s \frac{\partial C}{\partial z} + K \left(\frac{\partial^2 C}{\partial x^2} + \frac{\partial^2 C}{\partial y^2} \right) + \delta_0$$

(II.4)

having an analytical solution for each particle concentration as [Macedonio et al., 2005]:

$$C = \frac{1}{4\pi K t} e^{-\frac{(x-x_0-u_x t)^2+(y-y_0-u_y t)^2}{4Kt}} \delta(z - z_0 + u_s t)$$

(II.5)

Examples of analytical models based on the Gaussian solution for the deposit are ASHFALL [Hurst and Turner, 1999; Hurst and Smith, 2004], TEPHRA [Connor et al., 2001; Bonadonna et al., 2005] and HAZMAP [Macedonio et al., 2005; Pfeiffer et al., 2005]. Limitations of such models are discussed in Folch [2012].

II.3.3 Numerical model

Numerical models are introduced due to the limitations of the Gaussian models. Indeed, the numerical solution of Equation II.3 allows the computation of both the tephra loading and the airborne ash mass with time. Although such models can be applied for any context, their use increases substantially the bulk computational cost (details in Folch [2012]). Among the models, there is FALL3D [Costa et al., 2006; Folch et al., 2009], and ASH3D [Mastin et al., 2013; Schwaiger et al., 2012].

FALL3D is a 3D time-dependent Eulerian model solving for a set of equations describing the particle behaviour within the atmosphere. The tephra transport is governed by the main atmospheric fields (e.g. wind advection, turbulent diffusion and gravitational settling). The eruption can alter significantly local atmospheric conditions, increasing the complexity for computing the tephra behaviour within a highly perturbed environment. Consequently of ignoring numerically these effects, the model accuracy decreases at very proximal distance from the source (i.e. few kilometres). Moreover, the proximal area is mostly affected by large clast objects (i.e. volcanic bombs) deposited following a ballistic trajectory (Figure I.1).

FALL3D can be coupled with the integral plume model (FPlume; Section II.1; Folch et al. [2016]) to describe the source term. The particle transport and settlement are governed by the following equation, which does not account for any particle-particle interaction (e.g. ash

aggregation or collision). The continuity equation is given as the Eulerian form in a generalized coordinate system (X, Y, Z) as described in Byun and Schere [2006] and Costa et al. [2006]:

$$\frac{\partial C}{\partial t} + V_X \frac{\partial C}{\partial X} + V_Y \frac{\partial C}{\partial Y} + \left(V_Z - V_{sj}\right)\frac{\partial C}{\partial Z} = -C\nabla \cdot V + C\frac{\partial V_{sj}}{\partial Z} + \frac{\partial}{\partial X}\left(\rho_* K_X \frac{\partial \, C/\rho_*}{\partial X}\right) +$$

$$\frac{\partial}{\partial Y}\left(\rho_* K_Y \frac{\partial \, C/\rho_*}{\partial Y}\right) + \frac{\partial}{\partial Z}\left(\rho_* K_Z \frac{\partial \, C/\rho_*}{\partial Z}\right) + S_*$$

(II.6)

where C is the transformed concentration (i.e. scaled average concentration) and $V = (V_X, V_Y, V_Z)$ is the transformed wind speed (i.e. scaled wind speed). The term ρ_* is the transformed atmospheric density (i.e. scaled atmospheric density), and S_* refers to the transformed source term (i.e. in the used coordinate system).

This equation accounts for mass conservation during atmospheric transport of tephra in an explosive eruption and affects the released particles, which are regrouped in the ADS system. FALL3D solves the equation for each particle class i by considering for the curvilinearity of the Earth and applying a correction factor on the terrain-following coordinate system through the Jacobian of the transformation. The scaling procedure is done through the map scale factor (m) or the Jacobian (J) accordingly to the operation [Byun and Schere, 2006] and summarized in Table II.1. Then, each particle class i is assigned a triplet (d_p, ρ_*, F_p), which contains the diameter, density, and shape factor, respectively.

Parameter	Scaling
Coordinates	$X = mx;\ Y = my;\ Z = z\text{-}h(x,y)$
Horizontal velocities	$V_X = mv_x;\ V_Y = mv_y$
Vertical velocity	$\left(V_Z - V_{Sj}\right) = J^{-1}\left[\left(v_z - v_{sj}\right) - m\left(v_x \frac{\partial h}{\partial x} + v_y \frac{\partial h}{\partial y}\right)\right]$
Concentration	$C = \dfrac{cJ}{m^2}$
Density	$\rho_* = \dfrac{\rho J}{m^2}$
Source term	$S_* = \dfrac{SJ}{m^2}$

Table II.1: Scaling factors. The triplet (x,y,z) are the Cartesian coordinates. [FALL3D Manual – Table 1 in Appendix A modified]

For the sake of simplicity, the diameter d_p is assumed as d, which is the diameter of the corresponding sphere for an equivalent volume. The shape parameter (F_p) is defined as the particle sphericity (ψ) given by the ratio of the sphere surface with a diameter d to the particle

surface. It follows that the transport and sedimentation of each particle class *i* will be considered under the triplet (d, ρ_*, ψ), which is highly dependent on the settling velocity. Details on equations, models and parameterizations within the FALL3D code are available in Folch et al. [2009].

Particle sedimentation is controlled by the dry deposition terminal fall velocity for most of the tephra classes. In Equation II.3, u_s is defined as:

$$u_s = u_t + \frac{1}{r_a + r_s + r_a r_s u_t}$$

(II.7)

where r_a and r_s are the aerodynamic resistance coefficients [Feng, 2008] and u_t defines the drag force by the following formulation for a Newtonian fluid [Chhabra et al., 1999]:

$$u_t = \sqrt{\frac{4}{3} \frac{(\rho_p - \rho_a)}{C_D \rho_a} g d}$$

(II.8)

where g is the gravitational acceleration, d is the particle diameter, ρ_p and ρ_a are the particle and fluid (i.e. air) densities, respectively, and C_D is a drag coefficient. u_s, and u_t differ only for micron-sized particles.

In Equation II.3, the sink term for the wet deposition (S_k) is calculated through the parameterization:

$$S_k = -\lambda C = -a P^b C$$

(II.9)

with λ referring to the scavenging coefficient (in s^{-1}), P is the precipitation rate defined by the meteorological database and a and b are precipitation constants [Folch, 2012].

II.3.4 Lagrangian approach

Lagrangian models aim at computing the path followed by a volume of particles within a fluid (e.g. atmospheric fluid: air). Such models are mostly used by VAACs to forecast, track or compute backward the particle trajectories. To do so, the following equation serves to calculate the movement between two time-steps:

$$r(t_2) = r(t_1) + \sum_{t_1}^{t_2} [u + u' + u_s]dt$$

(II.10)

where r refers to the position vector and u' is the turbulent fluctuations (details in Folch [2012]). Regarding the Equation II.10, the integrated terms refer to the ADS presented in the Eulerian form (Equation II.3). Among the Lagrangian models, are HYSPLIT [Draxler and Hess, 1998], JMA [Iwasaki et al., 1998], PUFF [Searcy et al., 1998; Webley et al., 2012], FLEXPART [Stohl et al., 1998; 2005], MLDP0 [D'Amours and Malo, 2004], NAME [Jones et al., 2007; Witham et al., 2007] and MOCAGE-accident [Martet et al., 2009].

II.3.5 Hybrid approach

A hybrid Lagrangian-Eulerian formulation simulates the trajectory of the centre of mass of the released tephra. Then, from the trajectory, the model assumes a particle diffusion following a Gaussian form to assess the particle concentration at regular intervals. An example of models of this category is VOLCALPUFF [Barsotti et al., 2008]. This model is capable to compute in 3 dimensions the transport and sedimentation of the volcanic ash from the source to distal areas. The model couples an Eulerian form describing the plume with a Lagrangian form for the ash dispersal through a series of diffusing packets (named puffs).

II.3.6 Aerosol chemistry model

Several aerosol chemistry models are based the Eulerian approach and were applied to volcanological problems especially after the 2010 Eyjafjallajökull eruptions to track airborne ash and sulphur or sulphate aerosols. Few models are operative, such as REMOTE [Langmann, 2000], COSMO-MUSCAT [Steppeler et al., 2003; Wolke et al., 2004], POLAIR3D [Boutahar et al., 2004] and CMAQ [e.g. Matthias et al., 2012].

II.4   Ash aggregation modelling

For simplicity, most models assume aggregation to occur within the eruptive plume, and neglect any disaggregation process [Mueller et al., 2017b]. Recent studies [Durant et al., 2009; Taddeucci et al., 2011; Van Eaton et al., 2013; Costa et al., 2016a; 2017] have shown how aggregation is a common eruptive feature which contributes significantly to tephra fallout. Considering that this study uses the FALL3D model, which can account for or neglecting aggregation, we report here the parameterizations available within the code to account for ash aggregation. The models assume an effective aggregate class characterized by the diameter d_a (or Φ_a) and the density ρ_a.

II.4.1 Percentage model

The Percentage model (hereinafter *Percentage*) is described in Sulpizio et al. [2012]. The class is enriched by scavenging a constant percentage of the primary particles from the involved classes (i.e. $\Phi \leq \Phi_a$; yellow box in Figure II.3). The effect of using the *Percentage* model on the TGSD is illustrated in Figure II.3. In fact, each class of the original TGSD are depleted in favour of the effective aggregate class created by FALL3D. In Figure II.3, we present the example of a constant percentage with respect to the fines set at 50 wt%.

Aggregation model : *Percentage*
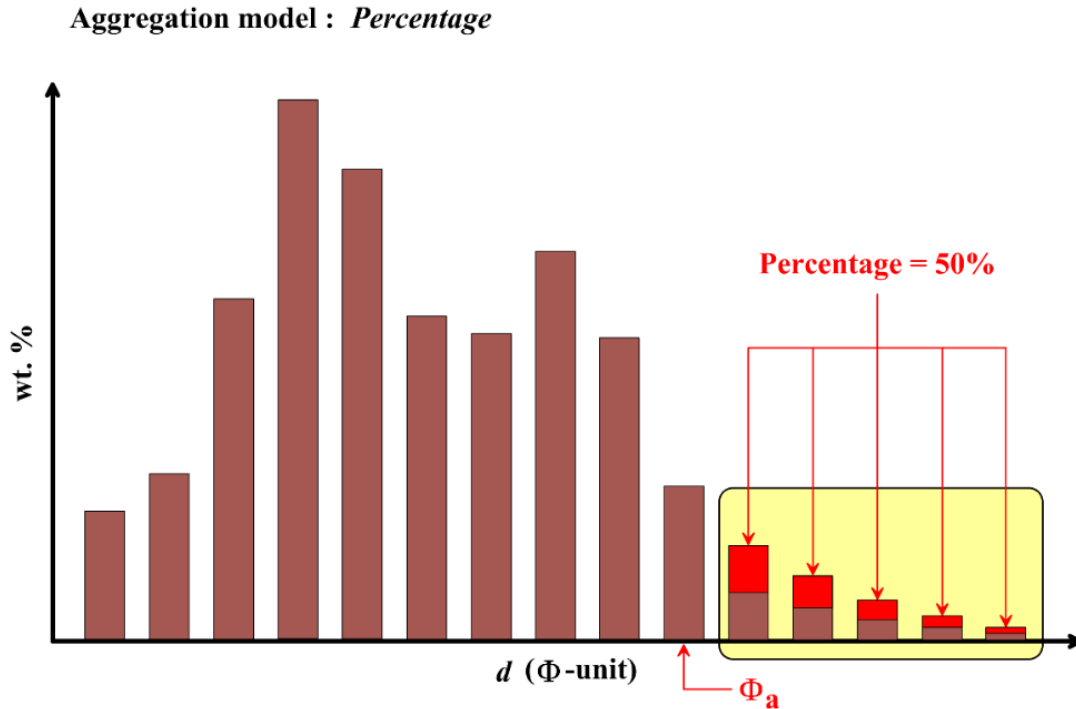
Figure II.3: Sketch of a TGSD modified by the *Percentage* aggregation model.

II.4.2 Cornell model

The Cornell model (hereinafter *Cornell*) was introduced by Cornell et al. [1983]. It was then modified and implemented in FALL3D [Costa et al., 2012]. The aggregate fraction is assigned with 50 wt% of particle with diameter 63-44 μm, 75 wt% of 44-31 μm and 90 wt% of ash smaller than 31 μm. The Figure II.4 shows how the *Cornell* model procedure enriches the aggregate class by removing the particles from the corresponding classes of the original TGSD.
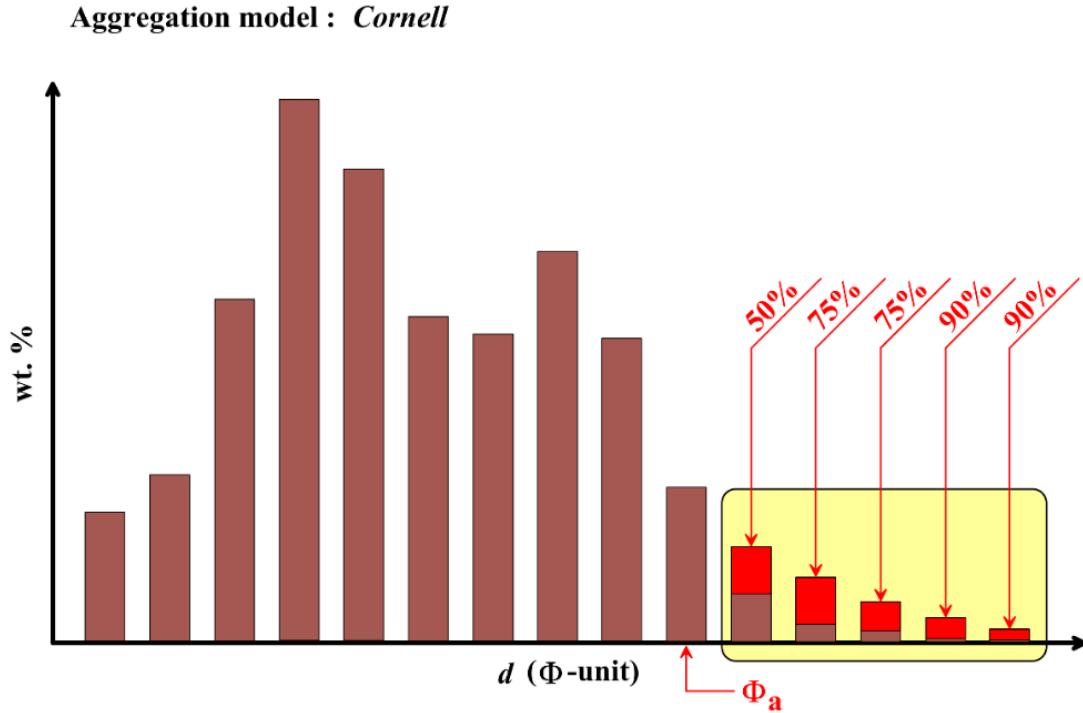
Figure II.4: Sketch of a TGSD modified by the *Cornell* aggregation model.

II.4.3 Costa model

The Costa model (hereinafter *Costa*) accounts for aggregation [Costa et al., 2010; Folch et al., 2010] by considering water in either liquid or solid phases from atmospheric or magmatic origin [Folch et al., 2016]. The *Costa* model accounts for the Brownian motion, ambient fluid shear and the differential sedimentation. The model requires two parameters which have to be calibrated, i.e. the fractal exponent (D_f) and the aggregate settling velocity correction factor (ψ_e) related to the aggregate porosity [Costa et al., 2010; Folch et al., 2010; 2016]. The model is based on a simplified solution of the Smoluchowski equation [Smoluchowski, 1917] and represents a good compromise between the full aggregation processes described in the Smoluchowski equation [Smoluchowski, 1917] and the need to reduce the bulk computational cost. Figure II.5 shows an example of how the *Costa* model allocates the erupted ash within the effective aggregate class (Φ_a, ρ_a) from the original TGSD by estimating the involved fraction for each class.

Aggregation model : *Costa*
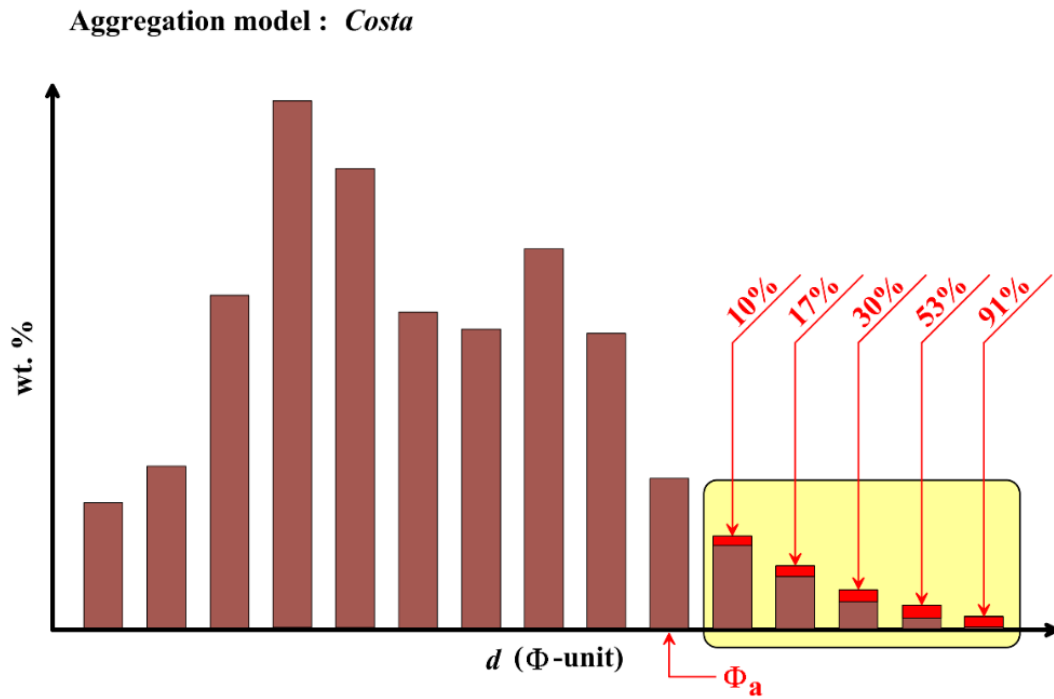
Figure II.5: Sketch of a TGSD modified by the *Costa* aggregation model. The indicative red fractions reflect the fine enrichment of the TGSD.

Chapter III – Observational data and inversion procedure

To better constrain the ESP used to run the simulations, all the available observations are used in terms of tephra release and fallout, plume evolution and ash dispersal. The following sub-sections describe the data used within different applications throughout the manuscript. This study integrates data from various instruments to better cover the grain-size spectrum, similar to recent studies [Bonadonna et al., 2011; Corradini et al., 2016]. Among the ESPs, the TEM is typically estimated by integrating the mapped tephra deposit [Andronico et al., 2014a; Bonadonna and Costa, 2012; 2013]. However, the estimation would benefit from the integration of different methods to cover entirely the grain-size spectrum from the blocks to the very fine ash particles (Figure III.1). Moreover, these methods can be used in parallel to better describe the eruption features (e.g. tephra exit velocities, column height, eruption duration, TGSD). From a computational point of view, the most critical parameter describing the initial conditions at the source is the particle size distribution generate by magma fragmentation (i.e. the TGSD). Considering the instrument complementarity in terms of grain-size coverage in Figure III.1, such parameter can be achieved by integrating several of the following data.
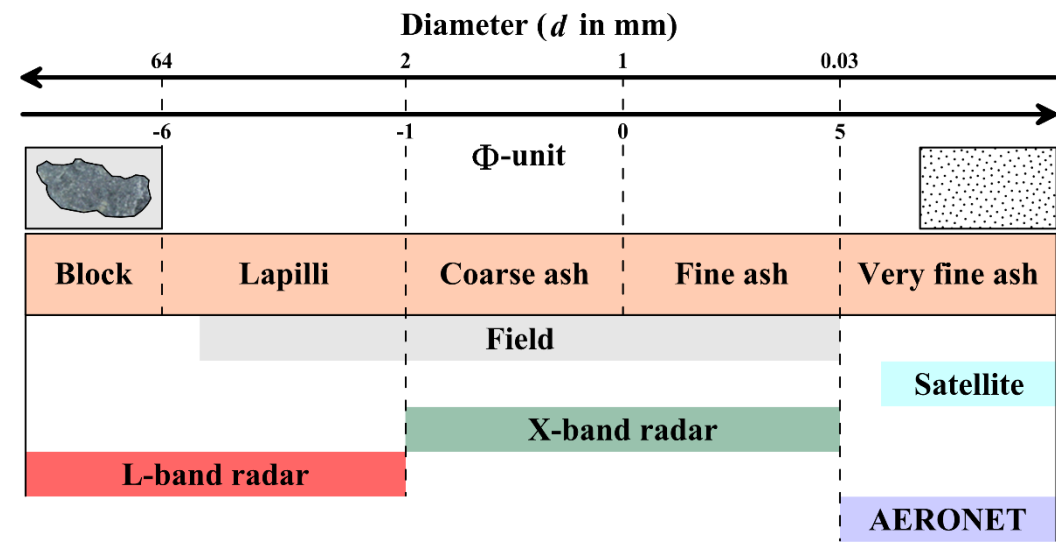
Figure III.1: Grain-size spectrum associated with the different methods.

III.1   Field data

Considering that no sophisticated equipment is required to carry out field measurements, they are the first information collected, weather permitting, from the slopes of the volcano towards the main plume axis. Although sampling is highly hazardous in terms of tephra fallout (panels a and b in Figure III.2) and deposited layers (e.g. slippery roads; panel c in Figure III.2), field

campaigns to delineate the areas affected by the tephra fallout and to measure the load per unit area, which is used afterwards to estimate the TEM [Bonadonna and Costa, 2012].

Figure III.2: Tephra fallout deposit of the 23rd November 2013 Etna paroxysm with an example of impact on infrastructure by showing the tephra layer on the main road around Etna. [Andronico et al., 2015 – Figure 2 modified]

After collection, samples are oven-dried prior to analysis in the laboratory. Then, the GSD is measured for each sample. The classical methods used are mechanical sieving (panel a in Figure III.3) or optical measurement (panel b in Figure III.3). Both instruments provide GSD from -5 to 5 Φ (see Figure III.1) and show a good agreement allowing their use alternatively if necessary [Lo Castro and Andronico, 2008]. Sieves can be used only for grain sizes down to 64 µm and the limiting dimension for particles, which determines whether they fall through the mesh in a sieve, is their intermediate diameter. Sieve analysis gives mass fraction of each size bin, explaining the resulting distribution is inherently binned. Optical measurement uses the principle of dynamic image analysis of projected particle shadows recorded by a dual-camera system, giving a binned distribution.

Regarding distal areas from the source, the samples may be composed of a low quantity of very fine tephra indicating the second method more suitable giving a statistically accurate GSD measurement. Moreover, the scarcity of such sample requires to use a method that returns it intact afterwards.
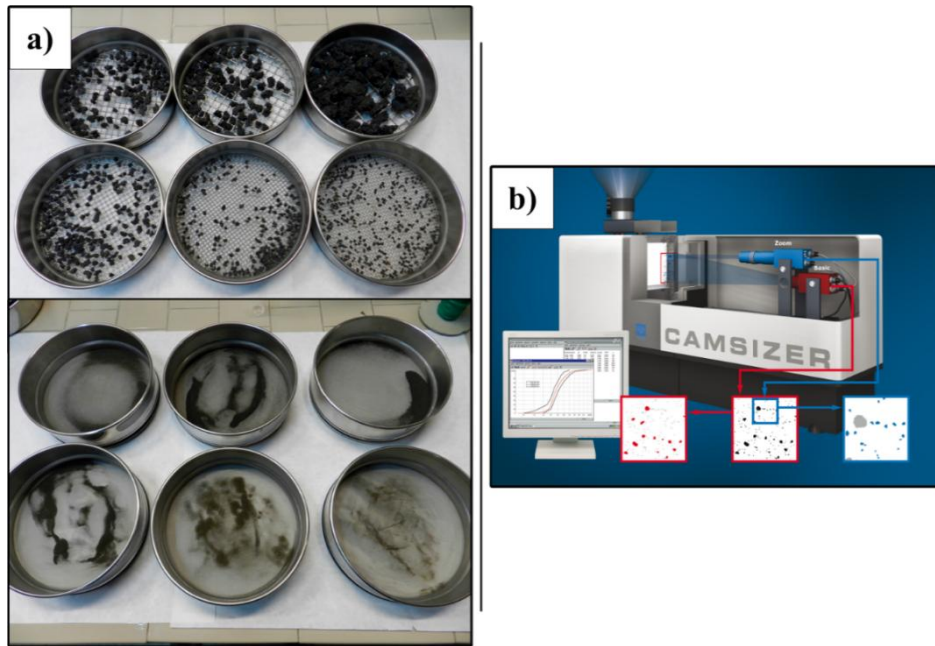
Figure III.3: GSD analysis performed by: a) Sieving method. b) CAMSIZER instrument (Retsch technology).

III.2   Satellite-based data

Geostationary space-based instruments (e.g. Meteosat Second Generation – MSG) are now widely used for monitoring volcanic activity by providing worldwide coverage at a time-resolution that allows most eruptive processes to be recorded [Prata and Kerkmann, 2007; Bonadonna et al., 2011; Folch et al., 2012; 2014; Gouhier et al., 2012; Boichu et al., 2016; Corradini et al., 2016]. Indeed such sensors are able to detect and track volcanic clouds over hundreds to thousands of kilometres from the source. Satellite-based thermal infrared (TIR) sensors are very useful for characterizing volcanic ash [Guéhenneux et al., 2015; Gouhier et al., 2016]. In the TIR region (i.e. 7-14 µm), we can distinguish silicate particles (e.g. volcanic ash) from other aerosols (e.g. ice crystals, SO_2, or H_2SO_4) using a two-channel difference model based on the absorption feature between the 11- and 12-µm wavelengths [Prata, 1989b; Wen and Rose, 1994; Watson et al., 2004]. It was shown that the difference between the at-sensor "Planck" brightness temperature (referred to as BTD) observed in these two channels is negative (-ΔT) for ash and positive (+ΔT) for ice. Wen and Rose [1994], built on early work [Prata, 1989b], developed a forward retrieval model that quantifies the effective radius (r_e) and optical depth (τ_c) from the extinction efficiency factor (Q_{ext}) calculated using the Mie theory. This allows a theoretical look-up-table to be produced for sets of variations of both r_e and τ_c as a function of the brightness temperature. From inverse procedure, r_e and τ_c (and hence the mass of the volcanic ash cloud) can be retrieved for any given brightness temperature pair (details in Prata and Grant [2001]; Watson et al. [2004]). However, satellite retrievals are affected by several factors such as the surface characteristics (i.e. temperature and emissivity), plume

geometry (i.e. altitude and thickness), ash optical properties and water vapour. These factors produce uncertainty of ~40% and ~30% respectively associated with the total mass retrieval and effective radius [Corradini et al., 2008]. Another source of uncertainty is related to the presence of large particles (typically for $r_e > 6$ µm), possibly within the fine ash clouds, which cannot be retrieved using the Mie theory as Q_{ext} does not vary significantly for $r_e > \lambda/2$ [Guéhenneux et al., 2015; Stevenson et al., 2015]. Overall, the effects related to both misdetection issues (i.e. BTD) and the presence of coarse ash particles in the cloud lead to a mass under-estimation of 50% [Stevenson et al., 2015].

The use of data from the SEVIRI (Spinning Enhanced Visible and Infrared Imager) sensor on-board MSG provides 1 image every 15 minutes at a spatial resolution of ~3×3 km at nadir. Satellite data are available online, for instance, from HOTVOLC [HOTVOLC Website], which is a web-based satellite-data-driven monitoring system developed at the OPGC (Observatoire de Physique du Globe de Clermont-Ferrand, France). This system is designed for real-time monitoring of active volcanoes [Gouhier et al., 2016]. Weather conditions permitting, the images (e.g. Figure III.4) may show the eruption features from proximal areas soon after the onset, or a far-travelled dilute cloud.
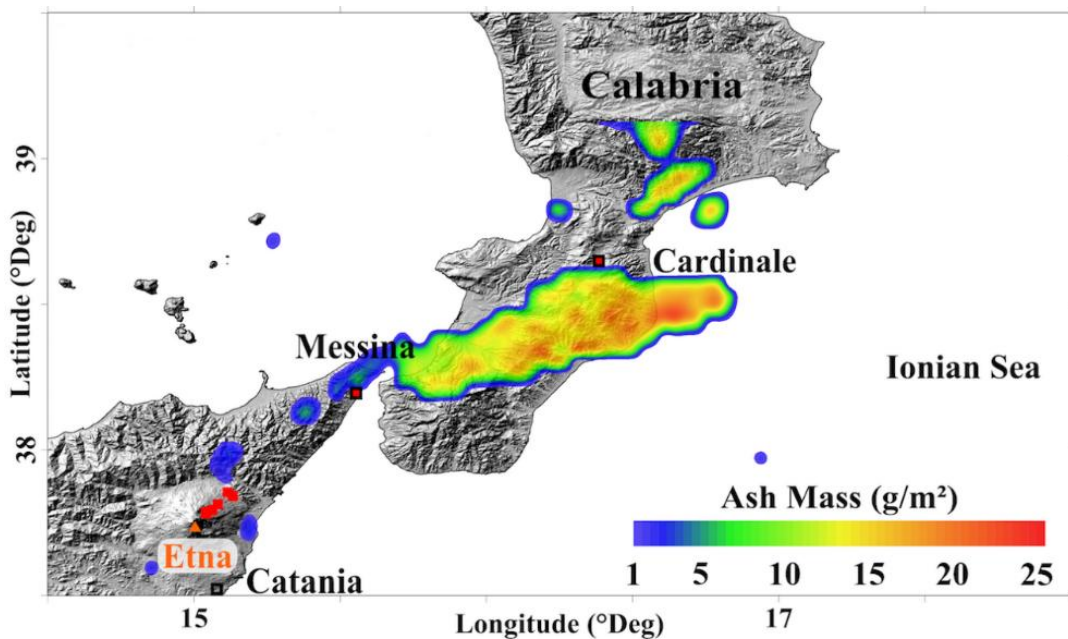
Figure III.4: Example of satellite retrieval showing the ash mass at 19:45 released during the 23rd February 2013 Etna paroxysm. [Poret et al., 2017 – Under Review]

III.3   Ground-based data

Among the ground-based sensors capable of observing an eruption, the remote sensing systems include direct observations (e.g. seismic tremor and video monitoring), radar and sun-photometer.

III.3.1 Seismic tremor signal

Seismic tremor shows the pressure fluctuation induced by the injection of magma into the rock. When a volcanic activity starts, the signal intensity may increase in correlation with the seismic activity. The use of the volcanic tremor aims at accurately timing the activity start and end together with the different main eruption phases as observable in the Figure III.5. Some eruptive features can be characterized through the tremor signal such as the initialization of Strombolian activity (white ellipse), the paroxysm episodes (red ellipses) which have very short duration compared with the emplacement of a lava flow (red slot) that may range from hours to days.
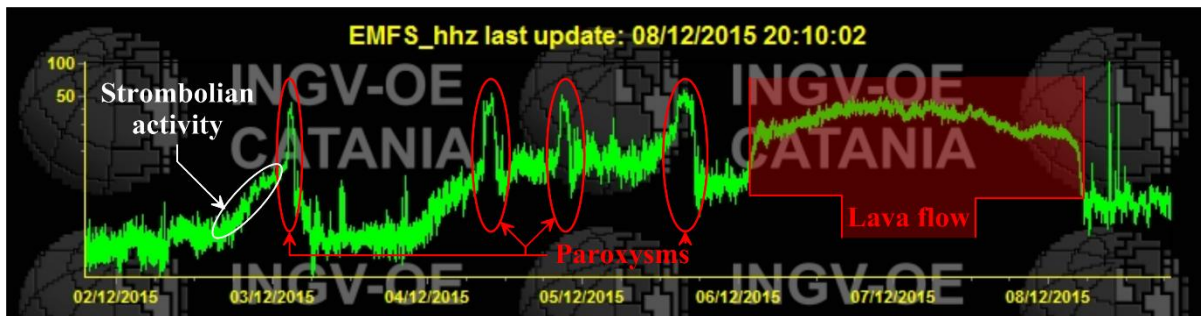
Figure III.5: Tremor signal of the eruptive sequence of the 3rd December 2015 on Etna. [INGV – OE Website]

III.3.2 Visible and Infrared images

Video-monitoring using both visible and/or infrared, together with tremor signal help to accurately estimate the eruption start and duration. As soon as the eruption begins, the images allow direct observations of the eruptive column assessing in real time the column height. Figure III.6 shows the time-series of the 23rd February 2013 Etna eruptive activity. Thermal images (top panel; 1T-5T) indicate the plume height and the spreading direction, whereas the visible images (bottom panel; 1V-5V) complete the observations. It is worth noting that the sensors are complementary during nocturnal events. Nonetheless, the detection limit depends on the image window (here maximum 9.5 km above sea level – a.s.l.), which explains the importance of combining the video-monitoring with other sensors such as the radar systems or satellite-based instruments to achieve a robust estimation of the column height.
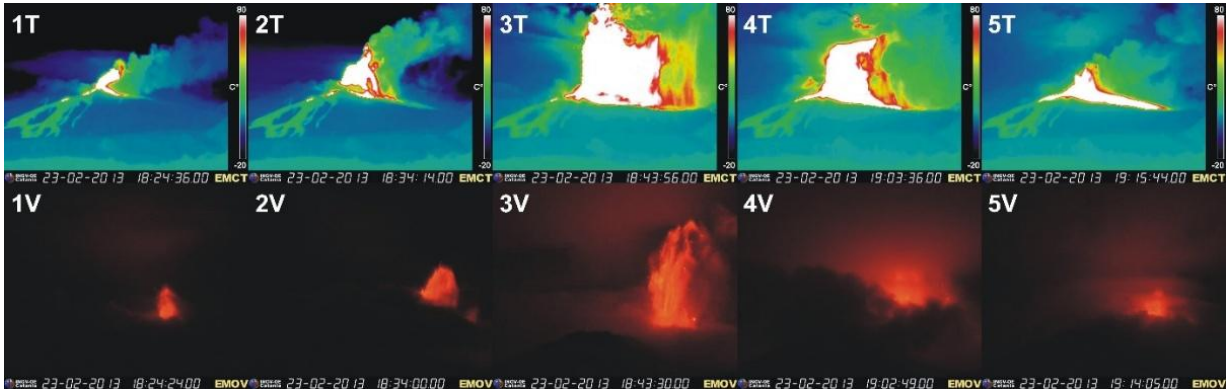
Figure III.6: The top panel shows thermal images of the 23rd February 2013 eruption of Etna. The bottom panel refers to the corresponding images in the visible spectrum. [Poret et al., 2015]

III.3.3 Weather radar

Although weather radar (X-band and C-band) is designed for weather forecast purposes, it is now widely used to monitor the volcanic activity. The X-band systems operates at the wavelength of ~3 cm providing volumetric scans every 10 minutes. As described in Vulpiani et al. [2016], the X-band radar retrieves i) reflectivity, ii) correlation coefficient in the returned signal, iii) radial velocity iv) differential reflectivity (in decibels), v) specific differential phase shift and vi) spectral width [Montopoli, 2016]. Processing of these data leads to estimates of ash concentration, exit velocity, column height, volcanic cloud top height and Particle-Size Distribution (PSD). To convert PSD into TGSD (in Φ-unit), we used PSD given as ash number density distribution [e.g. Corradini et al., 2016]. Then, the average for the whole event takes in input each PSD estimated from each single radar resolution volume delineated by horizontal angle, vertical angle, and range distance at each available time step for the airborne ash mass seen by the radar. PSD is converted into number of particles per unit of volume with the particle-size bins. By means of the volume and density associated with the size bins, the mass density distribution is calculated. Retrieved effective radius ranges from -1 to 5 Φ (see Figure III.1; Corradini et al. [2016]). The difference of the radar measurements in terms of grain-size with the field data suggests their integration to enlarge the observations. Figure III.7 illustrates the radar retrievals by showing the top height of the volcanic cloud and the spreading at 10:10 in the morning of the 23rd November 2013, when Etna erupted.
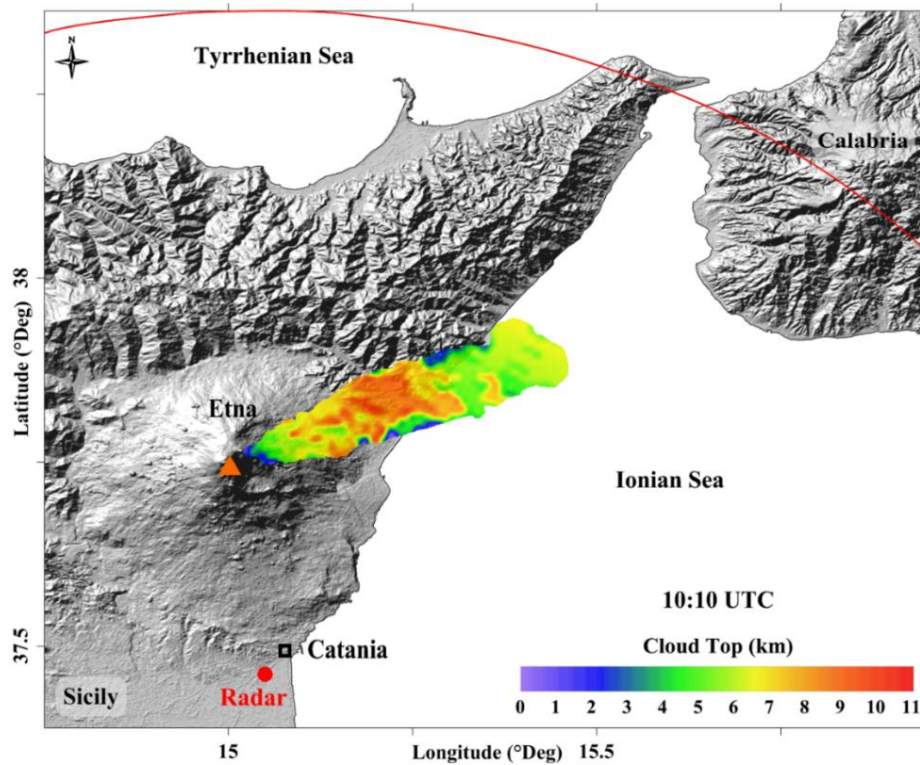
Figure III.7: Volcanic cloud top retrieved with the X-band radar for the 23rd November 2013 paroxysm of Etna (orange triangle). The red line refers to the radar detection limit installed at Catania airport (red point).

III.3.4 L-band Doppler radar – VOLDORAD 2B

The pulsed L-band Doppler radar (hereinafter VOLDORAD 2B) is a near-source instrument suitable to observe the volcanic activity in the very proximal area (hundreds of meters from the vent; Figure III.8). The radar is used worldwide to monitor volcanoes such as Stromboli and Etna (Italy), Yasur (Vanuatu), Arenal (Costa Rica) or Popocatépetl (Mexico). VOLDORAD 2B aims at observing in real-time the eruption by characterizing the main source parameters such as the eruption start and duration, the eruptive phases, the exit velocities of the erupted material, the MER and thereby the TEM [Donnadieu et al., 2015; 2016; Freret-Lorgeril et al., 2016]. Indeed, the radar operates at a wavelength of 23.5 cm allowing lapilli to block-sized (i.e. $\Phi \leq -1$; see Figure III.1) to be detected through a short window (panel b in Figure III.8). The detection is highly dependent on the erupted material as well as the concentration. It follows that the lower limit may vary highlighting the necessity of working in a multi-system approach. Inferred radar parameters (e.g. backscattered echo power) are proportional to the quantity of tephra detected through the radar beam. In addition, the along-beam radial velocities permit lava fountains from being observed at high time resolution (i.e. 0.2 s), inferring near-source detection of the ejection velocities by means of the following equation [Freret-Lorgeril et al., 2016; Donnadieu et al., 2017]:

$$V_e = \frac{v_{r+}}{\sin\theta} \approx 3.89 v_{r+}$$

<div align="right">(III.1)</div>

where V_e is the ejection velocities (in m/s), v_{r+} is the radial velocity (in m/s) and θ is the elevation angle of the radar beam (here $\theta = 14.9°$). Such approach is relevant for integrating the time-dependent ejection velocities with the corresponding observed eruptive column heights. In particular, VOLDORAD 2B data are used for better constraining the eruption phase characterization.
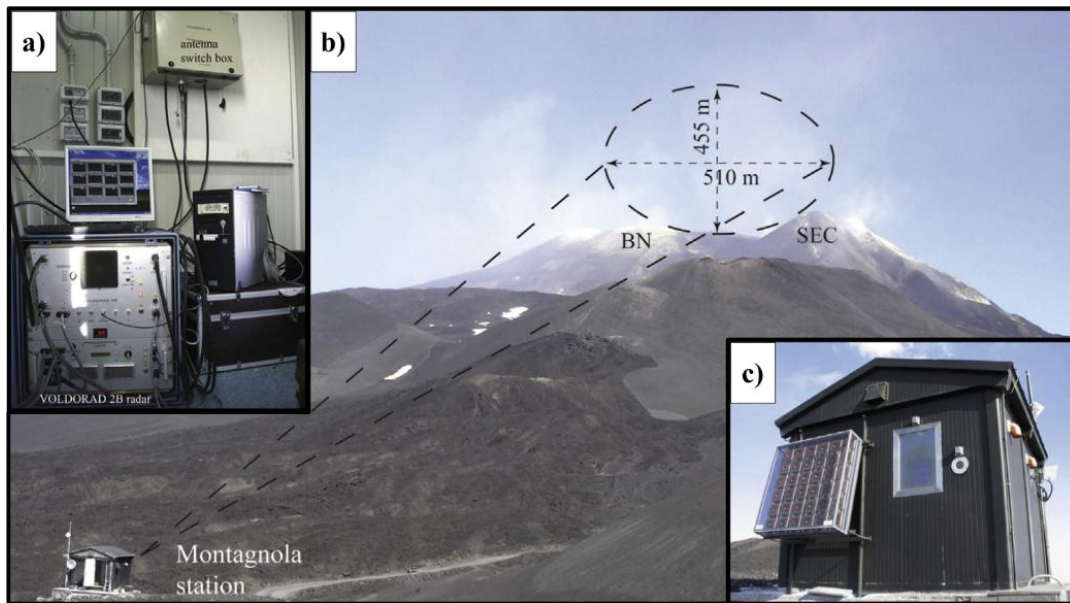
Figure III.8: View of the configuration of the VOLDORAD 2B system (panel a) installed on Etna (Montagnola station; panel b). c) Shows the shelter of the radar. [Donnadieu et al., 2016 – Figure 2 modified]

III.3.5 AERONET data

The AErosol RObotic NETwork (AERONET) is a ground-based remote sensing network [Holben et al., 1998] supervised by NASA and the "PHOtométrie pour le Traitement Opérationnel de Normalisation Satellitaire" (PHOTONS). AERONET aims at retrieving in real-time a global database from solar spectral irradiance to assess aerosol optical properties, e.g. volume size distribution, particle sphericity (estimated here as the ratio between the backscattered and the depolarization signals), and Aerosol Optical Depth (AOD) to validate satellite observations [Dubovik et al., 2006]. The columnar AOD is measured from solar radiance [Holben et al., 2006] at diverse spectral channels (e.g. 500 nm) through three data quality levels [Dubovik et al., 2006]. In addition, direct-sun-derived AOD processing [Watson

and Oppenheimer, 2001; O'Neill et al., 2003] integrates signal (in voltage) from the sensor to the top of the atmosphere, given by the sun-photometer measurement at the Mauna Loa Observatory of Hawaii. The proportionality between the spectral irradiance at the sensor and the acquired signal is used to convert into AOD. However, wavelength-dependent gas (e.g. H_2O, O_3, NO_2, CO_2, and CH_4) may scatter light and must be subtracted when calculating the AOD. During the inversion procedure, the error is assumed to be distributed lognormally and uncorrelated giving a standard deviation of 5% associated with the sky radiance measurement [Dubovik and King, 2000; Dubovik et al., 2000; Dubovik, 2004]. AOD at 500 nm wavelength is used as standard to compute the fine mode fraction of the total AOD [e.g. Folch et al., 2012]. It is worth noting that the assumption of a lognormal distribution, made for both AERONET and satellite retrievals, is not fully consistent with the empirical distribution we adopt in this work and has to be considered as an approximation of it.

The grain-size spectrum associated with the AERONET retrievals concerns the very fine ash particles (i.e. $\Phi \geq 5$; see Figure III.1) as described in Taylor et al. [2014]. However, this study uses the AERONET data to validate the simulations in terms of airborne ultra-fine ash dispersed to very distal areas (thousands of kilometres from source). Indeed, the released volcanic particles may be transported worldwide as observed recently with the Calbuco eruption (Chile, April 2015). In addition to the transport, the AOD measurement of volcanic material may be altered by the presence of mineral dust within the atmosphere (e.g. Saharan sand particles). In such case, the AOD signal has to be corrected by subtracting the estimated dust contribution in terms of AOD, which can be done through the GEOS-chem model [Bey et al., 2001; Park et al., 2004; Fairlie et al., 2007; Chan and Chan, 2017].

Chapter IV – Etna paroxysmal episode of the 23rd February 2013

Modelling eruption source parameters by integrating field, ground-based and satellite-based measurements: The case of the 23rd February 2013 Etna paroxysm

M. Poret[1, 2], A. Costa[1], D. Andronico[3], S. Scollo[3], M. Gouhier[4], and A. Cristaldi[3]

[1] Istituto Nazionale di Geofisica e Vulcanologia, Sezione di Bologna, Bologna, Italy

[2] University of Bologna, Geophysics department, Bologna, Italy

[3] Istituto Nazionale di Geofisica e Vulcanologia, Osservatorio Etneo, Sezione di Catania, Catania, Italy

[4] Clermont-Ferrand Université, Université Blaise Pascal, Laboratoire Magmas et Volcans, France

Abstract

Volcanic plumes from Etna volcano (Italy) are governed by easterly winds driving ash over the Ionian Sea. The limited land tephra deposit makes TGSD assessment and its fine ash fraction highly uncertain. On 23rd February 2013, a lava fountain produced a ~9 km high column a.s.l.. The atypical north-easterly wind direction dispersed the tephra from Etna to the Puglia region (southern Italy) allowing tephra sampling up to very distal areas. This study uses field measurements to estimate the field-based TGSD. Very fine ash distribution (PM_{10}) is explored parameterizing the field-TGSD through a bi-lognormal and bi-Weibull distribution. However, none of the two latter TGSDs allow simulating any far-travelling airborne ash up to distal areas. Accounting for the airborne ash retrieved from satellite (SEVIRI), we proposed an empirical modification of the field-based TGSD including very fine ash through a power-law decay of the distribution tail. The input source parameters are inverted by comparing simulations against measurements. Results suggest a column height of ~8.7 km a.s.l., a total erupted mass of ~4.9×10^9 kg, a PM_{10} content between 0.4-1.3 wt%, and an aggregate fraction of ~2 wt% of the fine ash. Aerosol optical depth measurements from AERONET are also used to corroborate the results at ~1700 km from the source. Integrating numerical models with field, ground-based and satellite-based data aims at providing a better TGSD estimation including very fine ash, crucial for air traffic safety.

Keywords: Total grain size distribution, PM_{10}, FALL3D, SEVIRI, Tephra dispersal, Air traffic safety

Introduction

One of the main goals of modern volcanology is a better understanding and quantification of ESP governing tephra dispersal during a volcanic crisis. This is done using field [e.g. Andronico et al., 2008a; 2008b; 2014b], remote-sensing retrievals [e.g. Corradini et al., 2008; 2016; Scollo et al., 2012; 2014; Gouhier et al., 2016], laboratory experiments [e.g. Bagheri and Bonadonna, 2016; Cigala et al., 2017; Mueller et al., 2017a; 2017b], and numerical models [e.g. Scollo et al., 2008; Bonadonna and Costa, 2012; Folch et al., 2016]. ESP assessment [e.g. Mastin et al., 2009; Folch, 2012] involves the estimation, among others, of the MER, which combined with the eruption duration provides the TEM. The field-derived TEM is obtained by integrating the isomass maps [e.g. Bonadonna and Costa, 2013], which requires tephra deposits to be sampled at several locations [Bonadonna et al., 2015c]. In addition to the TEM, field data give geolocalized GSD permitting the TGSD to be estimated by integrating local GSD [Bonadonna and Houghton, 2005; Bonadonna et al., 2015c]. Tephra is classified depending on the size [e.g. Folch, 2012], as bombs or blocks (i.e. diameter – $d \geq 64$ mm), lapilli ($2 \leq d < 64$ mm), and ash ($d < 2$ mm). Within ash, we further distinguish fine ash ($d < 1$ mm), very fine ash ($d < 30$ µm) [Rose and Durant, 2009], and ultra-fine ash ($d < 5$ µm). Hereinafter, we define the very fine ash as particle matter below 10 µm (hereinafter PM_{10}). Nonetheless, the TGSD strongly depends on the sampling distance from the source [Costa et al., 2016a], the number of available samples [Bonadonna and Houghton, 2005; Bonadonna et al., 2015c], and the spatial distribution [Bonadonna et al., 2015c; Spanu et al., 2016]. Moreover, the fine ash fraction within the TGSD is likely under-estimated due to the long atmospheric residence time ranging from hours to days [Rose and Durant, 2009], preventing very fine ash from sampling at reasonable distance [Costa et al., 2016a]. For these reasons, TGSD assessment is highly uncertain, especially for the fine ash fraction [Bonadonna et al., 2011; Costa et al., 2016a], which depends on the eruption type [Rose and Durant, 2009]. Indeed, a basaltic volcano commonly produces a fine ash fraction of few percent of the erupted material, whereas the fraction from silicic eruption can contains between 30-50 wt% [Rose and Durant, 2009].

The statements described above highlight the need for an integrated approach that encompasses the grain-size spectrum down to the very fine ash. Recent eruptions reveal how an accurate estimation of such fraction is crucial for air traffic safety [e.g. Casadevall, 1994; Bonadonna et al., 2011; Folch et al., 2012]. As an example, Bonadonna et al. [2011] integrated field and satellite information to better characterize the TGSD of the May 2010 Eyjafjallajökull eruption, which had a relatively large very fine ash population [Costa et al., 2016a]. Motivated by their results, we aim at reconstructing the entire TGSD (including PM_{10}), integrating field measurements and satellite-based observations of the 23rd February 2013 Etna paroxysm.

At Etna, more than 200 lava fountains occurred from the new south-east crater (NSEC) between 1995 and 2014 [Andronico et al., 2014b; De Beni et al., 2015; Corsaro et al., 2017]. Most eruption columns reached several kilometres high releasing ash into the atmosphere. The

prevailing easterly winds over the Etnean region [Barsotti et al., 2010; Scollo et al., 2013] dispersed the tephra downwind over the Ionian Sea. Consequently, the narrow land surface (i.e. 5-20 km eastwards from the source) affects the sampling area, and therefore the field-derived TGSD. Andronico et al. [2014a] demonstrated how an incomplete field dataset for Etna (e.g. location and spatial distribution) influences the TGSD estimation and the TEM retrieval. In addition, Azzopardi et al. [2013] showed an incorrect ESP assessment may also impact the forecast of the plume transport over neighbouring countries, such as the Maltese Islands.

On 23rd February 2013, the eruption dispersed tephra fallout north-eastward permitting sampling from the proximal volcanic slopes to Brindisi (Puglia region) about 410 km from the source (Figure IV.1 and Table IV.1). In the literature, only a few studies on Etna eruptions used similar distal field observations [Dellino and Kyriakopoulos, 2003], but the paucity of data prevented using within the TGSD calculation. Here, starting from the field-derived TGSD for the 23rd February 2013 paroxysm, we inverted the PM$_{10}$ fraction required within the TGSD for numerically reconstructing simultaneously the tephra loading and far-travelling airborne ash mass. Simulations were run coupling FPlume [Folch et al., 2016] with the FALL3D tephra dispersal model [Costa et al., 2006; Folch et al., 2009]. Simulation input parameters (ESP) were inverted by best-reproducing field and satellite retrievals.

Worldwide high time-resolution satellite coverage allows most eruptive processes to be recorded [Gouhier et al., 2016]. Geostationary platforms (e.g. MSG) are particularly suited to rapidly evolving volcanic plume observations [Prata and Kerkmann, 2007] with an acquisition frequency of up to 1 image every 5 minutes with the rapid scan service. In addition to satellite data, the ground-based AERONET is used to validate the satellite retrievals and simulations of ultra-fine particles (i.e. few μm) [Folch et al., 2012]. Although combining data from different instruments is challenging due to their own operative window, this work aims to show that an integrated multi-disciplinary approach is necessary for better assessing the TGSD, which is pivotal for air traffic safety [e.g. Folch et al., 2012; Beckett et al., 2015]. Indeed, improving ash plume characterization in terms of ash concentration and dispersion is highly relevant for the VAACs and the pilots to prevent ash encounters. As testified by several cases worldwide in the last 30 years [Prata, 1989a; Casadevall, 1994; Casadevall et al, 1999; Grindle and Burcham, 2003; Guffanti et al., 2005], the data can be used for delimiting the no-fly zones, helping the decision makers, such as those working in the VAACs. Considering there is no operational single-method capable of describing fully the volcanic eruption processes, tracking the plume and assessing the ESPs, their estimation can only be obtained through a synergetic integrated approach.
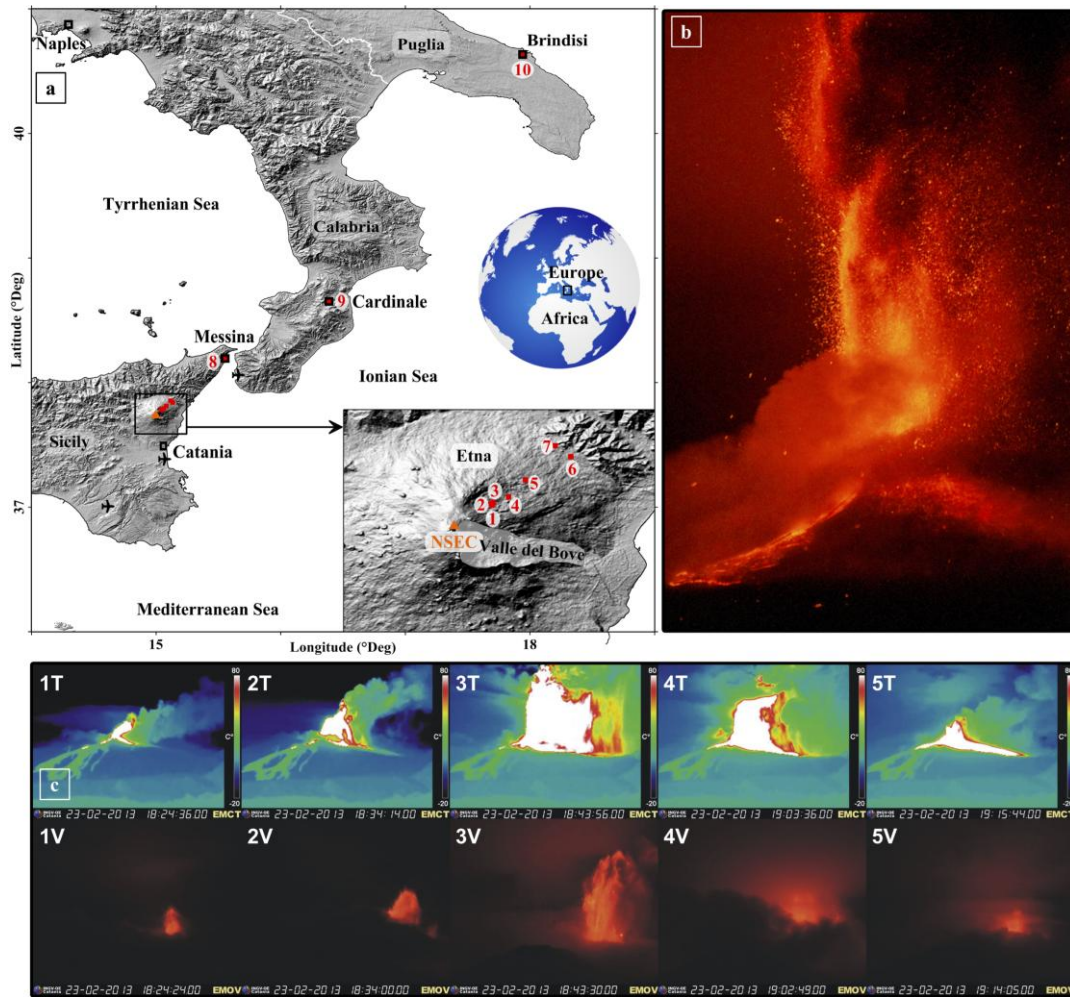
Figure IV.1: a) The Italian regions (i.e. Sicily, Calabria and Puglia) affected by tephra fallout of the 23rd February 2013 Etna paroxysm. NSEC stands for new south-east crater from which the eruption occurred. Red numbers refer to the sample sites, whereas the aircraft symbols localize the Fontanarossa (Catania), the Pio La Torre (Sicily), and the Tito Minniti (Calabria) airports. The inset zooms on Etna indicating the proximal samples (details in Table IV.1). b) Photograph of the eruption. Courtesy of Marco Neri c) Time-series pictures of the eruption in thermal (1T – 5T) and visible (1V – 5V) spectrum. Source: INGV – OE.

To provide alerts of volcanic activity in support of air traffic safety, the nine VAACs use operational VATD models, such as 1) NAME [Witham et al., 2007; Beckett et al., 2014] for the London VAAC, 2) MOCAGE-accident [Sič et al., 2015] for the Toulouse VAAC, and 3) FALL3D for the Buenos Aires and Darwin VAACs. However, their initializations commonly use simplified TGSD. For example, NAME assumes a standard grain-size distribution from a pre-existing eruption [Maryon et al., 1999], arbitrarily considering 5 wt% in weight of the TEM for the fine ash content.

Besides the aviation hazard, volcanic ash also affects populations living near active volcanoes [e.g. Sulpizio et al., 2012]. In particular, PM_{10} has respiratory health effects even for eruptions produced by Etna [e.g. Horwell et al., 2007; 2013; 2017; Rose and Durand, 2009; Andronico and Del Carlo, 2016; Tomašek et al., 2016].

The paper describes, first, the 23rd February 2013 eruption features. Then, the modelling approach is followed by the methodology used to reconstruct the TGSD and assess the best ESPs. We report the different dataset used (i.e. field, satellite and ground-based) prior to presenting and discussing the results.

	Field Observations					Computed Loading (kg/m^2)			
Sample	Location	Longitude	Latitude	Mode (Φ)	Loading (kg/m^2)	Field TGSD	bi-Gaussian TGSD	bi-Weibull TGSD	Fine Enriched TGSD
1	Baracca	15.042	37.782	-3.5	2.1×10^1	4.5×10^0	7.6×10^0	6.5×10^0	4.5×10^0
2	Casetta	15.041	37.784	-4.0	5.9×10^0	4.5×10^0	7.7×10^0	6.6×10^0	4.6×10^0
3	Bivio-007	15.044	37.786	-4.0	5.5×10^0	4.7×10^0	7.9×10^0	6.8×10^0	4.7×10^0
4	Forestale	15.061	37.792	-3.5	2.2×10^1	5.1×10^0	8.5×10^0	7.3×10^0	5.1×10^0
5	Chalet	15.081	37.813	-2.5	3.2×10^1	6.1×10^0	9.6×10^0	8.4×10^0	6.1×10^0
6	Castiglione	15.114	37.854	-1.5	5.2×10^0	8.0×10^0	1.1×10^1	9.5×10^0	8.1×10^0
7	Linguaglossa Out	15.133	37.840	-3.0	1.2×10^0	8.4×10^0	1.1×10^1	1.0×10^1	8.5×10^0
8	Messina	15.554	38.195	1.0	2.9×10^{-1}	1.2×10^0	1.1×10^0	9.4×10^{-1}	1.3×10^0
9	Cardinale	16.384	38.650	2.0	1.3×10^{-2}	3.9×10^{-2}	2.0×10^{-2}	2.2×10^{-2}	4.0×10^{-2}
10	Brindisi	17.941	40.634	3.0	1.4×10^{-3}	1.8×10^{-3}	1.5×10^{-4}	5.4×10^{-4}	1.8×10^{-3}

Table IV.1: List of the collected samples with their numerical results for each input TGSD. Sampling includes locations, tephra loadings, and modes. The computed loadings result from the use of the Field, bi-Gaussian, bi-Weibull, and Fine Enriched TGSDs (Figure IV.4).

Chronology of the 23rd February 2013 eruption

On 23rd February 2013, an intense lava fountain took place at the NSEC (Figure IV.1b), which is the youngest and most active of Etna's craters [Behncke et al., 2014; Andronico et al., 2015]. The eruptive activity initiated with Strombolian explosions, which increased around 18:15 (all times are expressed in UTC) turning into lava fountaining (Figure IV.1c). The paroxysmal phase lasted 1 hour 6 minutes. Despite bad weather conditions (i.e. cloudy, windy and night) during the paroxysmal activity, images from INGV – OE showed the growth of incandescent lava jets higher than 500 m above the crater (Figures IV.1b and IV.1c), from which a buoyant plume developed up to ~9 km a.s.l. forming the umbrella region. Figure IV.2 shows the main meteorological profiles (e.g. temperature, air moisture, wind speed and direction), obtained from the European Center for Medium-range Weather Forecasts (ECMWF; ERA-Interim-

Reanalysis). Considering the time for the ash to be transported from NSEC to Brindisi (i.e. ~5h), the two profiles refer to 18:30 and 23:30, respectively. This study benefitted from atypical meteorological conditions in wind speed and direction during the eruption and the following hours, with similar patterns over NSEC and Brindisi. Indeed, the wind speed at 18:30 and 8.5 km a.s.l. is ~49.6 m/s and ~32.6 m/s over NSEC and Brindisi, respectively, whereas at 23:30, it is ~50.6 m/s and ~36.3 m/s. Such a context made sampling possible from Etna's slopes (5-16 km from the source) to Messina (~70 km) up to Calabria and Puglia regions (~160 and ~410 km, respectively). Field location and data are available in Figure IV.1 and Table IV.1 respectively.
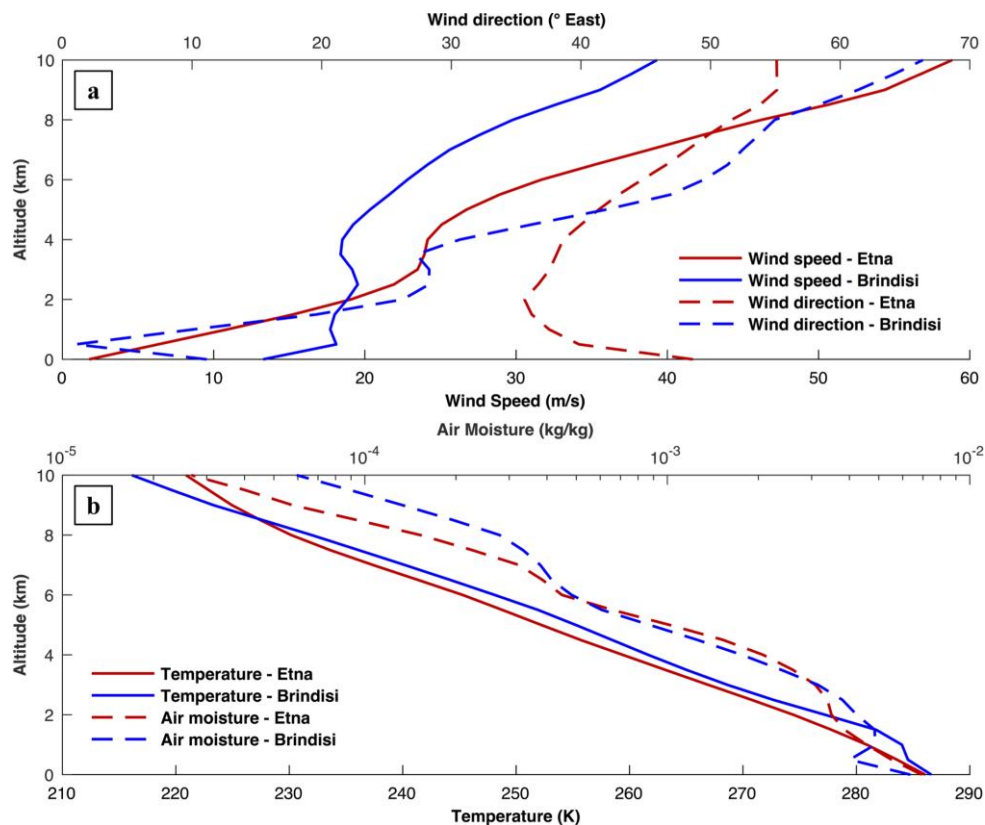
Figure IV.2: a) Wind direction and speed profiles above the NSEC and Brindisi at 18:30 and 23:30, respectively. b) Associated air moisture and temperature profiles. Data refer to the 23rd February 2013, which are provided by the ECMWF platform (ERA-Interim-Reanalysis).

In the deposit, we found lapilli up to 5-6 km from the vent (samples 1-7), coarse ash (i.e. 2-0.125 mm) in Messina (sample 8), fine ash with mode at 0.25 mm in Cardinale (sample 9), and the finest ash deposit in Brindisi (sample 10) with mode around 0.125 mm (details in Table IV.1). Geochemical analysis on several samples indicate a CaO/Al_2O_3 ratio in glass [Corsaro and Miraglia, 2013a] suggesting slightly different compositions from those measured during the 2011-2012 sequence [Behncke et al., 2014]. They also show more evolved magma than on the 23rd November 2013 [Corsaro and Miraglia, 2013b; Andronico et al., 2015].

Modelling approach: FPlume and FALL3D models

Tephra dispersal models are widely used in volcanology to quantify either the tephra loading (e.g. TEPHRA, Connor et al. [2001]; HAZMAP, Macedonio et al. [2005]; FALL3D, Costa et al. [2006]; Folch et al. [2009]), or the airborne volcanic ash (e.g. VOL-CALPUFF, Barsotti et al. [2008]; FALL3D). All tephra dispersal models need as input parameterizations of the source term (e.g. eruptive column, MER, TGSD). An overview of such models is available in Folch [2012], and Costa et al. [2016b].

This study uses FALL3D to compute the tephra dispersal and sedimentation by means of FPlume [Folch et al., 2016], which is a steady-state eruption column model based on the buoyant plume theory [Morton et al., 1956]. FPlume solves for 1D cross-section-averaged equations for mass, momentum and energy conservations, accounting for the effects of wind coupling, air moisture, particle re-entrainment, and ash aggregation under wet conditions. Within FALL3D, FPlume uses the TGSD together with the initial magma temperature and water content to provide the vertical particle distribution inside the column. Etna is a basaltic volcano producing magmas typically at 1300 K with ~2.5 % of magmatic water [Metrich and Rutherford, 1998; Metrich et al., 2004; Allard et al., 2005; Spilliaert et al., 2006; Carbone et al., 2015]. FPlume estimates the MER for a column height and a given wind profile by using two turbulent air entrainment coefficients (i.e. radial – α and cross-flow – β coefficients; Bursik [2001]; Suzuki and Koyaguchi [2015]). α is internally calculated (details in Kaminski et al. [2005]; Folch et al. [2016]), whereas β is poorly constrained [Costa et al., 2016b], being calibrated based on best-fitting the field measurements. Characterizing the source term through FPlume implies uncertainties associated with the input parameters [Macedonio et al., 2016].

The 3D time-dependent Eulerian FALL3D model solves a set of advection-diffusion-sedimentation equations over a structured terrain-following grid using a finite difference method [Costa et al., 2006; Folch et al., 2009]. Besides the ESPs, FALL3D requires the time-dependent meteorological fields across the computational domain (Figure IV.1). For the simulated period (i.e. from 00:00 on 23rd February up to 00:00 on 29th February 2013), ECMWF meteorological data were obtained every 6 hours for 37 pressure levels (i.e. from 1000 to 1 mb) at 0.75° horizontal resolution. It is worth noting that the resolution is too low for capturing the orographic effects, which can be very important at local scale (e.g. around Etna's slopes) affecting the tephra loading [Watt et al., 2015]. FALL3D uses an internal meteorological grid interpolated here at 4-km resolution (the grid mesh is displayed in Figure IV.S1 in the Supplement. Although gravity currents in the umbrella region are not significant for such a small eruption [Costa et al., 2013], the simulations accounted for these effects. Ash aggregation, assumed negligible in terms of mass, was also investigated following a scheme based on a simplified solution of the Smoluchowski equation [Smoluchowski, 1917] proposed by Costa et al. [2010]. Aggregation scheme uses a fractal relationship of the number of primary particles within an aggregate together with the effects of both magmatic water and air moisture [Folch

et al., 2010; 2016]. Further description of the models and the parameterizations used for ash aggregation are available in Poret et al. [2017].

Observational data and methodology

The methodology proposed here brings together field and satellite data to reconstruct the initial grain-size distribution in the plume before sedimentation (i.e. input TGSD). A summary of the input parameters is available in Table IV.2. As first step, we used the field samples to retrieve the TGSD. Then, the TGSD was parameterized using lognormal and Weibull distributions [Costa et al., 2016a; 2017]. ESP were inverted by capturing the measurements. Finally, the field-based TGSD was extrapolated for implementing the very fine ash distribution through an analytical parameterization. Satellite retrievals were used to invert the PM_{10} fraction by best-fitting the simulated distal airborne ash mass. We also validated the results by analyzing the ultra-fine ash dispersal with the AERONET data.

Parameter	Explored Range	
Column height (km above vent)	3	10
MER (kg/s)	10^3	10^8
Exit velocity (m/s)	150	300
Exit water fraction (%)	0.5	3.2
Cross-flow entrainment coefficient (β)	0.3	1.0
Aggregate diameter (Φ_{Agg})	1	2.5
Density aggregates (kg/m^3)	200	1200

Table IV.2: List of the input parameters for FPlume and FALL3D modelling with their ranges. Other options and models are described in Appendix IV.A.

Field data analysis

Few hours after the eruption, tephra was sampled at 10 different locations (Figure IV.1). Prior to analysis, loading per unit area was measured and samples were oven-dried at 110°C for 12 hours at the sedimentology laboratory of the INGV – OE. Then, GSD was retrieved from -5 to 5 Φ (at 0.5 Φ interval) by sieving (via a Retsch vibratory sieve shaker AS 200 Basic). The farthest sample (i.e. n°10 in Figure IV.1) contains only small fine ash (i.e. d $\geq$ 2 Φ) preventing sieve analysis. The GSD was given by the CAMSIZER (Retsch) instrument, which has the same range size limit as sieve [Lo Castro and Andronico, 2008]. Andronico et al. [2014a] validated their alternative use showing the good match between the two methods above for grain-size analysis purpose. The field GSDs indicate a clear decay in size from proximal to distal areas and an increase in tephra sorting with distance (Figure IV.3). They also show unimodal behaviour, peaking at -4 Φ for medial locations and 3 Φ for the distal ones (Table IV.1).
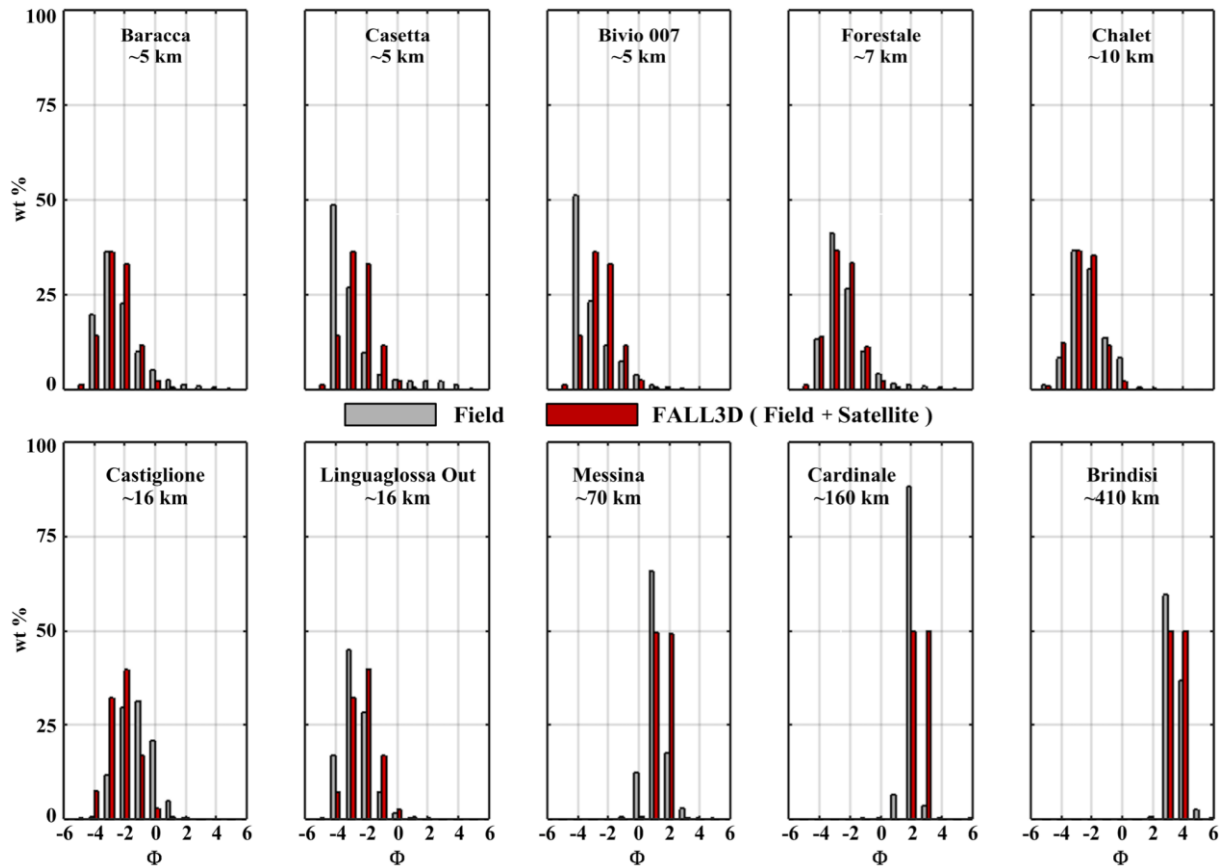
Figure IV.3: Individual field GSDs of the 10 samples together with the ones computed by considering both field and satellite observations (i.e. Fine Enriched TGSD).

Besides GSD, we used the field data to estimate the total mass of the deposit using the method of Bonadonna and Costa [2012; 2013], which is based on the Weibull distribution of the deposit thinning. The resulting field-derived TEM estimate yields $\sim 2.0 \pm 0.5 \times 10^9$ kg.

Satellite data (SEVIRI)

We used data from the SEVIRI sensor providing image every 15 minutes at a spatial resolution of $\sim 3 \times 3$ km at nadir. Satellite data were acquired from HOTVOLC [Gouhier et al., 2016]. During the 23rd February 2013 Etna eruption, the volcanic cloud was tracked in the SEVIRI data in terms of airborne ash mass (hereinafter AAM; in kg) over hundreds of kilometres. SEVIRI level 1.5 data recorded by the HOTVOLC system were initially converted into calibrated spectral radiance (in $Wm^{-2}sr^{-1}\mu m^{-1}$). Then, following the methodology described above [Wen and Rose, 1994; Guéhenneux et al., 2015], we provide the cloud top temperature (°C), altitude (m a.s.l.), AAM (kg), and r_e (μm) from 19:00 – 20:15.

AERONET data

The 23rd February 2013 Etna paroxysm released very fine ash towards south-eastern Europe. Among the AERONET sites, the station located at Çamlıbel, Turkey (station labelled IMS-METU ERDEMLI, ~1700 km from Etna) detected particles from 24th – 26th February 2013. Unfortunately, the eruptive period overlapped with a substantial re-suspension of Saharan dust from 20th – 23rd February 2013. Even though the dust storm was in a final stage, the presence of airborne mineral dust affected the AOD retrieved over the station. To assess the volcanic ash AOD, we subtracted the dust contribution estimated from the Goddard Earth observing system (GEOS-chem) model [Bey et al., 2001; Park et al., 2004; Fairlie et al., 2007; Chan and Chan, 2017]. Although such approach introduces a large uncertainty in the retrieval, we bear in mind that data were used to validate the satellite observations only by verifying if the input TGSD permits the reproduction of the ultra-fine ash dispersal at ~1700 km from the source. Indeed, we compared the computed volcanic ash AOD (FALL3D) with the AERONET measurements.

TGSD estimation

Making use of the 10 field GSDs, the field-derived TGSD (hereinafter Field TGSD; Figure IV.4) is estimated through the Voronoi tessellation method [Bonadonna and Houghton, 2005]. Regarding the spatial distribution of the samples, the Field TGSD suffers from the lack of field data, especially at medial and distal locations. Consequently, it cannot fully represent the initial magma fragmentation but only an estimation with, for the first time on Etna, medial and distal measurements. Figure IV.4a shows the bimodality of the Field TGSD with a first mode (i.e. the coarse sub-population) around -3 Φ and a second mode (i.e. the fine sub-population) around 0.5 Φ. To reproduce the Field TGSD in a simple parametric way and extrapolate to the very fine ash fraction, we describe the TGSD as the sum of two lognormal distributions (bi-Gaussian in Φ, hereinafter bi-Gaussian distribution), and two Weibull distributions (hereinafter bi-Weibull distribution).

The related equations are available in Section I.4 (Equations. I.2 and I.3; Costa et al. [2016a; 2017]). Best-fitting parameterizations are reported in Table IV.3. The cases well-characterized in terms of fine ash fraction indicate that a lognormal distribution tends to under-estimate the fine ash distribution [Costa et al., 2016a]. This becomes significant for TGSD produced by Etna eruptions, as most of the fine ash is typically not sampled. In the latter case, Costa et al. [2016a; 2017] demonstrated a better quantification of the fine ash fraction is given by the bi-Weibull distribution.
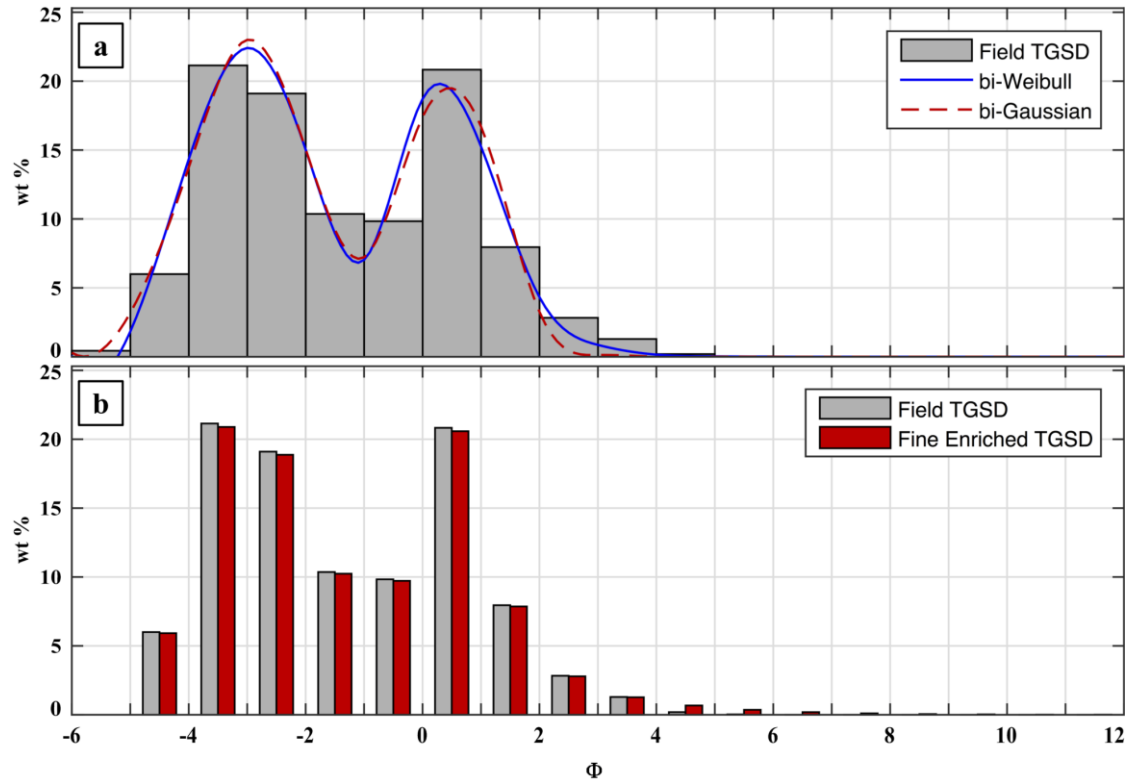
Figure IV.4: Summary of the input TGSDs used within the simulations. a) Field TGSD together with its best-fitting analytical curves (bi-Gaussian and bi-Weibull distributions; details in Table IV.3). b) Fine Enriched TGSD obtained from the Field TGSD by modifying empirically the fine ash distribution.

bi-Gaussian distribution		bi-Weibull distribution	
μ_1	-2.96 ± 0.07	λ_1	-3.28 ± 2.84
σ_1	1.03 ± 0.07	n_1	1.68 ± 0.24
μ_2	0.49 ± 0.07	λ_2	-1.25 ± 1.07
σ_2	0.79 ± 0.06	n_2	0.77 ± 0.16
p	0.59 ± 0.03	q	0.39 ± 0.06

Table IV.3: Parameterization of the analytical distributions obtained in best-fit of the Field TGSD. Values are expressed in Φ-units. The lognormal distribution is described through the coarse sub-population fraction (p), the means of the coarse- and fine-grained sub-populations (μ_1 and μ_2, respectively), and their standard deviations (σ_1 and σ_2, respectively). The Weibull distribution is constructed with the coarse sub-population fraction (q), the scale parameters of the means of the coarse- and fine-grained sub-populations (λ_1 and λ_2, respectively), and the shape parameters of the means of the coarse- and fine-grained sub-populations (n_1 and n_2, respectively).

Neither the Field TGSD, the bi-Gaussian, nor the bi-Weibull distributions (Figure IV.4) permit to capture numerically the satellite retrievals. We assume this is due to the missing information relative to the very fine ash (PM$_{10}$, i.e. $\Phi \geq 6$), or the lognormal shape given to the partial GSD into the satellite data. Indeed, the long atmospheric residence time of the PM$_{10}$, for negligible ash aggregation, prevents a rapid deposition [Rose and Durant, 2009]. To account for PM$_{10}$ within the TGSD, without accurate satellite-derived GSD, we opted for an empirical modification of the Field TGSD to enrich in fines the corresponding classes (i.e. $\Phi \geq 5$; Figure IV.4b). Indeed, we assume that for a limited range within the TGSD (i.e. PM$_{10}$), the lognormal distribution can approximate the empirical distribution we used for characterizing the PM$_{10}$. For the sake of simplicity, we used an empirical power-law dependence of the fraction with Φ according to the relationship:

$$X(\Phi_i) = X(\Phi_4) \times \gamma^{(\Phi_i - \Phi_4)}, \Phi \geq 5$$

(IV.1)

where $X(\Phi_i)$ is the fraction (in wt%) allocated to the ith bin, $X(\Phi_4)$ is the fraction obtained for $\Phi = 4$, and γ is the empirical factor ($\gamma < 1$). Although PM$_{10}$ refers to $\Phi \geq 6$, the Field TGSD does not permit calculating from $\Phi = 5$ implying to start at $\Phi = 4$ (see Figure IV.4b). The PM$_{10}$ fraction required into the TGSD was inverted exploring γ between 0.5 and 0.7, which corresponds to a PM$_{10}$ fraction of 0.3-1.3 wt%. This empirical procedure aims at proposing the input TGSD (hereinafter Fine Enriched TGSD; Figure IV.4b) capable to account for both field and satellite data. γ is estimated best-fitting the simulated AAM with the satellite retrievals.

Inverse problem-solving methodology

The invers problem presented above is solved carrying out hundreds of simulations to explore the input parameter ranges (Table IV.2 and Appendix IV.A for further parameterizations). Although more sophisticated Bayesian approaches can be used to deal with atmospheric observations [e.g. Twomey, 1996; Rodgers, 2000], the quantity and quality of the available data in terms of tephra loading and airborne ash mass motivated the inversion by means of simple statistical metrics as in similar studies [e.g. Folch et al., 2010; Costa et al., 2012; 2014; Martí et al., 2016; Poret et al., 2017]. By means of the following analyses, we aim at suggesting a simple method for integrating the data and assessing the reflecting ESP. However, when the data make it possible, more sophisticated comparison can be used [e.g. Wilkins et al., 2016].

We initiated the inversion procedure by optimizing the simulations best-fitting the observed tephra loadings. For this purpose, we used a goodness-of-fit criterion evaluated through different statistical metrics [Poret et al., 2017]. One was the normalized root mean square error (i.e. *RMSE*) calculated on the basis of two different weighting factors for the computed tephra loadings (i.e. *RMSE$_1$* and *RMSE$_2$*; equations and explanation in Appendix IV.B). Besides

RMSE, we measured the goodness-of-fit and uncertainty of the simulated tephra loadings through the statistical indexes *K* (i.e. geometric average of the distribution) and *k* (i.e. geometric standard deviation of the distribution) introduced by Aida [1978]:

$$K = exp\left[\frac{1}{N}\sum_i^N \log\left(\frac{Obs_i}{Sim_i}\right)\right]$$

(IV.2)

$$k = exp\left[\sqrt{\frac{1}{N}\sum_i^N \log\left(\frac{Obs_i}{Sim_i}\right)^2 - \left(\frac{1}{N}\sum_i^N \log\left(\frac{Obs_i}{Sim_i}\right)\right)^2}\right]$$

(IV.3)

Making use of such criteria, the simulations are considered reliable when *K* lies between 0.95 and 1.05 (i.e. ±5% of the best theoretical mass estimation based on the sampled tephra loadings). In other words, a value of *K* = 0.95 indicates a 5% over-estimation of the TEM for a given set of ESPs, whereas *K* = 1.05 gives an under-estimation of 5%. The best simulations are selected when *k* is minimized. Additionally, we calculated also the *bias* (to be minimized), the *correlation* (to be maximized) and the Student T test (hereinafter *TTest*) [Folch et al., 2010].

To reproduce the tephra loading, we ran a set of simulations varying the parameters at constant steps within their ranges (Table IV.2). Then, we refined by means of a finer step around the best cases to optimize the goodness-of-fit. We started with the column height by changing the values from 6 to 13 km a.s.l. using the relationship between the column height and the MER [Folch et al., 2016]. The latter was investigated iteratively between 10^3 and 10^8 kg/s. Then, the exit velocity and the magma water content were explored from 150 to 300 m/s and 0.5 to 3.2%, respectively. Regarding the FPlume inputs to compute the air entrainment, β was sampled from 0.3 to 1.0. The aggregation parameterization was explored by considering the aggregate diameter (Φ_{Agg}) and density from 1 to 2.5 Φ and 200 to 1200 kg/m^3, respectively.

The methodology described above gives similar tephra loadings through diverse input combinations, which indicates non-uniqueness of the solution [Connor and Connor, 2005; Scollo et al., 2008; Bonasia et al., 2010; Anderson and Segall, 2013].

Regarding the satellite retrievals, the PM$_{10}$ fraction was inverted by quantitatively comparing the retrieved whole ash mass contained within the volcanic cloud (SEVIRI) with the simulated total AAM (in kg). We applied the same statistical method to the observed airborne PM$_{10}$ masses (Section TGSD estimation) than for field measurements.

Results

The following section describes the best-fit results of tephra loading and airborne ash dispersal. First, we summarize the results of the Fine Enriched TGSD. Then, we report the ESPs retrieved for the explored input TGSDs. The last sections refer to the validation of the reconstruction of the main eruption features by means of field, satellite and AERONET observations, respectively.

ESP estimation solving the inverse problem

Regarding the tephra loading, Table IV.4 reports the results of the statistical analysis for the input parameter ranges (Table IV.2) with the different TGSDs. They indicate a minimum value of $k = 2.96$ associated with the bi-Weibull distribution, whereas the Field, bi-Gaussian and Fine Enriched TGSDs yield $k = 3.36$, $k = 3.37$, and $k = 3.37$, respectively. Additionally, the $RMSE_1$ and $RMSE_2$ show similar values with a slight better performance for the bi-Weibull distribution. In other words, without considering other observations than the tephra loadings, the goodness-of-fit method presents the bi-Weibull distribution as best input TGSD for the simulations. The statistical values (Table IV.4) indicate an uncertainty on the TEM estimation of about a factor 2-3, similar to other classical methods [Bonadonna and Costa, 2012; 2013; Bonadonna et al., 2015c].

Input Parameter	Field TGSD	bi-Gaussian TGSD	bi-Weibull TGSD	Fine Enriched TGSD	
Column height (km above vent)	5.5	5.5	5.5	5.5	5.5
MER (kg/s)	1.2×10^6	1.4×10^6	1.3×10^6	1.3×10^6	1.3×10^6
Exit velocity (m/s)	250	250	250	250	250
Exit temperature (K)	1300	1300	1300	1300	1300
Exit water fraction (%)	2.5	2.5	2.5	2.5	2.5
Cross-flow entrainment coefficient (β)	0.53	0.55	0.53	0.54	0.54
Diameter (Φ_{Agg})	—	—	—	—	2
Density aggregates (kg/m^3)	—	—	—	—	1000
Statistical metric					
$RMSE_1$	0.80	0.70	0.73	0.80	0.80
$RMSE_2$	2.28	2.84	2.46	2.31	2.31
K	1.00	1.01	0.99	0.99	0.99
k	3.36	3.58	2.96	3.37	3.37
Bias	0.0	0.0	0.0	0.0	0.0
Correlation	0.9	0.9	0.9	0.9	0.9
TTest	1.0	1.0	1.0	1.0	1.0

Table IV.4: Best input ESP and the corresponding statistical analysis for the tested TGSDs. Ash aggregation is investigated for the Fine Enriched TGSD with the scheme in Costa et al. [2010].

The absence of PM_{10} within the Field, bi-Gaussian, and bi-Weibull TGSDs (Figure IV.4) motivated to empirically modifying the Fine Enriched TGSD (Section TGSD estimation and Figure IV.4). The comparative results for the PM_{10} fractions (i.e. 0.3-1.3 wt%) are reported in Table IV.5. They revealed a systematic AAM over-estimation compared to the satellite retrievals (Table IV.6) for fractions higher than 0.5 wt%. The statistical analysis (Section Inverse method and Appendix IV.B) indicates a best TGSD with 0.4 wt% of PM_{10} (i.e. γ = 0.53) to reproduce the AAM. Indeed, Table IV.5 shows for γ = 0.53 a K index close to 1 and a minimum k around 1.3 (the *RMSEs* are also near the minimum). It follows we selected the Fine Enriched TGSD modified with γ = 0.53 (i.e. PM_{10} = 0.4 wt%). However, such a fraction does not permit the numerical reproduction of the maxima AAM per unit area, which is captured with a PM_{10} fraction of 1.3 wt% (i.e. γ = 0.70; Figure IV.S2 in the Supplement).

	Fine Enriched TGSD with:					
γ	0.50	0.53	0.55	0.60	0.65	0.70
PM_{10} (in wt%)	0.3	0.4	0.5	0.7	0.9	1.3
Time (UTC)	**Airborne Ash Mass (AAM; in kg)** *(Computed AAM/Observed AAM)*					
19:00	1.0×10^7 *(2.62)*	1.3×10^7 *(3.43)*	1.6×10^7 *(4.16)*	2.3×10^7 *(5.84)*	3.3×10^7 *(8.49)*	4.7×10^7 *(12.16)*
19:15	1.4×10^7 *(0.98)*	1.8×10^7 *(1.30)*	2.1×10^7 *(1.48)*	3.1×10^7 *(2.24)*	4.4×10^7 *(3.11)*	6.3×10^7 *(4.47)*
19:30	1.3×10^7 *(0.60)*	1.7×10^7 *(0.79)*	2.0×10^7 *(0.95)*	2.8×10^7 *(1.34)*	4.1×10^7 *(1.96)*	5.6×10^7 *(2.69)*
19:45	1.2×10^7 *(0.62)*	1.6×10^7 *(0.84)*	1.9×10^7 *(1.01)*	2.8×10^7 *(1.46)*	3.9×10^7 *(2.07)*	5.4×10^7 *(2.84)*
20:00	1.1×10^7 *(1.00)*	1.5×10^7 *(1.39)*	1.8×10^7 *(1.62)*	2.7×10^7 *(2.49)*	3.8×10^7 *(3.44)*	5.4×10^7 *(4.93)*
20:15	1.1×10^7 *(2.21)*	1.5×10^7 *(3.08)*	1.8×10^7 *(3.64)*	2.6×10^7 *(5.31)*	3.7×10^7 *(7.80)*	5.1×10^7 *(10.65)*
Statistical metric						
RMSE₁	0.33	0.24	0.29	0.79	1.47	2.45
RMSE₂	0.28	0.28	0.39	1.01	1.77	2.90
K	1.28	0.96	0.81	0.55	0.39	0.28
k	1.28	1.29	1.26	1.30	1.28	1.31
Bias	0.0	0.0	0.0	0.0	0.1	0.1
Correlation	0.3	0.1	0.5	-0.1	0.3	-0.1
TTest	0.2	0.8	0.2	0.0	0.0	0.0

Table IV.5: Computed airborne ash mass time-series for different γ together with the statistical analysis. Airborne ash masses are computed for different γ values used to produce the Fine Enriched TGSD. Parenthesis refer to the ratio between computed and measured ash masses.

Regardless of the TGSD used, the simulations return a column height of ~8.7 km a.s.l., which is consistent with the *in-situ* observations (i.e. ~9 km a.s.l.) from INGV – OE (Figure IV.1c). The relationship between the column height and the MER gives very similar values of MER: 1.2×10^6, 1.4×10^6, 1.3×10^6 and 1.3×10^6 kg/s for the Field, bi-Gaussian, bi-Weibull and Fine Enriched TGSDs, respectively. The inverted exit velocity is obtained at 250 m/s, being similar to the value observed by Donnadieu et al. [2016]. The β entrainment coefficient is calibrated by comparing both TEM released during the eruption (i.e. *K* optimization) and mean MER estimated from the column height by using FPlume. The resulting β values range from 0.53 to 0.55, which are similar to the value estimated by Devenish et al. [2010].

Time (UTC)	19:00	19:15	19:30	19:45	20:00	20:15
Cloud top temperature (°C)	-54.2	-53.5	-53.5	-53.8	-49.9	-48.6
Cloud top altitude (m a.s.l.)	9321	9167	9167	9167	8839	8678
Airborne ash mass (kg)	3.9×10^6	1.4×10^7	2.1×10^7	1.9×10^7	1.1×10^7	4.8×10^6
Mean effective radius (µm)	4.33	4.13	4.24	4.21	4.58	4.71

Table IV.6: Time-series of the main satellite retrievals. Retrievals derived from SEVIRI data and come from 15-minute internal observation.

Tephra loading validation against field observations

Figure IV.5 compares the 10 tephra loadings measured at the sampled sites with the simulated values obtained for the Field, bi-Gaussian, bi-Weibull, and Fine Enriched TGSDs. The sensitivity to the input TGSD can be seen from both Table IV.1 and Figure IV.5. Regardless of the TGSD, the 10 simulated values lie within a factor of 10 the measurements. In particular, 8 of the 10 loadings are between 1/5- and 5-times the observed values. The computed values of the proximal samples (labels 1-7) range between ~11 and ~4.5 kg/m^2, showing a narrower span than the field samples (~32 to ~1.2 kg/m^2). Medial samples (labels 8 and 9 in Figure IV.5) are slightly over-estimated. The farthest sample (label 10 in Figure IV.5) is either over-estimated or under-estimated tephra loading, depending on the input TGSD. Proximal samples show a slight enrichment in coarse material for the bi-Gaussian distribution than the other TGSDs (Figure IV.4), explaining the larger tephra loading estimates. In contrast, the lack of fine particle results on under-estimating in load the farthest sample of about a factor 10.
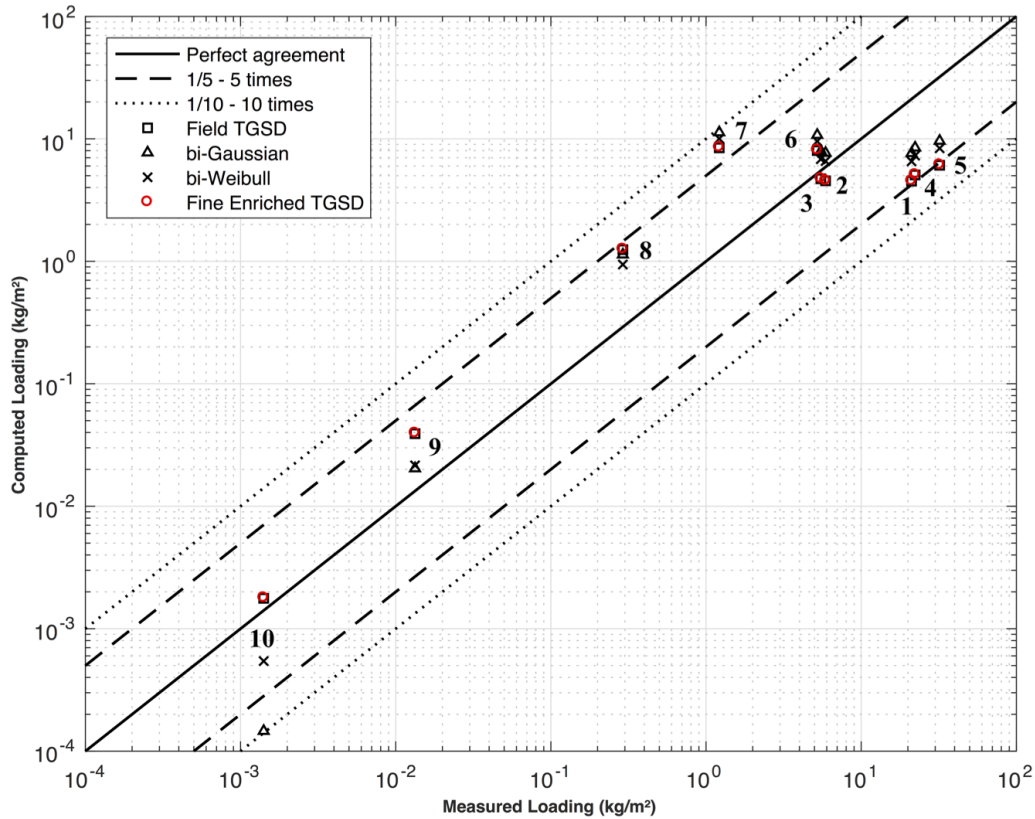
Figure IV.5: Observed tephra loadings versus computed data at 10 observation sites for the different input TGSD's used within the modelling simulations (details in Table IV.1). The typical errors are assumed of ~5-20% as described in Bonadonna et al. [2015c].

Figure IV.6 displays the tephra loading maps obtained with the four input TGSDs. It shows the bi-Gaussian and bi-Weibull distributions fail to reproduce the tephra loading up to distal areas, whereas the maps associated with the Field and Fine Enriched TGSDs capture reasonably well all sites (Table IV.1). The corresponding time evolution of the tephra loading for the Fine Enriched TGSD is available in the Supplement (Animation IV.A1).

Considering an eruption duration of 1 hour and 6 minutes through a constant eruptive phase (i.e. a unique column height), FPlume estimated the MER, which is used to assess the TEM. The optimal simulations selected for the different input TGSDs yield a TEM of 4.8×10^9, 5.3×10^9, 4.8×10^9, and 4.9×10^9 kg for the Field, bi-Gaussian, bi-Weibull and Fine Enriched TGSDs, respectively. The numerical TEM estimations are of the same order of magnitude than the field-derived TEM (i.e. ~$2.0 \pm 0.5 \times 10^9$ kg; Section Field data).
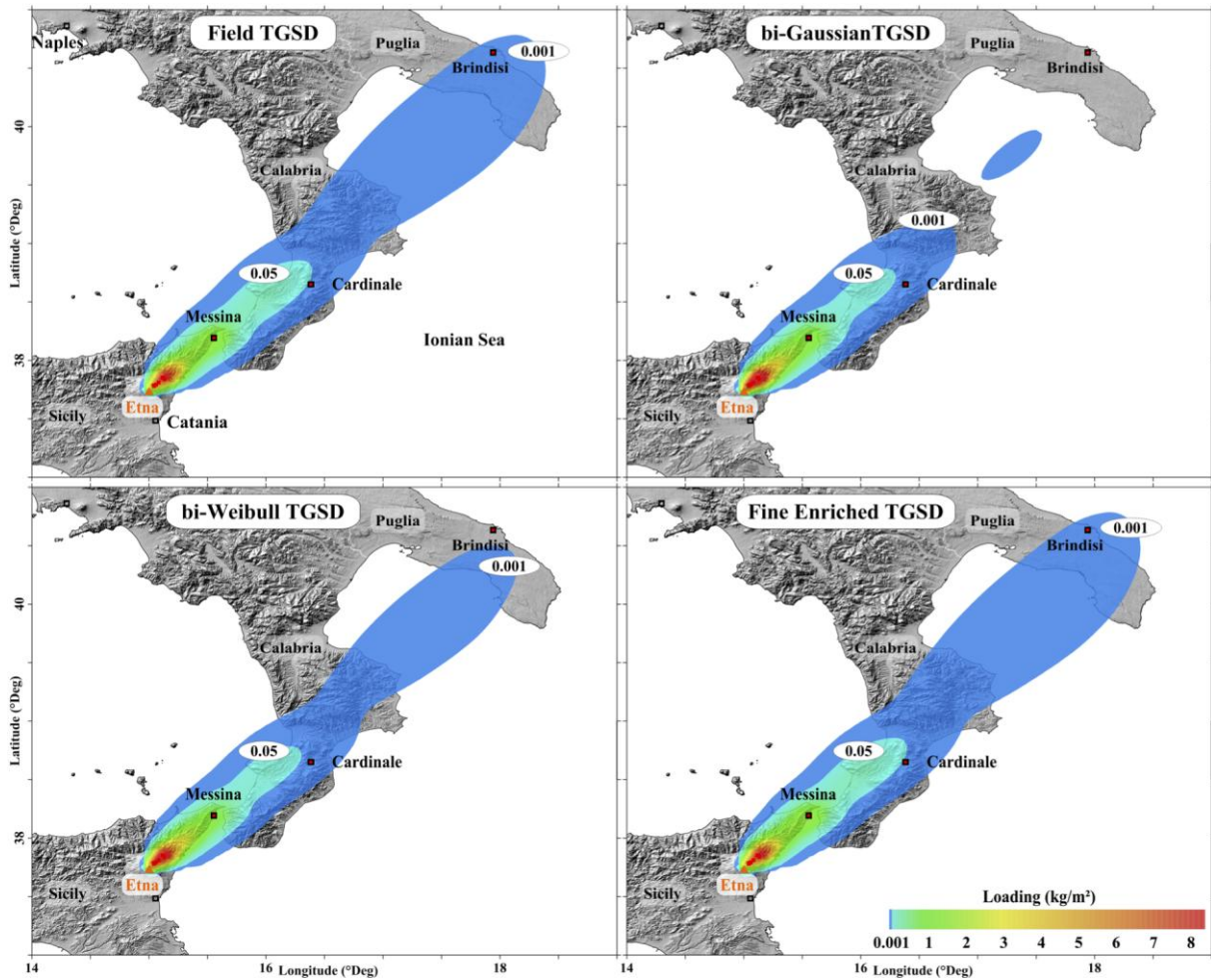
Figure IV.6: Tephra loading maps obtained for the different input TGSDs. Time-series for the Fine Enriched TGSD is available in the Supplement (Animation IV.A1).

PM$_{10}$ validation against satellite observations

Among the explored input distributions, only the Fine Enriched TGSD has enough PM$_{10}$ (here 0.4 wt%) to inject enough particles to reproduce the far-travelling airborne ash mass retrieved from satellite data (Table IV.6). The airborne ash dispersion is shown in Figure IV.7, where the FALL3D results (a – d) are compared with the SEVIRI retrievals (e – h). The first-time window (a, e in Figure IV.7; 19:15) refers to 1 hour after the paroxysm started. It shows the PM$_{10}$ fraction injected into the atmosphere spreading towards the Calabrian region. The volcanic cloud elevation estimated from the SEVIRI data indicates that it already reached its maximum altitude at ~9.3 km a.s.l. (Table IV.5). Hereinafter, we report the difference in terms of 1) total AAM and 2) maximum ash mass per unit area (all the values are reported in Table IV.4). At 19:15, the total AAM retrieved from SEVIRI returns 1.4×10^7 kg, whereas FALL3D estimates 1.8×10^7 kg (i.e. ~30% higher). The maximum ash mass per unit area measured from SEVIRI is ~22 g/m^2, while the computed value is ~12 g/m^2. The second-time window (19:30) illustrates the

dispersal over the Calabria 15 minutes later. The total AAM estimated from SEVIRI is 2.1×10^7 kg while the simulated value is 1.7×10^7 kg (i.e. under-estimation by ~21%). In this case, the maximum ash mass per unit area from SEVIRI (~20 g/m^2) is about three times the simulated value (~6 g/m^2). On the third-time window (19:45), satellite retrieval returns a total AAM of 1.9×10^7 kg, whereas FALL3D gives 1.6×10^7 kg (i.e. under-estimation by ~16%). The simulation of the maximum ash mass per unit area is about four times lower than the retrieved one (~5 g/m^2 vs. ~22 g/m^2, respectively). The last time window (d, h in Figure IV.7; 20:00) shows the volcanic ash cloud over the Ionian Sea at a slightly lower altitude (Table IV.5). The total AAM are 1.1×10^7 kg and 1.5×10^7 kg (i.e. over-estimation by ~39%) from SEVIRI and FALL3D, respectively. Again, the simulation of the maximum ash mass per unit area is about five times lower than the retrieved one (~4 g/m^2 vs. ~21 g/m^2, respectively). The full time-series of the airborne ash simulation is available in the Supplement (Animation IV.A2).

These results show that the simulation obtained using the Fine Enriched TGSD (Section TGSD estimation) reproduces AAM correctly but do not capture the local maxima. In general, the computed ash mass within the volcanic cloud (a – d in Figure IV.7) appears to be much more diluted than the satellite retrievals (e – h). From a computational point of view, to reproduce the correct local maxima, the input TGSD needs a PM$_{10}$ fraction about 3-times higher (i.e. 1.3 wt%). However, this implies an over-estimation of the total AAM by a factor 6 in average (see Figure IV.S2 in the Supplement).
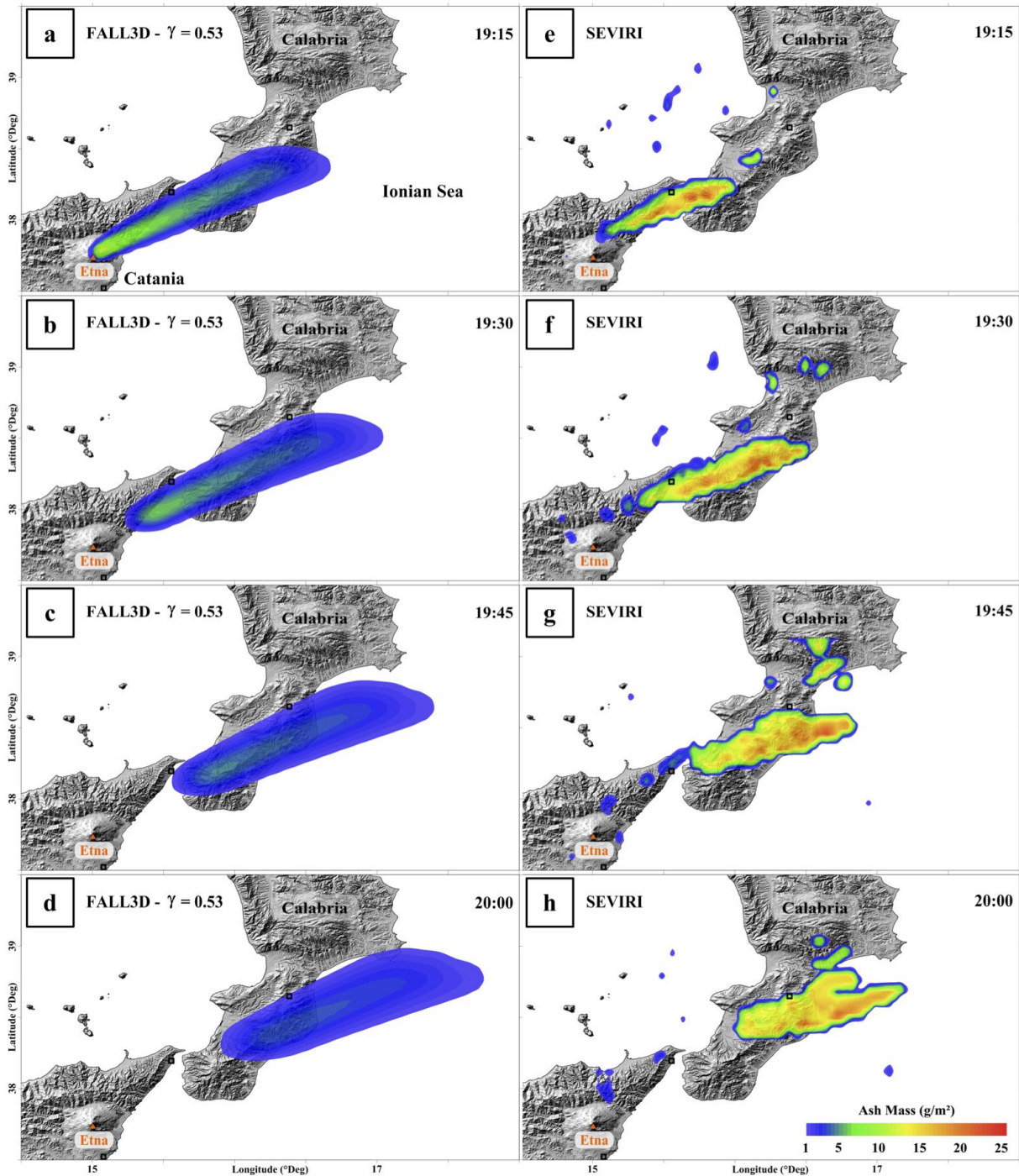
Figure IV.7: Airborne ash mass computed by FALL3D (a – d) and observed from satellite (e – h) from 19:15 – 20:00. Simulations correspond to the Fine Enriched TGSD obtained for γ=0.53. The time-series animation is available in the Supplement (Animation IV.A2).

AOD validation against AERONET observations

As an independent validation of the simulation results described above, we use the AOD measurements obtained from the AERONET [Holben et al., 1998]. On 24th February 2013, an AERONET station (Figure IV.8a) detected particles over the Çamlıbel village (Turkey; ~1700 km from Etna) from 06:58 – 11:58. To compare the retrieved AODs with the computed values associated with the presence of volcanic ash at such distal areas, we considered the data relative to non-spherical particles only, as described in Section AERONET data. From 06:58 – 10:58, the average particle sphericity is retrieved by AERONET between 0.3 and 3.9, whereas at 11:58 the value is 46.9 (hereinafter excluded). The corresponding AOD ranged between ~0.28-0.30 (hereinafter $AOD_{AERONET}$). As mentioned in Section AERONET data, we subtracted the Saharan dust contribution (i.e. ~0.23; GEOS-chem) from the $AOD_{AERONET}$ to assess the AOD associated with the volcanic ash over the Turkish station (hereinafter AOD_{ash}). The resulting AOD_{ash} ranges from ~0.05-0.07 (Figure IV.8b).
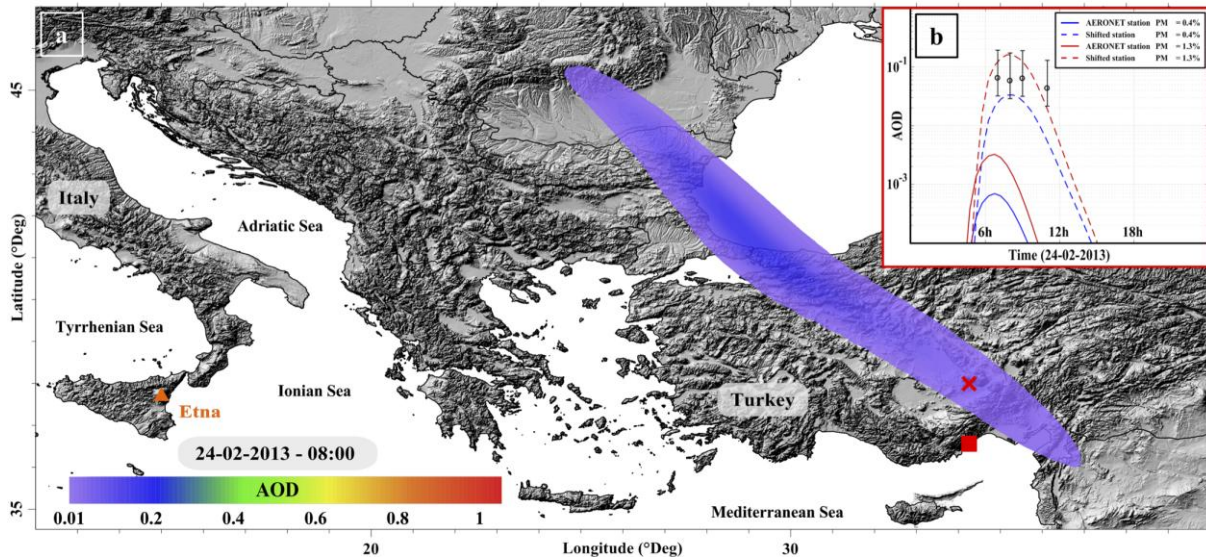
Figure IV.8: a) Simulated AOD of the 23rd February 2013 eruption for a computational domain extending over Turkey at 08:00 (24th February 2013). The time-series animation is available in the Supplement (Animation IV.A3). The red square refers to the AERONET station (labelled IMS-METU ERDEMLI), whereas the red cross is the virtual point located 2 grid-nodes northwards. b) AOD comparison between the AERONET measurements (circles) and the numerical results over both the AERONET station and the shifted station for PM_{10} fractions of 0.4 wt% and 1.3 wt%, respectively. The measurement uncertainty is estimated accordingly to Marenco et al. [2011].

We compared AOD_{ash} with the numerical AOD (hereinafter AOD_{FALL3D}) computed by FALL3D for the Fine Enriched TGSD. Figure IV.8a shows we extended the domain including the southern Europe with a 10-km grid resolution. The time-series of AOD_{FALL3D} shows a spreading over Albania, Greece, Macedonia, Serbia, Turkey, Bulgaria, Romania, Moldova, Ukraine up to the Black Sea and the Russian borders (see Animation IV.A3 in the Supplement).

The comparative study (Figure IV.8b) indicates that AOD_{FALL3D} reproduces two orders of magnitude smaller than AOD_{ash} (i.e. 4.3×10^{-4}). Such a discrepancy is likely attributed mostly to the spatial-temporal shift of the meteorological fields due to the coarse resolution of the raw database [Dacre et al., 2011; Folch et al., 2012] used for the simulation [e.g. Poret et al., 2017]. In fact, comparing with AOD_{FALL3D} computed two grid-nodes northwards (~150 km from the station), AOD_{FALL3D} improved substantially being similar to the AOD_{ash} with ~0.02 (Figure IV.8a). It is worth noting that AOD_{FALL3D} is obtained with $PM_{10} = 0.4$ wt% for the Fine Enriched TGSD, which is selected on the basis of the total AAM analysis. However, considering $PM_{10} = 1.3$ wt% (Section PM_{10} validation), AOD_{ash} became 8.6×10^{-4} and ~0.10 over the Çamlıbel and the two grid-nodes shifted sites, respectively. Although this comparative study has a large uncertainty for both AOD estimations and spatio-temporal delay of meteorological model, we bear in mind that we used AOD observations for simulation results validation only, without constraining the model inputs. Besides these limitations, we note the Fine Enriched TGSD seems able to capture the concentration of ultra-fine ash up to very distal areas (~1700 km from the source).

Discussion

This study proposes integrating field and satellite data of the 23rd February 2013 Etna eruption to constrain the numerical reconstruction of the tephra loading and airborne ash mass. However, the input parameter interdependency implies the non-uniqueness solution through diverse ESP combinations [Connor and Connor, 2005; Scollo et al., 2008; Bonasia et al., 2010; Anderson and Segall, 2013]. Although all the simulations capture reasonably the main features associated with the tephra loading, the Field, bi-Gaussian, and bi-Weibull TGSDs fail to best-fit simultaneously field and satellite data. In particular, only the Fine Enriched TGSD succeeds in reproducing both the tephra loading and airborne ash mass. This argues the need for developing an integrated method for assessing the initial grain-size distribution covering the entire size spectrum.

Considering GSD at the sampled sites, we compared each measurement with the numerical one (Figure IV.3) for the Fine Enriched TGSD. Overall, FALL3D captures 7 of the 10 GSDs by peaking at the same modes. However, 2 of the 3 most proximal samples (i.e. Casetta and Bivio 007 in Figure IV.3) are shifted by 1 Φ, which indicates coarser tephra deposits than the computed ones. In contrast, the Castiglione site (Figure IV.3) shows a finer field deposit than the computed one. These discrepancies can be attributed to the sample positions from the main plume axis, but also the sampling distance from the source [Spanu et al., 2016]. In fact, the coarser material (-4 ≥ Φ ≥ -2) deposits within a narrow area from the vent highlighting the difficulty to correctly capture the coarse tail distribution through the Voronoi tessellation method when the deposit is not adequately sampled [Andronico et al., 2014a].

Regarding the comparative study of the tephra loadings (Figure IV.5), the proximal measurements range from 32 to 1.2 kg/m^2, whereas the computed are between 11 to 4.5 kg/m^2. These results are assumed acceptable as they are within the same order of magnitude [e.g., Scollo et al., 2008; Folch et al., 2010; Costa et al., 2014]. Although the tephra loadings are not perfectly reproduced, the resulting values indicate a consistency with the field measurements by lying within the 1/5-5 times limits for 5 of the 7 proximal samples, whereas the 2 others are within the 1/10-10 times limits. The difference between the computed and measured proximal tephra loadings can be partially attributed, among others, to the low meteorological resolution. Indeed, for simulating several hundred kilometres domain, we used a 4×4 km meteorological resolution (Figure IV.S1 in the Supplement), which means only 5 grid nodes are representing the proximal samples (located between ~5 and ~16 km from the source).

Satellite retrievals were integrated into field data by inverting the PM_{10} fraction to use within the input TGSD. However, focusing on reproducing the AAM per unit area suggests a PM_{10} content of 0.4 wt%, whereas capturing the local maxima requires a larger fraction (~1.3 wt%). As most of Eulerian models, FALL3D has a numerical diffusion effect, which can partially explain the PM_{10} fraction discrepancy [Folch, 2012; Folch et al., 2012]. Meanwhile, satellite retrievals have well-known ash discrimination issues associated with the BTD method. Indeed, spectral features in the TIR may not allow a perfect discrimination of ash (see Guéhenneux et al. [2015] for a review). Additionally, atmospheric effects, such as convective clouds [Potts and Ebert, 1996], or mineral dust [Watkin, 2003] may produce negative BTD leading to false ash pixels detection. In contrast, moisture rich environment confounds BTD retrievals by adding a positive component [Pavolonis et al., 2006]. These biases can affect the determination of the area containing airborne ash over-estimating its extension.

Other complications can be attributed to the effect of ash aggregation, although for explosive basaltic eruptions (e.g. those ones from Etna) should not be significant [Rose and Durant, 2009]. Indeed, the best simulations accounting for ash aggregation under the scheme developed in Costa et al. [2010] returns a contribution of only ~2 wt% over the fine ash. Such results are obtained for an effective aggregate diameter Φ_{Agg} of 2 and a density of 1000 kg/m^3. As expected, ash aggregation appears negligible compared to the TEM.

The use of the Fine Enriched TGSD permitted capturing the observed tephra loading and airborne ash mass, providing a more realistic estimation of the initial magma fragmentation down to the very fine ash distribution compared to the field-derived TGSD. However, such a characterization still needs further work in terms of 1) parameterization of the partial GSD for satellite retrievals, or 2) integration of field and remote-sensing tephra measurements, also for other eruptions benefiting from large dataset. At this stage, we opted for a purely empirical approach but a more theoretical study is the object of ongoing research. It is worth noting that the used inversion of the very fine ash distribution is done comparing with satellite retrievals, which assume a lognormal distribution. This comparison can introduce a bias in the results

without considering for the satellite-derived GSD. However, this study aims at dealing specifically with the reconstruction of the ESP leading to simultaneously capturing the tephra loading and airborne ash dispersal using information relative to coarse and very fine tephra. Also, the results we reported aim at encouraging future work that integrates data from field, ground-based instruments (e.g. visible and infrared images, weather and Doppler radars, light detection and ranging systems – LiDAR, and AERONET network), and satellite sensors (e.g. SEVIRI) to converge towards a full reconstruction of the tephra dispersal and deposition.

The findings of this study have implications for volcanic hazards and the evaluation of the related impacts. In fact, assessing accurately the initial magma fragmentation contributes to a more realistic description of both tephra deposition and airborne ash dispersal. On one hand, the tephra can affect the populations in the vicinity of the volcano (e.g. fallout and tephra accumulation hazards; Andronico et al. [2015]). On the other hand, fine ash has high impact both near the source with the effects of PM_{10} on public health [Horwell et al., 2007; 2013; 2017; Andronico and Del Carlo, 2016; Tomašek et al., 2016), and far away from the volcano with threat on air traffic [Casadevall, 1994; Casadevall et al, 1999; Guffanti et al., 2005]. Quantifying airborne ash (i.e. PM_{10}) released during the 23rd February 2013 lava fountain, PM_{10} dispersed in the atmosphere remaining above 2 g/m^2 for 6 hours after the paroxysm up to several hundreds of kilometres from the source (see Section PM_{10} validation and Figures IV.7 and IV.S2). Such a situation may pose hazards to air traffic safety highlighting again the necessity for assessing accurately the TGSD. As example, on December 2015, the Voragine crater of Etna produced four intense lava fountains within three days [Vulpiani et al., 2016; Corsaro et al., 2017; Pompilio et al., 2017]. These similar episodes had sustained columns (i.e. high MERs) up to 15 km a.s.l. producing significant fine ash dispersed to distal regions. Although fine ash fraction during basaltic explosive eruptions represents a small fraction of the TEM, neglecting it within the TGSD can lead to a substantial under-estimation of the far-travelling airborne ash mass, with implications for aviation safety. We showed that a better PM_{10} characterization is possible by adopting an integrated approach, which use models and all the available observations. We also encourage developing similar integrated approaches to other volcanoes for real time forecast of tephra dispersal.

Concluding remarks

On 23rd February 2013, Etna volcano, Sicily produced an intense lava fountain under strong north-easterly wind direction. The erupted tephra was deposited downwind from the volcano to the Puglia region, located ~410 km from the source. These untypical meteorological conditions gave a rare opportunity to collect field samples from proximal to distal locations. This study aims at numerically reconstructing tephra loading and airborne ash mass by means of field, satellite (SEVIRI), and ground-based (AERONET) retrievals. Among the input eruption source parameters required by FALL3D, a better estimation of the TGSD accounting for both field and satellite measurements was demonstrated and evaluated. In fact, the long residence time of very

fine ash into the atmosphere prevents deposition at reasonable distances. To better characterize the very fines, we parameterized the field-based TGSD through a bi-lognormal and bi-Weibull distribution. None of the two latter TGSDs can provide a very fine ash fraction allowing the computation of any far-travelling airborne ash up to distal areas. For this reason, we suggested here the empirical modification of the field-based TGSD to include the very fine ash by assuming a power-law decay of the tail of the distribution. The Fine Enriched TGSD is similar to other Etna eruptions with a more marked bi-modal distribution peaking at -3 Φ and 0.5 Φ for the coarse- and fine-grained sub-populations, respectively. Eruption source parameters are inverted by means of a goodness-of-fit method best-reproducing simultaneously the tephra loading measurements and airborne ash mass retrieved by satellite. Results indicate a column height of 8.7 km a.s.l., a TEM of ~4.9×10^9 kg, a MER of ~1.3×10^6 kg/s for a paroxysmal phase of 1 hour and 6 minutes, a PM_{10} fraction of ~0.4-1.3 wt% with respect to the TEM, and an aggregate fraction of ~2 wt% of the fine ash. These encouraging results highlight the need for integrating further airborne/airspace multi-sensors with field measurements to better characterize the parameters controlling plume transport in the atmosphere and tephra sedimentation, with emphasis on the very fine ash distribution (PM_{10}) responsible for public health and air traffic safety issues.

Supplement

The figures and animations aim at supporting the numerical reconstruction of the tephra transport and deposition together with the airborne ash dispersal associated with the 23rd February 2013 paroxysm of Etna, Italy. The following information are obtained by using the FALL3D dispersal model with the input Fine Enriched TGSD, which emerges from integrating field and satellite data. The supplement files are available through the following link:

https://drive.google.com/open?id=1qYBPwBvk9EMRrle_I5Lc6PdXberJ1z3C

Figure IV.S1: Figure IV.S1 shows the internal grid mesh (black points) used for simulating the tephra loading and airborne ash dispersal with FALL3D. To be consistent with satellite data resolution (3×3 km at nadir), we used a 4×4 km grid for each altitude level from 0 to 10 km a.s.l., with a 0.5 km step.

Figure IV.S2: Figure IV.S2 compares the satellite retrievals, in terms of airborne ash dispersal, with the corresponding FALL3D results. The squares refer to the distal sampled sites reported in Figure IV.1. These results are obtained imposing a semi-qualitative agreement (i.e. same order of magnitude) between computed and observed local maxima of airborne ash mass (AAM) per unit area. As input, this needs 1.3 wt% of PM_{10} (i.e. $\gamma = 0.70$) within the Fine Enriched TGSD. However, as described in the main text, such a TGSD over-estimates significantly the total AAM compared with a PM_{10} fraction of 0.4 wt% (i.e. AAM optimized; details in Sections ESP estimation and PM_{10} validation).

Animation IV.A1: Animation IV.A1 refers to the time-series of the whole tephra loading (in kg/m^2) computed with the Fine Enriched TGSD (see Section Tephra loading validation). The animation shows the downwind dynamic evolution of the tephra deposit from the 23rd February 2013 at 18:00 to 01:30 the following day.

Animation IV.A2: Animation IV.A2 shows the time-series of the airborne ash mass (i.e. PM_{10}) from 18:00 – 22:00 the 23rd February 2013 (see Section PM_{10} validation). The animation displays how the simulated PM_{10} relative to the Fine Enriched TGSD disperses from the source towards the Calabrian coasts. The colour scale remains the same as the one used for the comparative study between the satellite and numerical results (i.e. Figures IV.7 and IV.S2).

Animation IV.A3: Animation IV.A3 indicates the behaviour of the ultra-fine ash (~1 μm) within the distribution (see Section AOD validation) towards the very distal area from Etna (~1700 km). The animation refers to the time-series of the numerical AOD estimated from the 23rd February 2013 at 18:15 to 22:15 the following day.

Acknowledgements

Chapter V – Etna paroxysmal episode of the 23rd November 2013

Reconstructing volcanic plume evolution integrating satellite and ground-based data: Application to the 23rd November 2013 Etna eruption

Matthieu Poret[1, 2], Stefano Corradini[3], Luca Merucci[3], Antonio Costa[1], Daniele Andronico[4], Mario Montopoli[5], Gianfranco Vulpiani[6], Valentin Freret-Lorgeril[7]

[1] Istituto Nazionale di Geofisica e Vulcanologia, Bologna, Italy

[2] University of Bologna, Geophysics department, Bologna, Italy

[3] Istituto Nazionale di Geofisica e Vulcanologia, CNT, Roma, Italy

[4] Istituto Nazionale di Geofisica e Vulcanologia, OsservatorioEtneo, Catania, Italy

[5] Institute of Atmospheric Sciences and Climate, National Research Council of Italy, Roma, Italy

[6] Department of Civil Protection, Presidency of the Councils of Ministers, Roma, Italy

[7] Université Clermont Auvergne, CNRS, IRD, OPGC, Laboratoire Magmas et Volcans, F-63000 Clermont-Ferrand, France

Correspondence to: Matthieu Poret (matthieu.poret@gmail.com)

Abstract

Recent explosive volcanic eruptions recorded worldwide (e.g. Hekla in 2000, Eyjafjallajökull in 2010, and Cordón-Caulle in 2011) demonstrated the necessity of a better assessment of the ESP (e.g. column height, MER, eruption duration, and TGSD to reduce the uncertainties associated with the far-travelling airborne ash mass. Volcanological studies started to integrate observations to use more realistic numerical inputs, crucial for taking robust volcanic risk mitigation actions. On 23rd November 2013, Etna volcano (Italy) erupted producing a 10-km height plume, from which two volcanic clouds were observed at different altitudes from satellite (SEVIRI, MODIS). One was retrieved as mainly composed by very fine ash (i.e. PM_{20}), whereas the second one as made of ice/SO_2 droplets (i.e. not measurable in terms of ash mass). Atypical north-easterly wind direction transported the tephra from Etna towards the Calabria and Puglia regions (southern Italy), permitting tephra sampling in proximal (i.e. ~5-25 km from source), and medial areas (i.e. Calabria region, ~160km). A primary TGSD was derived from the field measurement analysis, but the paucity of data (especially related to the fine ash fraction) prevented it from being entirely representative of the initial magma fragmentation. For better constraining the TGSD assessment, we also estimated the distribution from the X-band weather radar data. We integrated the field and radar-derived TGSDs by inverting the relative weighting averages to best-fit the tephra loading measurements. The resulting TGSD is used as input for the FALL3D tephra dispersal model to reconstruct the whole tephra loading. Furthermore, we empirically modified the integrated TGSD by enriching the PM_{20} classes until

the numerical results were able to reproduce the airborne ash mass retrieved from satellite data. The resulting TGSD is inverted best-fitting the field, ground-based, and satellite-based measurements. The results indicate a total erupted mass of 1.2×10^9 kg, being similar to the field-derived value of 1.3×10^9 kg, and an initial PM_{20} fraction between 3.6 and 9.0 wt%, constituting the tail of the TGSD.

Keywords: TGSD; FALL3D; SEVIRI; PM_{20}; tephra dispersal modelling; eruption source parameters

Introduction

Volcanic explosive eruptions pose hazards related to the release of large quantity of material into the atmosphere. The observation of the eruption features, such as the eruptive column, the tephra loading, or the far-travelling volcanic plume aims at characterizing the ESP. Hazard assessment related to tephra dispersal, and its implications for aviation safety and public health, is one of the major motivations for developing robust automated tools to forecast tephra loading and airborne ash dispersal [e.g. Costa et al., 2006; Barsotti et al., 2008; Folch et al., 2008; 2009]. To mitigate the risk to aviation traffic, nine VAACs were created worldwide for volcanic cloud monitoring purposes. By making use of operational VATD models, VAACs aim at alerting for the presence of volcanic ash in the atmosphere. Beside other ESPs (e.g. eruption start and duration, column height, and MER), such models require the TGSD as input [e.g. Folch, 2012], being one of the most critical ESPs, significantly affecting tephra dispersal model outputs [e.g. Scollo et al., 2008; Beckett et al., 2015]. Typically, the TGSD is derived from the field sample analysis through the Voronoi tessellation method [Bonadonna and Houghton, 2005]. However, collecting field data on tephra deposit highly depends on the atmospheric conditions, land/sea deposition, site accessibility, etc. As a consequence, for inadequate sample dataset in terms of sampling distance from the source [Andronico et al., 2014a; Costa et al., 2016a], spatial distribution and density of samples [Bonadonna et al., 2015c, Spanu et al., 2016], the field-derived TGSD is uncertain and cannot be assumed as representative of the whole tephra loading and dispersal. Additionally, the atmospheric residence time of the very fine ash (i.e. hereinafter in this work PM_{20}), ranging from hours to weeks [Rose and Durant, 2009] prevents from any rapid deposition implying their substantial under-estimation within the TGSD [Bonadonna et al., 2011]. This raises the necessity for integrating field data with measurements from other sensors (e.g. ground-based radar and satellite) capable to retrieve the missing information in terms of airborne ash. Moreover, the recent eruptions (e.g. Hekla in February 2000, Eyjafjallajökull in April 2010, and Cordón-Caulle in June 2011) have shown the impact of the very fine ash on air traffic [e.g. Guffanti et al., 2010; Folch et al., 2012; Sulpizio et al., 2012], but also on public health (e.g. respiratory diseases; Andronico and Del Carlo [2016]; Tomašek et al. [2016]; Horwell et al. [2017]).

The non-existence of a single instrument capable to cover entirely the grain-size spectrum motivated this study in proposing a method based on the synergic use of field, ground-based, and satellite data for better constraining the TGSD, and therefore the numerical simulations (here FALL3D; Costa et al. [2006]; Folch et al. [2009]) to reconstruct the tephra loading and the far-travelling airborne ash dispersal. Actually, excluding a few studies [Bonadonna et al., 2011; Folch et al., 2012], simulations are commonly run by using the field-based TGSD or adopting subjective parameterizations (e.g. assuming a constant mass fraction for fine ash). Here, we expanded the reconstruction of the tail of the field-derived TGSD by using radar and satellite retrievals.

We applied this methodology to the 23rd November 2013 Etna paroxysm, which occurred from the NSEC, being the most active crater in the last 20 years [Behncke et al., 2014; De Beni et al., 2015]. Atypical winds dispersed the plume north-easterly driving the tephra towards the Calabria and Puglia regions (~400 km from the source), where ash fallout was reported [Bonaccorso et al., 2014; Andronico et al., 2015; Montopoli, 2016]. Few hours after the eruption, tephra was sampled along the plume axis from Etna (i.e. 5-25 km from NSEC) to Calabria (i.e. ~160 km; Figure V.1 and Table V.1). Meanwhile, the eruption benefited from being observed through ground-based (i.e. X-band weather radar and VOLDORAD 2B) and satellite-based (i.e. SEVIRI) remote sensing instruments. Although they operate in different parts of the electromagnetic spectrum, their integration aims at providing a more complete view of the eruption, especially of the plume dynamic.

Next Section presents the 23rd November 2013 Etna eruption, the field and remote sensing data. Then, the TGSD estimation, the modelling approach and methodology used to reproduce the eruption features. Finally, the Sections report the results together with their discussions prior the main concluding remarks.
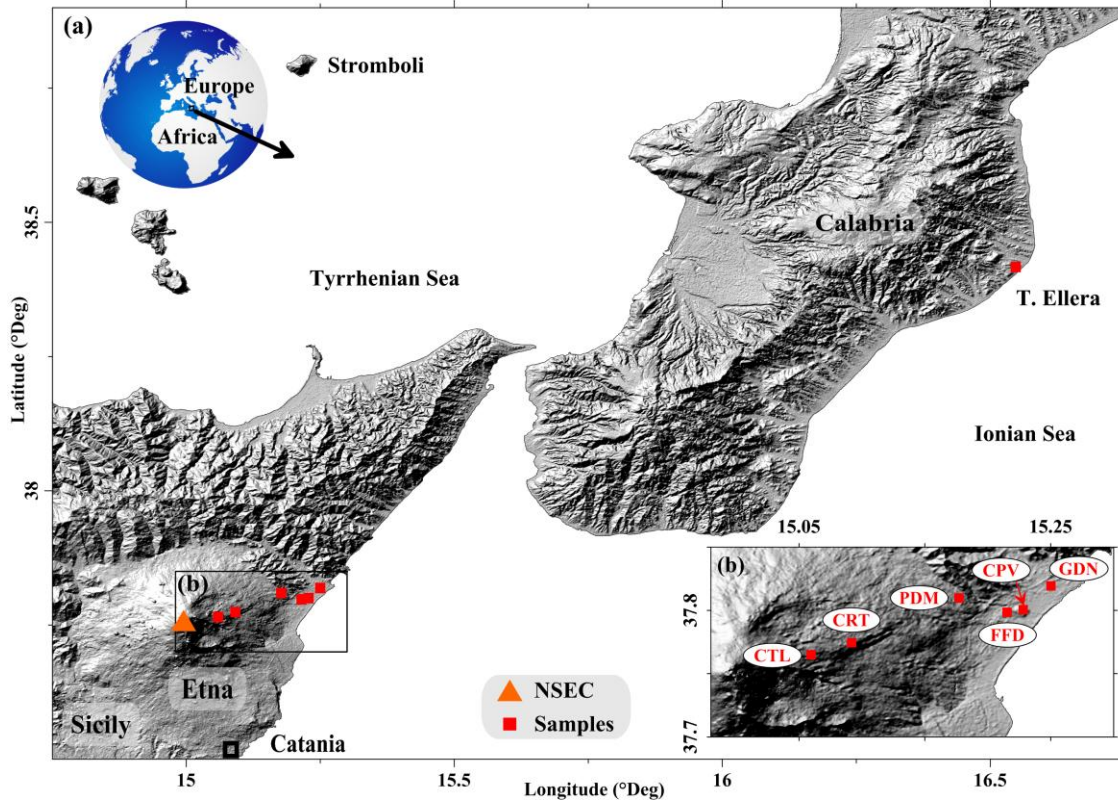
Figure V.1: Tephra sample locations (Sicily and Calabria regions, Italy). a) shows the local to medial areas (up to ~160 km from NSEC) affected by the fallout. b) is a zoom indicating the proximal zone (up to ~25 km from NSEC) and the dispersion of the samples. Details in Table V.1.

	Field observations					Computed loading (kg/m²)			
Sample	**Location**	**Longitude**	**Latitude**	**Mode (Φ)**	**Loading (kg/m²)**	**Field TGSD**	**Radar TGSD**	**Integrated TGSD**	**Whole TGSD**
CTL	**Citelli**	**15.060**	**37.765**	**-3**	1.7×10^1	7.2×10^0	3.4×10^{-1}	4.1×10^0	2.0×10^0
CRT	**Cerrita**	**15.092**	**37.774**	**-2**	1.4×10^1	5.2×10^0	3.5×10^{-1}	2.8×10^0	2.0×10^0
PDM	**Piedimonte**	**15.177**	**37.810**	**-2**	6.1×10^0	1.3×10^1	1.3×10^{-1}	6.6×10^0	1.8×10^0
FFD	**Fiumefreddo**	**15.215**	**37.799**	**-1**	1.6×10^0	9.6×10^0	2.9×10^{-1}	4.9×10^0	1.5×10^0
CPV	**Campovolo**	**15.228**	**37.801**	**-2**	9.5×10^{-1}	8.6×10^0	3.2×10^{-1}	4.4×10^0	1.4×10^0
GDN	**Giardini**	**15.250**	**37.819**	**-1**	4.0×10^0	9.8×10^0	3.8×10^{-1}	5.0×10^0	1.4×10^0
TER	**T.Ellera**	**16.548**	**38.417**	**3**	1.6×10^{-2}	4.0×10^{-4}	3.5×10^{-1}	1.5×10^{-2}	2.4×10^{-2}

Table V.1: Field measurements (locations, loadings, and modes) with the computed tephra loadings obtained with the ARPAE database for the explored TGSDs (Figure V.5).

The 23rd November 2013 Etna lava fountain

In 2013, the 17th lava fountain episode took place on 23rd November from the NSEC [De Beni et al., 2015]. Mild Strombolian explosions initiated on 22nd November afternoon and increased after 07:00 of the following day. The transition between Strombolian and lava fountaining activity (i.e. between resumption and paroxysmal phase; Alparone et al. [2003]) started at 09:30, producing intense lava fountains which increased rapidly in height and intensity. During the 50 min of duration of the paroxysmal phase, a sustained 10-km height eruptive column was observed [Bonaccorso et al., 2014; Andronico et al., 2015]. Moreover, a peculiar feature was recorded from INGV – OE, showing a greyish volcanic plume that rose above a denser brownish one, from which tephra fallout was visible (Figure V.2). Such observation is attributed to the release of a large amount of water vapour/gas rising higher than tephra [Corradini et al., 2016]. This is relevant for characterizing the far-travelling airborne ash, which becomes more complex with the presence of two distinct volcanic clouds. In this case, volcanic ash in the far-field region was testified by an A319 pilot flying over the Albanian coasts at 13:50 and 10.3 km a.s.l., i.e. FL 339, reporting ash between 10.9-11.5 km a.s.l., i.e. FL 360-380 [Crompton and Husson, 2015].

Figure V.2: Photograph of the eruption showing the formation of the two volcanic clouds rising at different altitudes (greyish above the brownish). Source: Courtesy of Boris Behncke (INGV – OE).

Field data

Samples were collected and tephra loading per unit area measured at 7 locations (Figure V.1 and Table V.1). They were oven-dried at 110 °C for 12 hours and analysed in the sedimentology laboratory at INGV – OE, in Catania (Italy). The individual GSD (available in the Supplement; Figure V.S1) were measured optically at 1 Φ-interval through the CAMSIZER® (Retsch Technology), covering the range from -5 to 5 Φ. Although field measurements are commonly used for determining the TEM by integrating the isomass lines [Bonadonna and Costa, 2012; 2013], the paucity of samples with their wide dispersion (Figure V.1) limits the reliability of the estimation based on field observations only. However, on the basis of the field data analysis, Andronico et al. [2015] estimated a TEM of $1.3 \pm 1.1 \times 10^9$ kg making use of the Weibull distribution method [Bonadonna and Costa, 2012; 2013]. Then, combining the field-derived TEM with the paroxysmal duration (~50 min), they calculated an average MER of $4.5 \pm 3.6 \times 10^5$ kg/s. Furthermore, considering the climax phase only (i.e. from 09:55 to 10:14), the MER reached 10^6 kg/s ejecting more than 80 wt% of the erupted mass [Donnadieu et al., 2017]. It is worth noting that such MER estimations represent average (or peak) value for the entire duration of the paroxysmal phase without considering its time evolution (i.e. the variation of eruption intensity). Indeed, the time-series MER can be assessed from the relationships between MER and the column height [e.g. Mastin et al., 2009; Degruyter et al., 2012; Woodhouse et al., 2013; Folch et al., 2016] and from velocity variations at the vent recorded by VOLDORAD 2B.

Satellite and ground-based remote sensing data

The simultaneous record of the eruption from both satellites and ground-based instruments permits retrieving, on the first hand, the plume spreading and airborne ash mass dispersal (see Animation V.A1 in the Supplement), collected by the SEVIRI on board the geostationary MSG satellite. The MODerate resolution Imaging Spectro-radiometer (MODIS) aboard the NASA-Aqua polar-orbit satellite was also used to describe the eruption features [Corradini et al., 2016]. On the second hand, concerning ground-based instruments, the X-Radar [Montopoli, 2016, Vulpiani et al., 2016] and the visible/thermal cameras [Corradini et al., 2016] provided time-series data of the plume height and the erupted mass.

The available data mentioned above were integrated through a multi-disciplinary approach in Corradini et al. [2016] to improve the volcanic cloud retrievals, the source characterization and to generate new products. In particular, the satellite observations (Figure V.3) showed the formation of the two distinct volcanic clouds described in the section describing the eruption. Although both spread north-eastwards, one reached ~6 km a.s.l., being mainly made of ash (Ash Cloud – AC), and therefore retrieved in terms of airborne ash mass and cloud altitude. The second cloud was higher (~11 km a.s.l.) with enough ice/gas droplets (Ice/gas Cloud – IC) to significantly alter the cloud characteristics, blinding the satellite from any ash mass measurement [Prata and Kerkmann, 2007]. Initially, the clouds were united and split out over

the Calabria region (around 11:00). In a final stage, the AC reached the Puglia region, whereas the IC moved over the Ionian Sea towards Albania (around 14:00). In terms of mass, Figure V.4 shows ash was dominant from the onset of the eruption until 11:30, and then ice replaced ash. In fact, from SEVIRI retrievals, ash was likely released between 10:00 and 12:00 prior the emitted water vapour was transformed into ice (i.e. 11:00 – 12:45). This is also shown in Figure V.4, where ice formation starts later than SO_2 and ash emission. SO_2 was released all along the eruption (i.e. 10:00 – 12:30), although with a lower contribution than ash and ice.
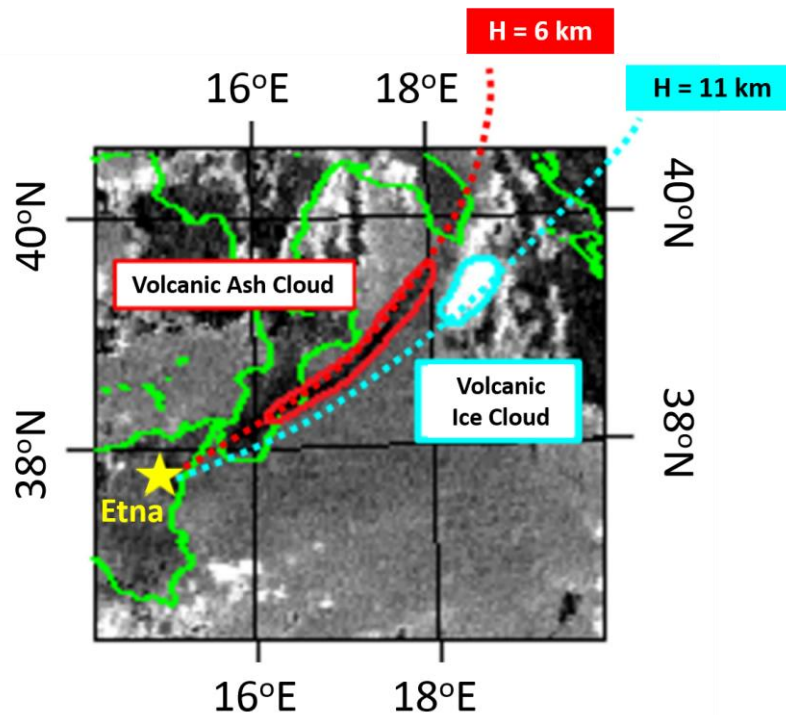
Figure V.3: Satellite image (SEVIRI) showing the trajectories of the two volcanic clouds (modified from Figure 17 in Corradini et al. [2016]). The ash cloud dispersed towards the Puglia region (southern Italy) at ~6 km a.s.l., whereas the ice/gas cloud moved over Albania at ~11 km a.s.l..

The data integration presented in Corradini et al. [2016] permits to reduce the uncertainties associated with the volcanic cloud top height, the ash/ice/SO_2 masses (Figure V.4) and the AOD retrievals. On the basis of the satellite and X-Radar data, Corradini et al. [2016] improved the mass estimation of 30 % and reported an X-Radar-derived TEM of ~3.0×10^9 kg with a PM_{20} fraction between 1-2 wt%, that is ~30-60 tons. The source characterization also can be better described by means of the ESP and the eruptive phases. The plume height time-series was recorded from the visible cameras at INGV – OE, indicating values from the NSEC (~3300 m a.s.l.) to ~11 km a.s.l., with a rapid increase around 9:30 followed by a decay at 10:20.

The VOLDORAD 2B radar is a pulsed Doppler radar operating at 23.5-cm wavelength (L-band) allowing lapilli to block-sized to be detected. VOLDORAD 2B continuously monitors

Etna's summit craters since 2009 [Donnadieu et al., 2015; 2016] at 3 km from the NSEC (La Montagnola Station). Inferred radar parameters (e.g. backscattered echo power) are proportional to the quantity of tephra detected through the radar beam. In addition, the along-beam radial velocities permit lava fountains from being observed at high time resolution (i.e. 0.2 s), inferring near-source detection of the ejection velocities by means of Equation III.1 [Freret-Lorgeril et al., 2016; Donnadieu et al., 2017]. Such approach is relevant for integrating the time-dependent ejection velocities with the corresponding observed eruptive column heights. In particular, we used the VOLDORAD 2B data associated with the 23rd November 2013 eruption to better constrain the eruption phases characterization.
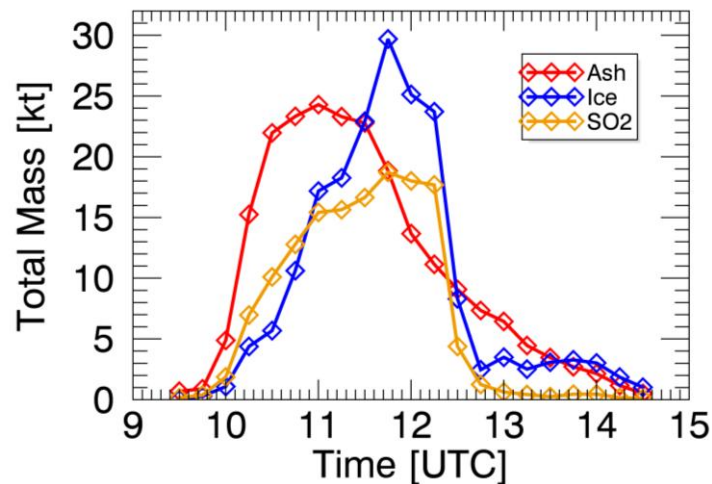
Figure V.4: Ash, Ice and SO$_2$ masses time-series retrieved from SEVIRI for the 23rd November 2013 Etna eruption.

Methodology

Simulating the tephra loading and airborne ash dispersal of the 23rd November 2013 Etna eruption requires to assess the related ESPs, and in particular the TGSD. Their use as input parameters into the FPlume model [Folch et al., 2016] aims at describing the eruption column, representing the source term required by the FALL3D tephra dispersal model [Costa et al., 2016b]. In the following methodology, we present the TGSD reconstruction and modelling approach. Then, the simulations are analysed in terms of tephra loadings and airborne ash mass dispersal to best-fit the field and satellite measurements.

TGSD estimation

The 7 field samples are not sufficient for assuming the field-derived TGSD as the full spectrum TGSD [Andronico et al., 2014a; Beckett et al., 2015; Bonadonna et al., 2015c; Costa et al., 2016a; Spanu et al., 2016]. Although such a field-based TGSD is being biased toward coarse ash, we first estimated the TGSD (hereinafter Field TGSD; Figure V.5) from the individual GSDs using the Voronoi tessellation method [Bonadonna and Houghton, 2005]. However, the

Field TGSD needs to be better characterized prior to be used within atmospheric ash dispersal models. Considering the Field TGSD representativeness on the grain-size spectrum (i.e. -5 to 5 Φ; Section Field data), we used the X-Radar retrievals to constrain the mass relative to coarse and fine ash (i.e. -1 to 5 Φ; Corradini et al. [2016]). The X-Radar-derived TGSD is inverted from the Particle-Size Distribution (PSD), given as ash number density distribution [Corradini et al., 2016]. It is worth noting that we considered a spatial and temporal average of the X-Radar-based PSD for the whole event. The average takes in input each PSD estimated from each single radar resolution volume delineated by horizontal angle, vertical angle, and range distance at each available time step for the airborne ash mass seen by the radar. We converted the PSD into number of particles per unit of volume with the particle-size bins. Then, by means of the volume and density associated with the size bins, we calculated the mass density distribution (hereinafter Radar TGSD; Figure V.5). However, we would like to highlight that retrieval of Radar data is done assuming a Gamma distribution for the number particles per unit of volume for each particle size interval. Then this distribution is converted to express the mass fraction as function of Φ. In particular, since a single gamma distribution is not able to adequately describe large size spectra, a Gamma distribution, with different parameters, is assumed in each particle size range of fine ash, coarse ash, small lapilli, and large lapilli, so the final total distribution is a combination of several gamma distributions. However, such an empirical derived distribution can be approximated using other distributions, such as a lognormal or a Weibull distribution. The latter point will be investigated in future studies.

It is worth noting that the Field and Radar TGSDs are distributions observed through their own grain-size window, which explains the substantial difference in shape (Figure V.5). It follows that assessing accurately the TGSD covering both windows can be done by integrating the Field and Radar TGSDs only. Although, in principle, their integration is possible, the grain-size windows discrepancy prevents from merging the Field and Radar TGSDs without knowing their relative weighting averages. We determined empirically the weight combination by integrating the distributions at regular intervals (i.e. from full Field TGSD to full Radar TGSD). The resulting distribution (i.e. -5 to 5 Φ; hereinafter Integrated TGSD; Figure V.5) is obtained best-fitting the tephra loading at the sampled sites.

However, due to the instrument/method grain-size limit, none of the three TGSDs (Field, Radar, or Integrated TGSD; Figure V.5) contains enough PM_{20} to reproduce the far-travelling airborne ash mass retrieved by satellite. We assessed the tail of the Integrated TGSD (i.e. $\Phi \geq 6$) by modifying empirically the PM_{20} fraction, adding mass into the corresponding classes. We calculated the fractions based on an empirical power-law dependence of the classes with Φ through the following parameterization:

$$X(\Phi_i) = X(\Phi_5) \times \gamma^{(\Phi_i - \Phi_5)}$$

(V.1)

where $X(\Phi_i)$ is the fraction (in wt%) allocated to the ith bin, $X(\Phi_5)$ is the fraction obtained for $\Phi = 5$ and γ is the empirical factor ($\gamma < 1$). The explored γ values span from 0.1-0.7, giving respectively PM_{20} fractions between ~0.6-10.7 wt% of the TEM. The best fraction to use within the TGSD (hereinafter Whole TGSD; Figure V.5) is chosen best-fitting the satellite retrievals.
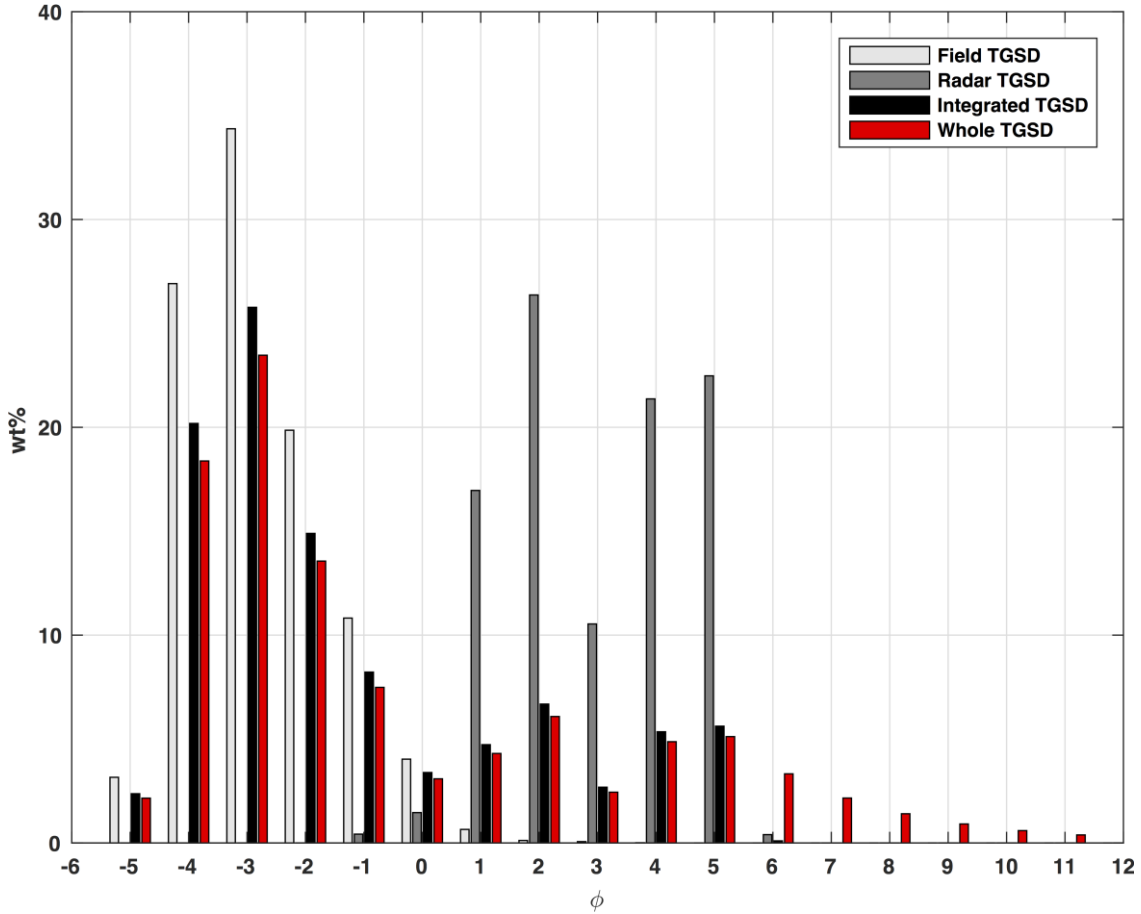
Figure V.5: Input TGSDs estimated from either field or X-Radar data. The Integrated TGSD emerges from a weighting average combination of the Field and Radar TGSDs. The Whole TGSD derives from the Integrated TGSD modified to implement the satellite measurements.

Modelling approach

To furnish the ESPs required by the FALL3D tephra dispersal model, we used the integral plume model FPlume [Folch et al., 2016] describing the eruptive column based on the buoyant plume theory [Morton et al., 1956]. FPlume solves a set of 1D cross-section-averaged equations for mass, momentum, and energy conservation in the eruption column, accounting for wind

coupling, air moisture, particle re-entrainment, and ash aggregation effects [Folch et al., 2016]. Among the source conditions, FPlume feeds into FALL3D by describing the mass flow rate for each particle bin and the vertical distribution within the column. As inputs, FPlume uses the TGSD, initial magma temperature, and water content (Table V.2) to calculate the mass released per unit of time within the column. Indeed, FPlume uses the TGSD to solve the mass conservation equation for each class distributing along the column. Then, the mass for each particle class at each level is transported laterally using FALL3D.

Parameter	Explored Range	
TGSD	Multiple	
Column height	Multiple	
MER	Multiple	
Exit velocity	Multiple	
Initial magma temperature (°K)	1300	
Exit water fraction (wt%)	2.5	
Radial entrainment coefficient (α)	0.05	0.15
Cross-flow entrainment coefficient (β)	0.05	1.00

Table V.2: Input parameters used within the FPlume and FALL3D models. Multiple TGSDs are tested as input for the simulations. The column height, MER, and exit velocity are set as multiple values. The simulation scheme is presented in Figure V.7.

In our case, Etna's magmas have a temperature of 1300 K with ~2.5 wt% of water [Carbone et al., 2015; Spilliaert et al., 2006]. FPlume calculates MER from the column height (or vice versa) for a given wind profile [Folch et al., 2016] by describing the air mixing within the plume through two turbulent air entrainment coefficients (i.e. radial – α and cross-flow – β; Bursik [2001]; Kaminski et al. [2005]; Suzuki and Koyaguchi [2015]; Folch et al. [2016]; Costa et al. [2016b]). Here, α and β are obtained empirically through the solution of an inverse problem best-fitting the erupted mass derived from the field measurements [Poret et al., 2017]. Ash aggregation can be considered negligible during Etna eruptions with less than 2 wt% of the fine ash removed by aggregation. For this reason, we did not consider such process in this study. The effect of the typical uncertainties associated with the input parameters of FPlume on the source term characterization are described in Macedonio et al. [2016].

FALL3D is used for simulating tephra dispersal and is a 3D time-dependent Eulerian model based on the advection-diffusion-sedimentation equation computed over a terrain-following domain [Costa et al., 2006; Folch et al., 2009]. Besides the ESPs, FALL3D needs the time-dependent meteorological fields over the computational domain for the corresponding period (i.e. from 00:00 on 23rd up to 00:00 on 29th November 2013). The first series of simulations are run by means of a local high-resolution meteorological database (ARPAE from INGV – OE) to

better constraining the computed tephra loadings against the field measurements in proximal and medial areas (Figure V.1 and Table V.1). Indeed, ARPAE provides a 7×7-km spatial and 15-minutes temporal resolution over the domain highlighted in Figure V.1. Then, FALL3D internally interpolates the meteorological data over a grid set at 1×1-km resolution. The parameterizations used for the simulations with the ARPAE database are summarized in the Appendix. The related main atmospheric profiles (e.g. temperature, air moisture and wind speed) over the NSEC are displayed in Figure V.6.

The second series of simulations aims at reproducing the satellite retrievals, expanding the computational domain to Albania. The ARPAE data do not cover such a domain, for which we use the meteorological fields from the European Center for Medium-range Weather Forecasts (ECMWF, ERA-Interim-Reanalysis; hereinafter ERA-Interim). They provide 6-hour interval for 37 pressure levels data at 0.75° horizontal resolution. For computational cost reason, the internal grid resolution into FALL3D is set at 5×5 km, which still consistent with the satellite data resolution (3×3 km at nadir). The parameterization used with the ERA-Interim database is summarized in the Appendix.

The consistency between the two databases is checked adding the profiles retrieved over the NSEC with ERA-Interim in Figure V.6. Although ARPAE and ERA-Interim tend to have the same temperature and wind speed patterns, the air moisture from ERA-Interim is slightly lower than ARPAE for 3-6 km a.s.l. and higher for 7-11 km a.s.l.. These observations are not significant to produce a substantial effect on the simulations. Moreover, Figure V.6 also shows the conditions over the Albanian capital (Tirana). With such meteorological conditions, airborne tephra needs 4:30 to be transported from Etna to Albania (Figure V.6), being consistent with the pilot report mentioning ash. Wind speed is moderate to strong, with higher velocities near the volcano than at Tirana city. As indicative values at 9 km a.s.l., we report ~48 and ~45 m/s over the NSEC (at 09:30) for ERA-Interim and ARPAE, respectively, and ~34 m/s over Tirana city at 14:00. Besides the velocities, the wind direction (Figure V.6) shows a strong north-easterly orientation over the NSEC, which is consistent with the tephra dispersion towards Calabria. The profiles indicate a substantial variation between mid- (5-6 km a.s.l.) and high-altitudes (> 7 km a.s.l.), which probably resulted on the different spreading orientations for the two volcanic clouds (AC and IC) at their own altitudes (Figure V.3). Besides the profiles, the consistency for using alternatively the two meteorological databases is checked by constraining the simulations with ERA-Interim to converge the TEM towards the same value as for the Integrated TGSD and the ARPAE database.
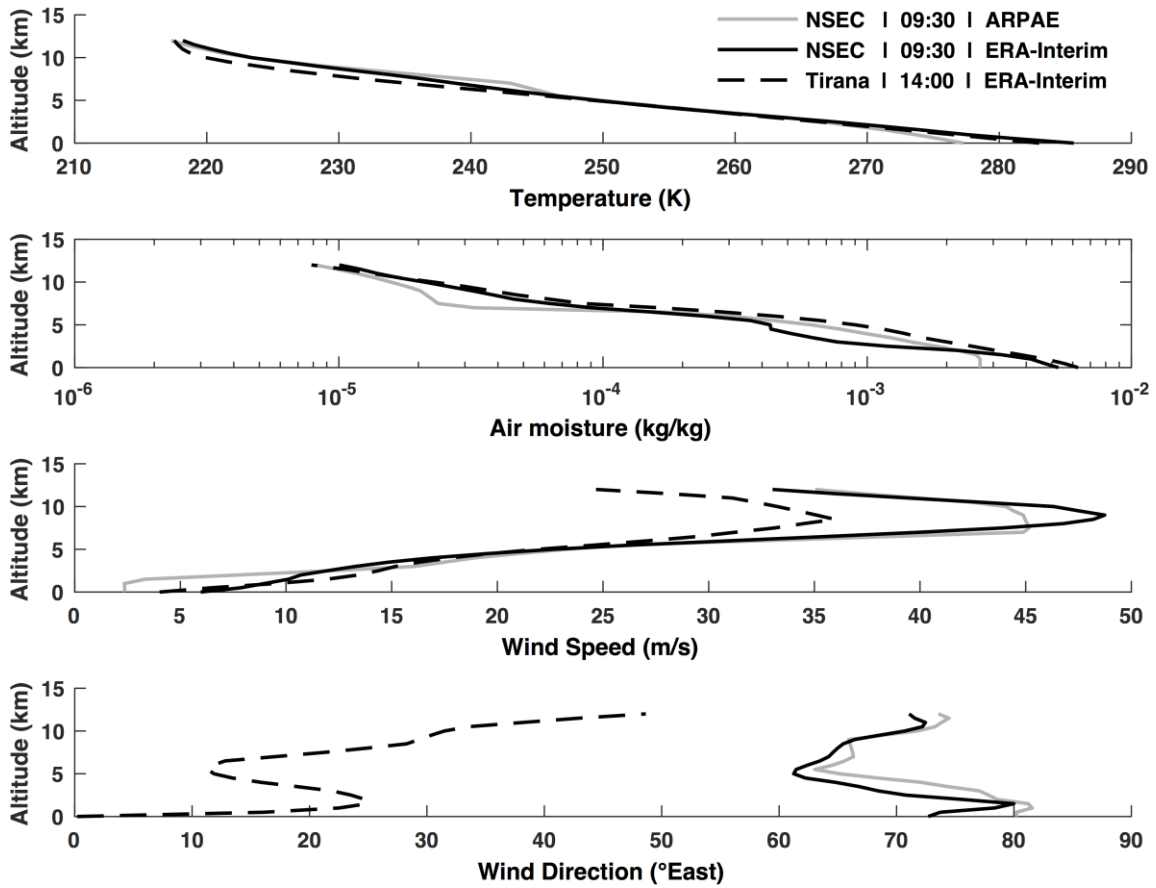
Figure V.6: Main meteorological profiles over NSEC from ARPAE (INGV – OE) and ERA-Interim (ECMWF), and over Tirana city for ERA-Interim.

Tephra dispersal simulations are commonly carried out using the field-based TGSD and assuming a constant average column height (or MER) for the entire duration of the paroxysmal phase (panel a in Figure V.7). However, it is evident that eruption intensity varies substantially with time and consequently the column height [e.g. Scollo et al., 2014; 2015]. To account for such variability, we discretized the eruption into a set of phases in consistency with i) the plume height observations from the remote sensing measurements [Corradini et al., 2016] and ii) the exit velocities retrieved by VOLDORAD-2B [Donnadieu et al., 2015; 2016; 2017]. The improved simulation scheme (panels b and c in Figure V.7) is achieved by coupling this discretization with the ARPAE or ERA-Interim databases and the Integrated TGSD or Whole TGSD, respectively, depending on the inversion purpose.
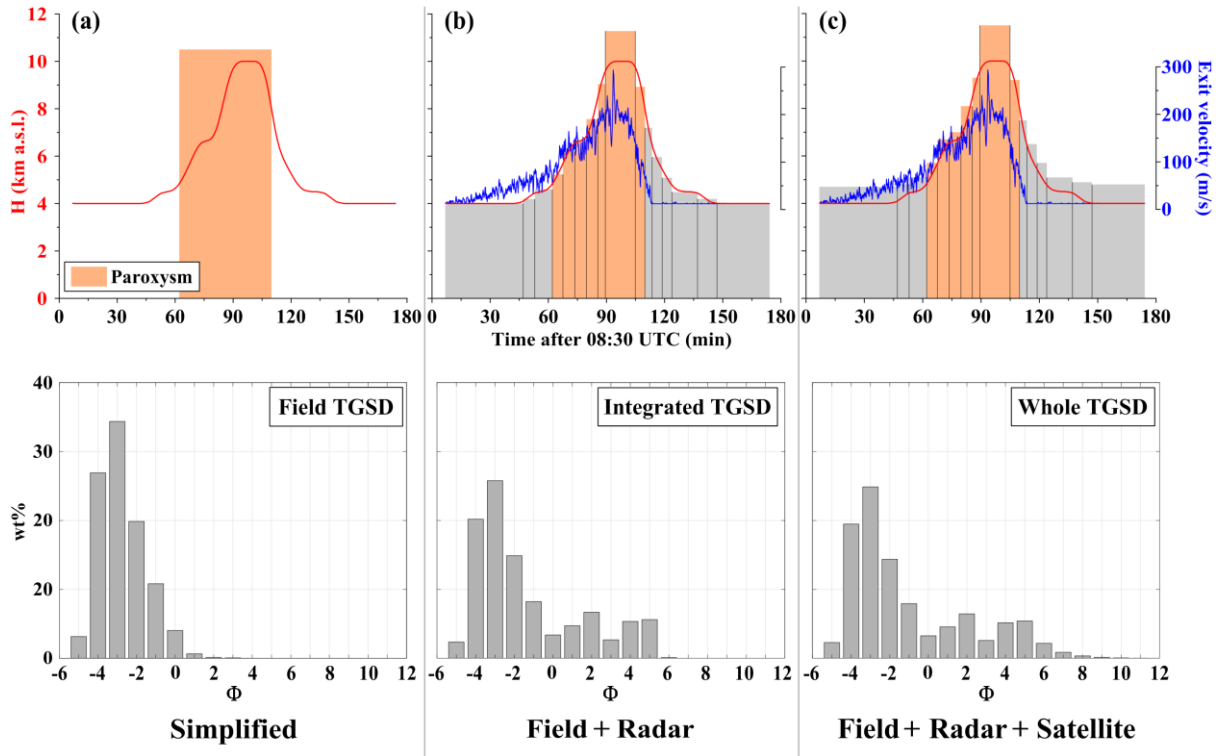
Figure V.7: Simulation schemes. a) Simplified procedure. b) Discretization of the eruption into a set of phases to account for the temporal variation of the intensity (i.e. column height, hence MER, and exit velocity). The improved scheme is accompanied with the Integrated TGSD and ARPAE database. c) Same procedure as b) with the Whole TGSD and ERA-Interim.

Inversion modelling strategy

Simulation optimization is carried out to assess the ESP, and among them the TGSD, leading to the numerical reconstruction of the tephra loading and airborne ash mass dispersal. Input parameters in Table V.2 were varied at constant steps within their ranges facing to the inherent non-uniqueness solution for assessment purposes [e.g. Anderson and Segall, 2013]. Starting by inverting the Integrated TGSD, we tested each weighting average combination of the Field and Radar TGSDs, ranging from 100 wt% Field TGSD to 100 wt% Radar TGSD, with a step of 5 wt%. To select the best combination, we compared the tephra loadings computed at the sampled sites until we best-fit the field measurements.

Considering the simulations, we used the scheme described in the previous section (panels b and c in Figure V.7), which implies a set of column height values (and hence the corresponding MERs) with the average exit velocity. Therefore, neither the column height, the MER, nor the exit velocity were changed in each simulation. However, we inverted the plume parameters (i.e. α and β) from 0.05 to 0.15 and 0.05 to 1.0, respectively [Costa et al., 2016b], by means of the following goodness-of-fit procedure.

The goodness of fit between simulations and field observations was evaluated through different statistical metrics [see Poret et al., 2017]. In particular, we used *RMSE* assuming 3 different error distributions (i.e. *RMSE₁, RMSE₂, and RMSE₃*) described in Folch et al. [2010]. We also used the Aida [1978]'s indexes *K* (i.e. geometric average of the distribution) and *k* (i.e. geometric standard deviation of the distribution).

$$K = exp\left[\frac{1}{N}\sum_i^N \log\left(\frac{Obs_i}{Sim_i}\right)\right]$$

(V.2)

$$k = exp\left[\sqrt{\frac{1}{N}\sum_i^N \log\left(\frac{Obs_i}{Sim_i}\right)^2 - \left(\frac{1}{N}\sum_i^N \log\left(\frac{Obs_i}{Sim_i}\right)\right)^2}\right]$$

(V.3)

where *i* refers to the ith sample over *N*, *Sim* and *Obs* are the simulated and observed tephra loadings, respectively. For a given set of ESPs, *K* gives the gap between the theoretical optimal tephra loading samples and the simulated ones. The reliability of the simulation is obtained for *K* between 0.95 and 1.05, which means a threshold of ±5 wt% from the derived theoretical optimal TEM. It follows that the best simulations are selected for *K* close to 1 with *k* and the 3 *RMSEs* minimized. Additionally, we estimated the *bias*, the *correlation*, and the Student T test (*TTest*) [Folch et al., 2010].

After the Integrated TGSD, the Whole TGSD is inverted by quantitatively analysing the effect of different PM_{20} fractions (i.e. 0.6-10.7 wt%; Section TGSD estimation) on the computed airborne ash dispersal. The best fraction is selected by means of the following 3 statistical metrics. The mass difference (i.e. $\Delta Mass$) between the satellite measurements and the FALL3D estimates. We compared the masses over the number of pixels given by the plume mask (obtained for the threshold of 0.1 t/km^2) retrieved from SEVIRI:

$$\Delta Mass = \frac{1}{\Delta T}\int_{t_0}^{t_f} (M_{Obs} - M_{Sim})\, dt$$

(V.4)

where M_{Obs} and M_{Sim} are the observed and simulated masses integrated over the whole event (i.e. from $t_0 = 09{:}30$ to $t_f = 14{:}30$, with $\Delta T = t_f - t_0$). This index gives the discrepancy (in

tons) for each γ factor (i.e. PM$_{20}$ fractions). Additionally, we also calculated for each γ factor the absolute average difference of mass per unit area ($\overline{Sum(\Delta)}$ in t/km^2) for the entire volcanic cloud by the following:

$$\overline{Sum(\Delta)} = \frac{1}{\Delta T} \int_{t_0}^{t_f} \frac{\sum_N |M_{Obs}(N) - M_{Sim}(N)|}{Area_P} dt$$

(V.5)

where N is the number of pixels (i.e. plume mask), $M_{Obs}(N)$ and $M_{Sim}(N)$ are the observed and modelled masses associated with the Nth pixel for SEVIRI and FALL3D, respectively. $Area_P$ refers to the area covered for the related time interval, which is calculated by means of N and the pixel resolution (i.e. 9 km^2). This index indicates the uncertainty of the simulated airborne ash mass per unit area with respect to the satellite retrieval.

Considering that $\Delta Mass$ and $\overline{Sum(\Delta)}$ are discrepancy estimates, the selection is done on the basis of their minimization. Nonetheless, $\overline{Sum(\Delta)}$ gives absolute values preventing from any over- or under-estimation characterization. It follows that we evaluated also the following index:

$$\varepsilon = \frac{1}{\Delta T} \int_{t_0}^{t_f} \frac{[\sum_N M_{Obs}(N) - M_{Sim}(N) < 0] + [\sum_N M_{Obs}(N) - M_{Sim}(N) > 0]}{Area_P} dt$$

(V.6)

where ε refers to an over-estimation per pixel when $\varepsilon < 0$ and an under-estimation per pixel for $\varepsilon > 0$, with a best-fit for $\varepsilon = 0$. Moreover, the index indicates the average mass difference per unit area (i.e. t/km^2) between the satellite measurements and the simulation. The synergic use of these metrics aims at providing a simple way of comparing spatially and temporally the simulation outputs with the field and remote system measurements.

Results and Discussions

This section describes the results of the inversion of i) the ESPs, and among them, ii) the Integrated TGSD reproducing the tephra loading. Then, iii) we report the results for assessing the PM$_{20}$ fraction needed within the Whole TGSD to capture the airborne ash transported in distal area.

ESP inversion

Regarding the Integrated TGSD inversion (Section Inversion modelling strategy), Table V.3 shows the statistical analysis for the best simulation (i.e. $K \approx 1$, $RMSE_1$, $RMSE_2$, $RMSE_3$, and k minimized) for each weighting average combination. Regardless of the weights, $RMSE_1$ and $RMSE_3$ have flat patterns, motivating we relied on the $RMSE_2$ and k. They show relevant combinations from (65,35; i.e. 65 and 35 in wt% for the Field and Radar TGSDs respectively) to (85,15). Although $RMSE_2$ ranges between 1.56 to 1.85 from (65,35) to (85,15), k is minimized at 2.95 for (75,25), being selected as best weighting average combination for composing the Integrated TGSD (Table V.3 and Figure V.8). It is worth noting that $RMSE_2$ and k indicate relatively high values yielding a mean error factor nearby 3, which is comparable to uncertainties associated with other classical methods [Bonadonna and Costa, 2012; 2013; Bonadonna et al., 2015c].
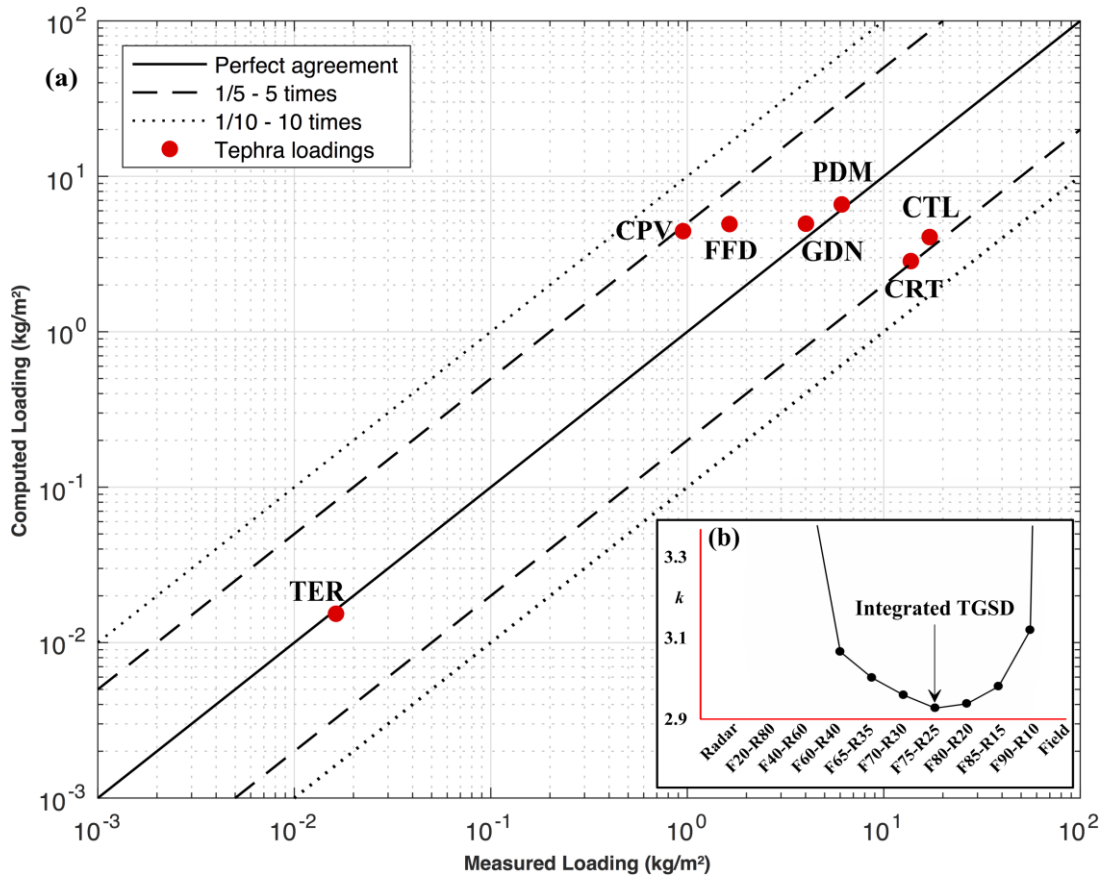
Figure V.8: a) Comparative study between the measured and computed tephra loadings for inverting the Integrated TGSD. b) Graphic of the k index showing the optimization for assessing the best weighting average combination to apply to the Field and Radar TGSDs (details in Table V.2).

| Integrated TGSD	Input			Statistical Metric								Output
Combination (in wt%)	α ($\alpha_1 - \alpha_2$)	β	K	k	$RMSE_1$	$RMSE_2$	$RMSE_3$	Correlation	Bias	TTest	TEM ($\times 10^9$ in kg)
Radar TGSD	0.15 – 0.15	1.00	6.97	9.82	0.97	7.71	0.87	-0.2	-0.3	0.1	5.73
20 Field | 80 Radar	0.06 – 0.09	0.72	1.00	4.35	0.84	2.95	0.74	0.8	0.0	1.0	2.84
40 Field | 60 Radar	0.06 – 0.09	0.40	1.02	3.48	0.81	1.61	0.74	0.8	0.0	1.0	1.66
60 Field | 40 Radar	0.06 – 0.09	0.28	1.01	3.08	0.78	1.53	0.77	0.9	0.0	1.0	1.28
65 Field | 35 Radar	0.06 – 0.09	0.26	1.01	3.02	0.77	1.56	0.77	0.9	0.0	1.0	1.22
70 Field | 30 Radar	0.06 – 0.09	0.25	0.98	2.98	0.77	1.67	0.80	0.9	0.0	1.0	1.21
75 Field | 25 Radar	0.06 – 0.09	0.22	1.02	2.95	0.76	1.64	0.79	0.9	0.0	1.0	1.13
80 Field | 20 Radar	0.06 – 0.09	0.22	0.99	2.96	0.75	1.77	0.82	0.9	0.0	1.0	1.13
85 Field | 15 Radar	0.06 – 0.09	0.21	1.01	3.00	0.75	1.85	0.84	0.9	0.0	1.0	1.10
90 Field | 10 Radar	0.06 – 0.09	0.21	1.00	3.13	0.74	2.02	0.88	0.9	0.0	1.0	1.12
Field TGSD	0.06 – 0.09	0.35	0.99	6.56	0.83	3.65	1.44	0.9	0.0	1.0	1.60

Table V.3: Statistical metric for the best simulations (i.e. α and β) for each weighting average combination for the Integrated TGSD. α is described through α_1 and α_2 within the calculation [Folch et al., 2016]. TEM indicates the associated theoretical value for each combination.

Figure V.9 illustrates the statistical analysis of the Whole TGSD inversion (Section Inversion modelling strategy) for the best simulation for each PM_{20} fraction. Considering the whole airborne ash mass, the results yield a best value for $\Delta Mass$ at $\gamma = 0.65$ (i.e. $PM_{20} = 9.0$ wt%), indicating an overall under-estimation of ~76 tons of ash by FALL3D for the entire eruption. Then, $\overline{Sum(\Delta)}$ shows a minimum for $\gamma = 0.40$ (i.e. $PM_{20} = 3.6$ wt%), giving an absolute average difference of mass per unit area of ~0.37 t/km^2 for the whole sequence. The third index returns a best value of $\varepsilon = -0.03$ t/km^2 for $\gamma = 0.65$ (i.e. $PM_{20} = 9.0$ wt%), being consistent with $\Delta Mass$. ε likely reflects that FALL3D slightly over-estimates the average mass per pixel of 0.03 t/km^2. By integrating the results (Figure V.9), the Whole TGSD required the minimum PM_{20} fraction of 3.6 wt% to best reproduce in absolute the average ash mass per unit area. However, such a fraction is not sufficient for best simulating the whole airborne ash mass released during the eruption, and minimizing the over- or under-estimation, which tends to be satisfied with higher PM_{20} fractions (i.e. 9.0 wt%). The corresponding input TGSD is displayed in Figure V.5. Moreover, $\Delta Mass$ and ε in Figure V.9 both indicate that FALL3D under-estimates substantially the airborne mass for PM_{20} fractions lower than ~7 wt% and over-estimates above ~10 wt%.

Regarding the other ESPs, although the column height values were not changed throughout the simulations (panels b and c in Figure V.7), we report here the MER inverted by FPlume for the climax phase only, with is of ~7.0×10^5 kg/s. The calibration of α and β returns values ranging from 0.06-0.15 and 0.21-1.00, respectively, depending on the weighting average combination

(Table V.3). The latter ranges are consistent with the literature [Devenish et al., 2010; Suzuki and Koyaguchi, 2015].
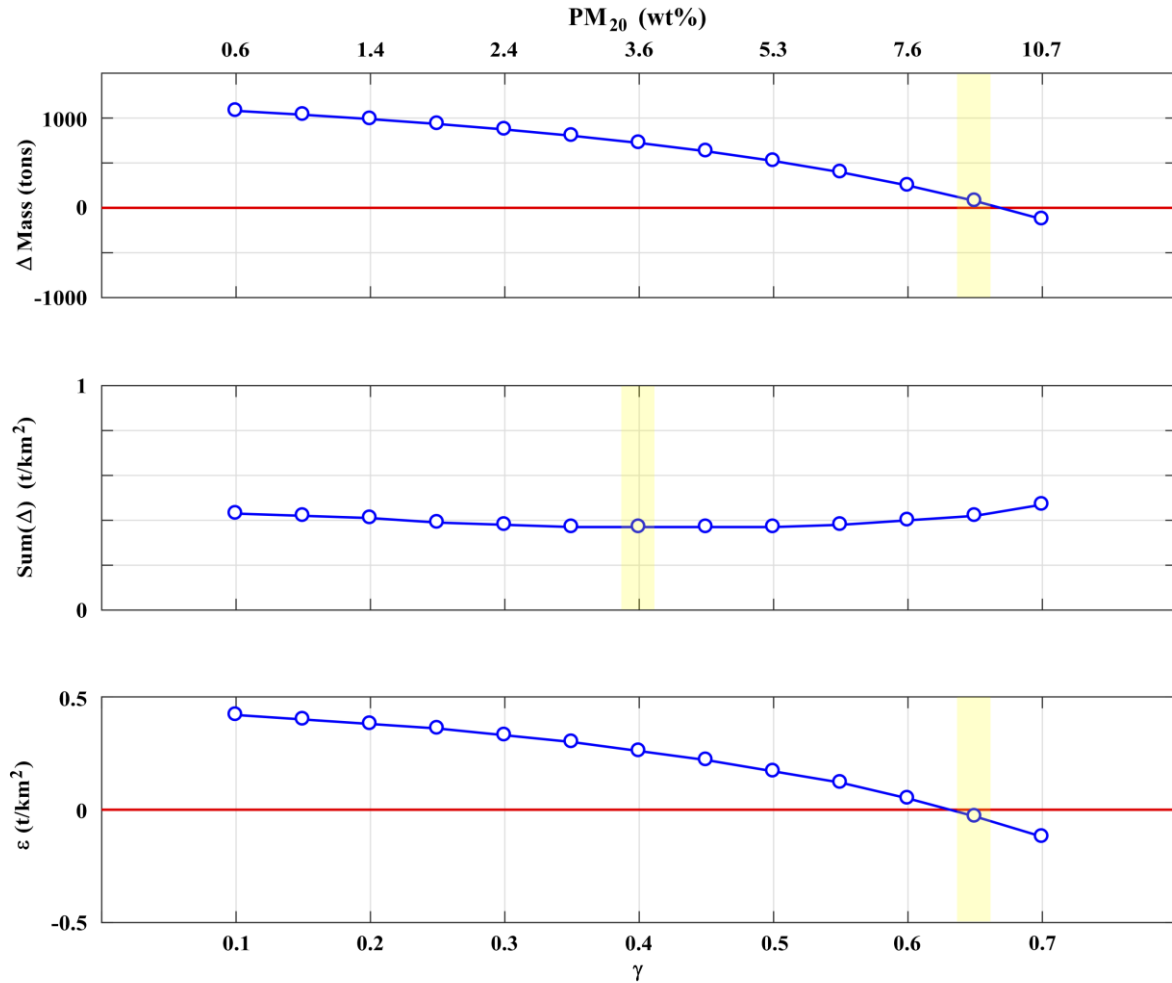
Figure V.9: Quantitative analysis of the airborne ash mass measured from SEVIRI and computed by FALL3D to invert the PM_{20} fraction to use within the Whole TGSD for best-reproducing the SEVIRI retrievals. The upper part compares the whole airborne ash masses for the entire eruption, whereas the middle part gives the difference of the absolute average difference of mass per unit area. The lower part quantifies the difference in terms of mass per unit area.

Tephra loading

During the Integrated TGSD inversion, the 6 proximal samples were relatively stable when varying the weighting average combination, whereas the farthest sample (i.e. TER) was substantially affected. Figure V.8 shows the comparison between the computed and measured tephra loadings with the Integrated TGSD (details in Table V.1). It is worth noting that making use of the Field TGSD prevents FALL3D from capturing the TER sample, while the Radar TGSD fails on most of the samples as indicated in Table V.1. These observations argue the necessity to combining the two different distributions through the Integrated TGSD, especially

when field measurements are few. Figure V.8 shows the 7 samples lying within the 1/5- 5-times threshold of the measured tephra loadings, especially the unique medial sample (i.e. TER). As indicative values from Table V.1, the 6 proximal samples indicate tephra loadings ranging from 1 to 17 kg/m^2. In contrast, FALL3D computed them between 3 and 7 kg/m^2 for the Integrated TGSD. Such narrower range compared to the field data can be attributed to the complexity for modelling in proximal area (< 20 km from the source), and the field samples location with respect to the main plume axis.

Besides the tephra loadings, we also compared the field-derived GSD at the sampled sites with the numerical results for the Integrated TGSD (see Figure V.S1 in the Supplement). Although FALL3D reproduces accurately 3 of the 7 samples by peaking at the same modes, 4 proximal samples (i.e. CRT, PDM, FFD and GDN) are shifted by 1 Φ, indicating the field measurements being slightly finer than the computed ones. This discrepancy argues the difficulty for computing accurately at such proximal areas due to plume dynamic complexities [e.g. Cerminara et al., 2016]. Nonetheless, the mode shift can also be attributed to the sampling distance from the source as explained in Spanu et al. [2016]. Indeed, at proximal area the coarse tephra ($-4 \geq \Phi \geq -2$) is depositing rapidly, increasing the difficulty of estimating accurately this part of the TGSD with the Voronoi tessellation method together with a paucity of field measurements [Andronico et al., 2014a]. Moreover, we cannot exclude partial breakages of few coarse-grained clasts when impacting the ground [Andronico et al., 2015], which also may result on grain-sizes slightly finer than expected.

Although we used the improved simulation scheme (Section Modelling approach; panel b in Figure V.7), we run a simulation through the simplified procedure (panel a in Figure V.7) to highlight the effect on the tephra loading, and therefore the statistical analysis. The results show that making use of a constant plume height (here ~11.3 km a.s.l.) for the entire paroxysmal phase give $K = 1.01$ and $k = 5.76$ with $RMSE_1 = 0.80$, $RMSE_2 = 3.36$, and $RMSE_3 = 1.33$, which are significantly higher than for the improved procedure (details in Table V.3). Regarding the TEM, the simplified scheme returns 1.5×10^9 kg, which is ~34 % higher than for the integrated approach with 1.2×10^9 kg. The latter TEM is in good agreement with the estimation of 1.3×10^9 kg reported in Andronico et al. [2015]. It is worth noting that varying the weighting average from 100 wt% Field TGSD towards 100 wt% Radar TGSD yields an increasing TEM going from 1 to 6×10^9 kg, respectively (Table V.3). This observation on TEM is consistent with the results described in Corradini et al. [2016], which indicates an X-Radar-derived total mass of 3.0×10^9 kg compared to the field-derived TEM of 1.3×10^9 kg from Andronico et al. [2015]. Such a difference between X-Radar and field-based TEM estimates can be explained by considering the following aspects: i) X-Radar samples airborne particles during their fallout whereas the field measurements are based on deposited tephra; ii) the operative window focuses the X-Radar retrievals on detecting the ash particles (-1 to 5 Φ), while the field sampling method expands the measurements to block-sized (-5 to 5 Φ); iii) the Radar TGSD refers to the average

over the duration observed from the radar at the sampled grid points, which not necessarily coincides with the duration and location characterized by the Field TGSD; iv) as explained in Section TGSD estimation, the X-Radar measurements are made with assumptions using a regression model of radar simulations, which can add a further degree of uncertainty. The assumptions mainly affecting the final radar retrieval involve the radar forward model used to set up the radar retrieval scheme. It follows that assumptions made on particle shape, density, orientation, and PSD play the key role. However, the presented integrated approach by weighting the distributions issued from different methods aims at preventing the resulting Integrated TGSD from being associated with the full uncertainty of a single source.

The use of the different distributions (i.e. Field, Radar, Integrated, and Whole TGSDs) presented in this study permits comparing the resulting tephra loading maps (Figure V.10). The tephra loading scale reported in Figure V.10 refers to the use of the ERA-Interim database, indicating slightly different tephra loadings than the values in Table V.1 (ARPAE). Here, Figure V.10 is used as indicative tephra loading maps to display the effect of the input TGSD on the resulting tephra dispersal, showing the affected areas (e.g. Calabria and Puglia regions). In particular, the use of the Field TGSD (panel a) permits FALL3D to compute the tephra loadings at the sampled sites up to Calabria, but not in Puglia region where ash was reported. The Radar TGSD (panel b) operates in the ash window preventing its use from reproducing any tephra loading and airborne ash data. In contrast, the Integrated and Whole TGSDs (panels c and d) capture all the tephra loading samples, but only the Whole TGSD succeed on simulating the far-travelling airborne ash mass retrieved from satellite. The corresponding time-series animation of the tephra loading associated with the Whole TGSD is available in the Supplement (Animation V.A2).
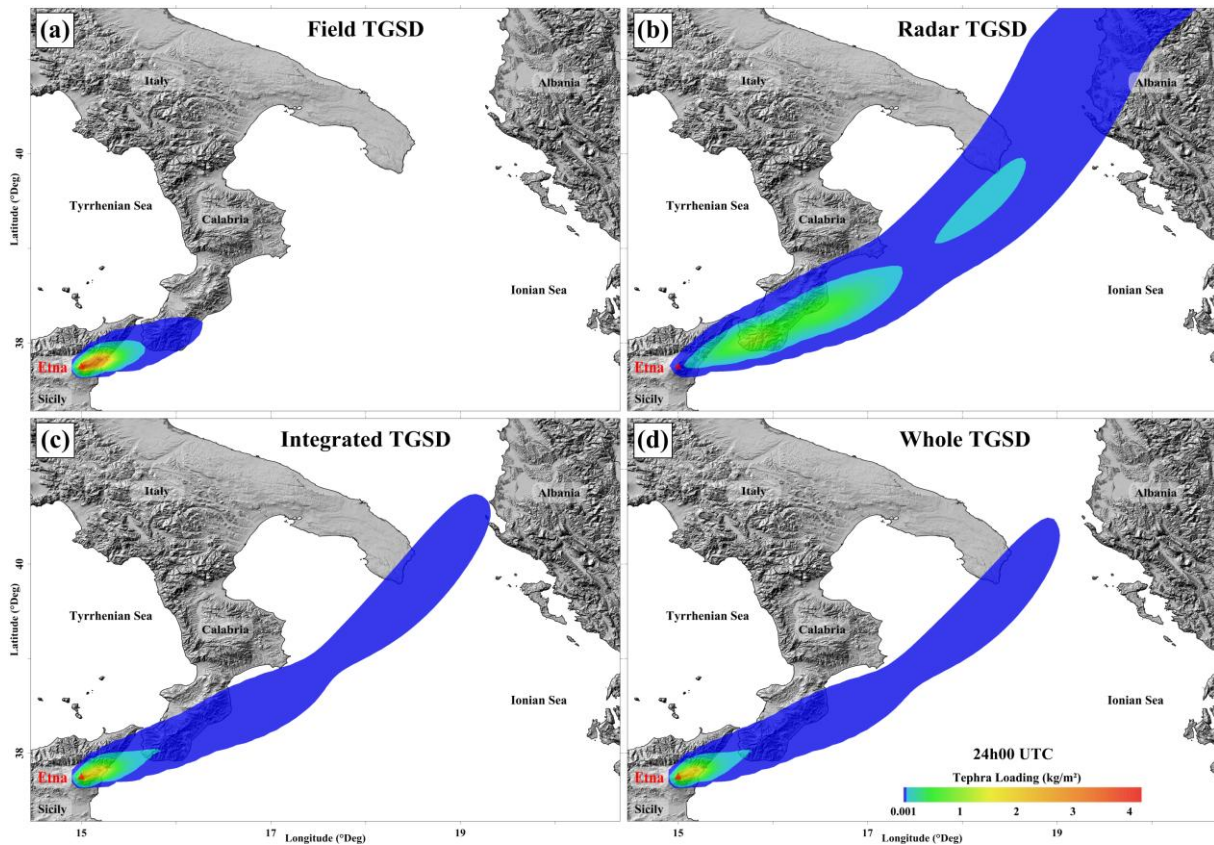
Figure V.10: Tephra loading maps computed with the a) Field, b) Radar, c) Integrated, and d) Whole TGSDs, respectively. They indicate the relevance of the integrated approach reproducing the affected areas.

Airborne ash dispersal

As mentioned in the description of the eruption, large quantities of ash, water vapour (transformed into ice) and SO_2 gas (Figure V.4) were released from Etna, preventing the remote systems from quantifying the whole event easily. The formation of two volcanic clouds (AC and IC) following their own trajectory at different altitudes (Figure V.3) increased substantially the complexity of comparing quantitatively the far-travelling airborne ash masses (i.e. SEVIRI and FALL3D). Indeed, the columnar satellite measurements and FALL3D results prevent from isolating the two clouds, which motivated this study to focus on the plume mask retrieved by SEVIRI for each time (Figure V.11). Figure V.11 illustrates the comparison between the retrieved and computed airborne ash mass. By means of the inverted PM_{20} range (i.e. 3.6-9.0 wt%), we displayed the airborne ash mass maps. The left column refers to the minimum PM_{20} fraction (i.e. 3.6 wt%) required to capture accurately the absolute average difference of mass per unit area (i.e. $\overline{Sum(\Delta)}$), whereas the right column corresponds to the fraction (i.e. 9.0 wt%) best reproducing the whole airborne ash mass (i.e. $\Delta Mass$ and ε). Each panel in Figure V.11 shows the overlapping between the SEVIRI retrievals and the FALL3D outputs for a given

time. Although the overlap tends to decrease with time, the results for $\gamma = 0.65$ (i.e. $PM_{20} = 9.0$ wt%) indicate a better performance than for $\gamma = 0.40$ (i.e. $PM_{20} = 3.6$ wt%). The entire time-series animations are available in the Supplement (Animations V.A3 and V.A4 for $\gamma = 0.40$ and $\gamma = 0.65$, respectively).

The PM_{20} range obtained for the 23rd November 2013 Etna paroxysm tends to be relatively high with respect to the literature (1-2 wt%; Corradini et al. [2016]), eventually attributed to the observational data used and the instrument properties. However, in terms of mass to the TEM, the estimated PM_{20} fractions indicate consistent values. Indeed, 1-2 wt% of the X-Radar TEM (3.0×10^9 kg) refers to 30-60 tons, while 3.6-9.0 wt% of the integrated TEM (1.2×10^9 kg) gives 43-108 tons. In fact, Corradini et al. [2016] integrated X-Radar data with satellite retrievals to assess the PM_{20} fraction. However, the satellite cannot quantify any ash mass from pixels mainly filled by ice or gas (e.g. SO_2). In other words, although the volcanic ice/gas clouds (i.e. IC) are assumed to be produced from ash nucleus [Corradini et al., 2016], the probable presence of ash within such clouds will be missed from SEVIRI.

Being the airborne ash mass spreading downwind towards the far-field, the very fine ash fraction (i.e. here 3.6-9.0 wt% of the erupted mass) is a critical input into operational tephra dispersal models (e.g. HYSPLIT, Stunder et al. [2007]; NAME, Witham et al. [2007]; FALL3D, Folch et al. [2012]), which are widely used for aviation safety. Although few studies have attempted to better constrain the fraction estimation, eruptions from different volcanoes are not comparable as such a fraction is very different from one case to the other, ranging from 50 wt% to few wt% [Rose and Durant, 2009]. As discussed by Costa et al. [2016a; 2017], the very fine ash fraction varies with eruption intensity, magma composition, and eruption style. In particular, at the Spurr 1992's eruption, Wen and Rose [1994] estimated ~2 wt% dispersed into the distal area. At the Eyjafjallajökull 2010's eruption, the estimated range span from ~0.9-11 wt% [Bonadonna et al., 2011; Dacre et al., 2011; Devenish et al., 2012]. However, some operational models assume a fraction of ~5 wt%, which is not related with our estimate for the Etna eruption. In fact, assuming a constant fraction (e.g. 5 wt%) would represent the very fine ash fraction that escapes to aggregation processes and travels in the far field. In the case of basaltic eruptions, like at Etna, the eruption intensity and the very fine ash content are low, and hence aggregation less efficient [Costa et al., 2010], implying that most of the fraction can be transported distally. These observations yield the necessity for better considering such fraction as input, suggesting further investigations on both basaltic and silicic volcanoes.

Regarding the FALL3D results in Figure V.11, the airborne ash maps show the two volcanic clouds (AC and IC) observed from satellite [Corradini et al., 2016], although they are still connected to each other. Dispersing simultaneously from the source, the FALL3D simulations yield the presence of volcanic ash following the trajectory of AC below FL 250. In addition, FALL3D also indicates a major contribution of the airborne mass associated with the IC trajectory spreading over FL 250. The results in terms of temporal dispersal (Animation V.A3)

are corroborated by the SEVIRI retrievals (Animation V.A1) and the pilot report, which mentioned volcanic ash and probably gas near Albania at FL 360-380 [Crompton and Husson, 2015].
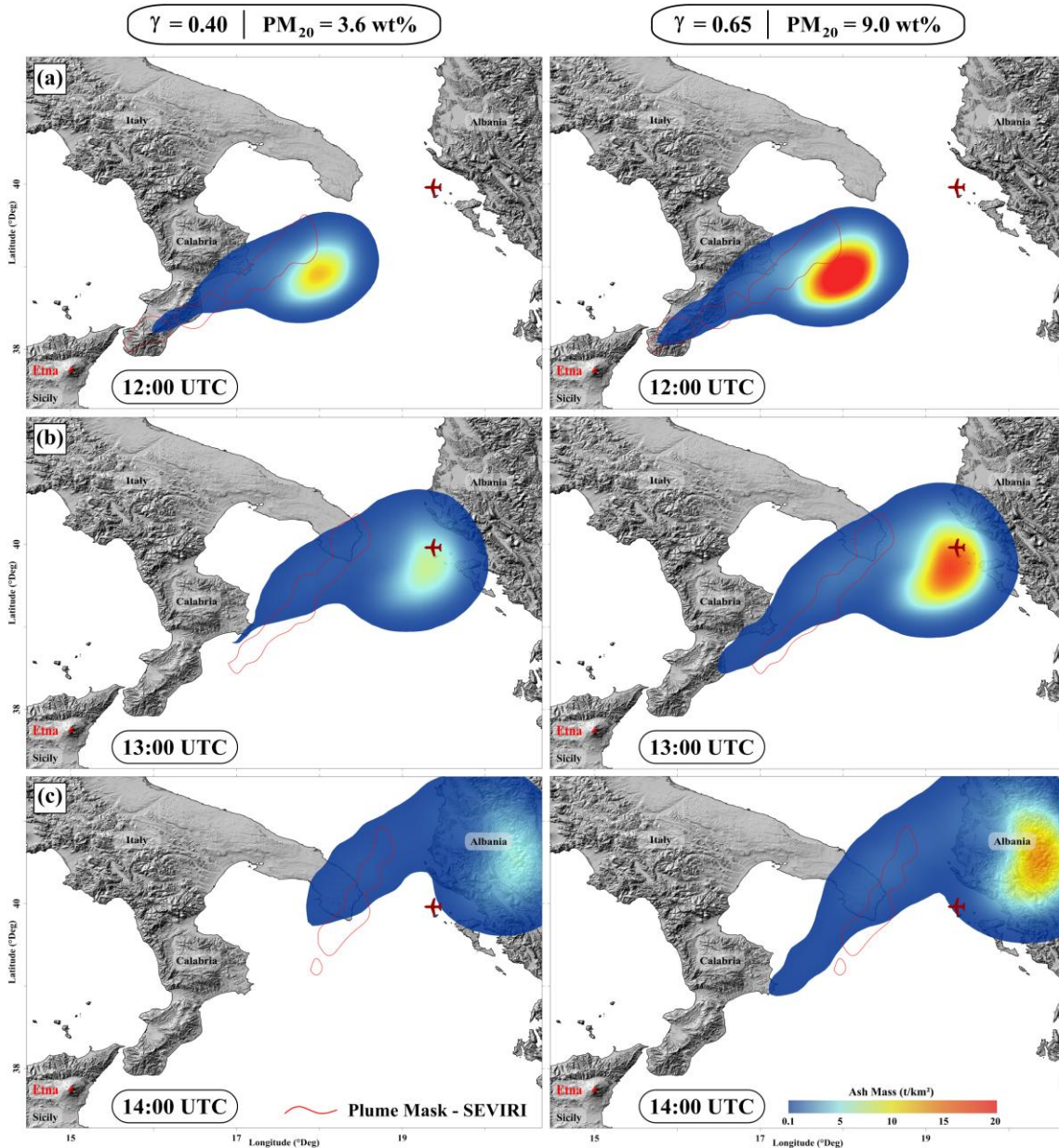
Figure V.11: Illustration of the comparative study between the SEVIRI and FALL3D airborne ash masses for a given time (i.e. 12:00, 13:00, and 14:00) to best-reproduce the satellite retrievals.

As a consequence of being blind to any ash within the IC, the comparative study results represent partially the whole airborne ash. This raises questions related to volcanic hazards, such as the air traffic safety. In fact, on the basis of the FALL3D results, the IC appears to have a significant amount of erupted material (i.e. PM_{20}, ice, and gas). This observation highlights the necessity for quantifying entirely the far-travelling airborne tephra, perhaps benefitting from

other sensors capable to characterize such aerosol clouds. In particular, this study inferred from quantitative analysis based on the observations in terms of tephra loading and airborne ash mass the interest for integrating retrievals from diverse instruments to assess accurately the initial magma fragmentation (i.e. TGSD of the whole erupted tephra).

Conclusions

Recent studies have shown the need for improving the assessment of the eruption source parameters to reduce the uncertainties and present more realistic numerical outputs, which can be used for hazards mitigation. Here, we worked on better estimating the initial magma fragmentation (i.e. TGSD) by integrating measurements from field samples, ground-based (X-band weather radar) and satellite-based (SEVIRI) systems. We applied the methodology to the 23rd November 2013 Etna paroxysm, which benefited from north-easterly wind direction that dispersed the tephra over the Calabria towards the Puglia (Italy) and Albania regions. The available observations in terms of tephra loadings and airborne ash dispersal were used to reconstruct numerically (through the FALL3D model) the eruption features from the source to distal areas. In fact, the field-based TGSD reproduces only the sampled tephra loadings, whereas the Radar TGSD refers to a limited range of ash classes preventing its use within FALL3D as initial TGSD. We produced an Integrated TGSD (i.e. weighting average of field + radar distributions) to best-fit the tephra loadings. The inversion results yield a TGSD made of 75 wt% of the Field TGSD and 25 wt% of the Radar TGSD. However, the Integrated TGSD does not account for the far-travelling airborne ash mass retrieved from satellite (i.e. PM_{20}). We empirically modified the Integrated TGSD to implement the SEVIRI retrievals by investigating diverse PM_{20} fractions (i.e. 0.6-10.7 wt%), until we best-fit the measurements. The inverted PM_{20} fraction best-matching the SEVIRI data ranges from 3.6-9.0 wt%, depending on capturing the whole airborne ash mass or the mass per unit area. This study highlighted the need for improving the integration of data from different instruments to better quantify tephra loading and airborne mass (i.e. PM_{20}, ice, and gas), especially when aerosol clouds are produced during the eruption. From a computational point of view, the assessment of the initial TGSD would benefit from such integration, being widely used for modelling purposes such as for air traffic safety. This work aims at being of interest for developing new methods or tools capable to assess the full size-spectrum TGSD.

Supplement

The supplement associated with this manuscript serves for illustrating the results in terms of individual grain-size distributions with the Integrated TGSD, which is validated on the basis of the tephra samples (Figure V.S1). The time-series animations aim at highlighting the main eruption features (i.e. whole tephra loading and airborne ash dispersal). The supplement files are available through the following link:

https://drive.google.com/open?id=19VqQAUfmzzWFi3_FDM-YwiAvtM_G9S0v

Figure V.S1: Comparison of the 7-individual field-derived GSDs with the computed ones through the FALL3D model. The figure indicates the reproducibility of the local GSD by peaking at the same mode. The shifted GSDs are discussed in the main text.

Animation V.A1: The time-series animation refers to the dynamic evolution of the volcanic ash cloud travelling from the source retrieved from SEVIRI (i.e. 09:30-14:30).

Animation V.A2: The time-series animation corresponds to the simulation of the tephra loading obtained for the Whole TGSD with $\gamma = 0.65$. The animation shows the temporal expansion of the tephra fallout indicating the affected areas (i.e. 09:30-14:30).

Animation V.A3: The time-series animation shows the simulation of the airborne ash dispersal associated with the Whole TGSD produced with $\gamma = 0.40$ (i.e. 09:30-14:30). This animation indicates the temporal dispersal obtained with the initial injection of 3.6 wt% of PM_{20} into the atmosphere. The major lobe goes towards Albania, which corresponds to the ice/gas volcanic cloud, whereas the minor lobe (i.e. tail) spreads towards the Puglia region (southern Italy) and is related to the volcanic ash cloud.

Animation V.A4: The time-series animation is referring to the simulation of the far-travelling airborne ash dispersal computed with the Whole TGSD for $\gamma = 0.65$ (i.e. 09:30-14:30). This animation shows a similar dispersal than for the Animation V.A3. However, using $\gamma = 0.65$ means the initial injection of 9.0 wt% of PM_{20} into the atmosphere, which results on higher ash mass values, especially for the major lobe spreading towards Albania.

Author contributions

M. Poret conceived the idea and defined the project approach together with A. Costa, S. Corradini, and L. Merucci. M. Poret and A. Costa compiled the FALL3D simulations and co-wrote the manuscript. S. Corradini and L. Merucci provided and processed the SEVIRI data. G. Vulpiani and M. Montopoli provided and processed the X-band weather radar data. D. Andronico provided and processed the field data. V. Freret-Lorgeril provided and processed the VOLDORAD 2B data. All the co-authors work on the interpretation of the results and finalization of the manuscript.

Chapter VI – Modelling tephra dispersal and ash aggregation: The 26th April 1979 eruption, La Soufrière St. Vincent

Modelling tephra dispersal and ash aggregation: The 26th April 1979 eruption, La Soufrière St. Vincent

M. Poret[1, 2]; A. Costa[1]; A. Folch[3]; and A. Martí[3]

[1] Istituto Nazionale di Geofisica e Vulcanologia, Sezione di Bologna, Bologna, Italy
[2] University of Bologna, Geophysics department, Bologna, Italy
[3] CASE Department, Barcelona Supercomputing Center, Barcelona, Spain

Abstract

On the 26th April 1979, La Soufrière St. Vincent volcano (West Indies) erupted producing a tephra fallout that blanketed the main island and the neighbouring Bequia Island, located southwards. Using deposit measurements and the available observations reported in Brazier et al. (1982), we estimated the optimal eruption source parameters, such as the MER, the TEM and the TGSD by means of a computational inversion method. Tephra transport and deposition were simulated using the 3D Eulerian model FALL3D. The field-based TGSD reconstructed by Brazier et al. (1982) shows a bi-modal pattern having a coarse and a fine population with modes around 0.5 and 0.06 mm, respectively. A significant amount of aggregates was observed during the eruption. To quantify the relevance of aggregation processes on the bulk tephra deposit, we performed a comparative study in which we accounted for aggregation using three different schemes, computing ash aggregation within the plume under wet conditions, i.e. considering both the effects of air moisture and magmatic water, consistently with the eruptive phreatomagmatic eruption features. The sensitivity to the driving meteorological model (WRF/ARW) was also investigated by considering two different spatial resolutions (5 and 1 km) and model output frequencies. Results show that, for such short-lived explosive eruptions, high-resolution meteorological data are critical. Optimal results best-fitting all available observations indicate a column height of ~12 km above the vent, a MER of ~7.8×10^6 kg/s which, for an eruption duration of 370 seconds, gives a TEM of ~2.8×10^9 kg. The optimal aggregate mean diameter obtained is 1.5Φ with a density of 350 kg/m^3, contributing to ~22 wt% of the deposit mass.

Keywords: Tephra fallout; aggregation; FALL3D; WRF/ARW; TGSD; Eruption Source Parameters, La Soufrière St. Vincent

Introduction

On 26th April 1979, La Soufrière St. Vincent volcano (West Indies) produced a phreatomagmatic eruption due to interaction between the shallow aquifer and magma. The phreatomagmatic phase of the eruption produced a significant amount of aggregates, which were observed in-situ during fallout and were also evident from the grain-size features of the collected samples. Indeed, tephra deposits showed a rich fine ash composition at proximal and medial locations [Brazier et al., 1982; 1983]. Despite these observations, quantifying aggregation formed within a volcanic plume from field data is a challenging task due to the aggregates tendency to disaggregate when impacting the ground [Brazier et al., 1982]. At the end of the eruption, 33 field samples were collected providing tephra loadings at each location (Figure VI.1a). These samples are valuable to constrain simulations and quantify the role of ash aggregation combining field measurements and models.
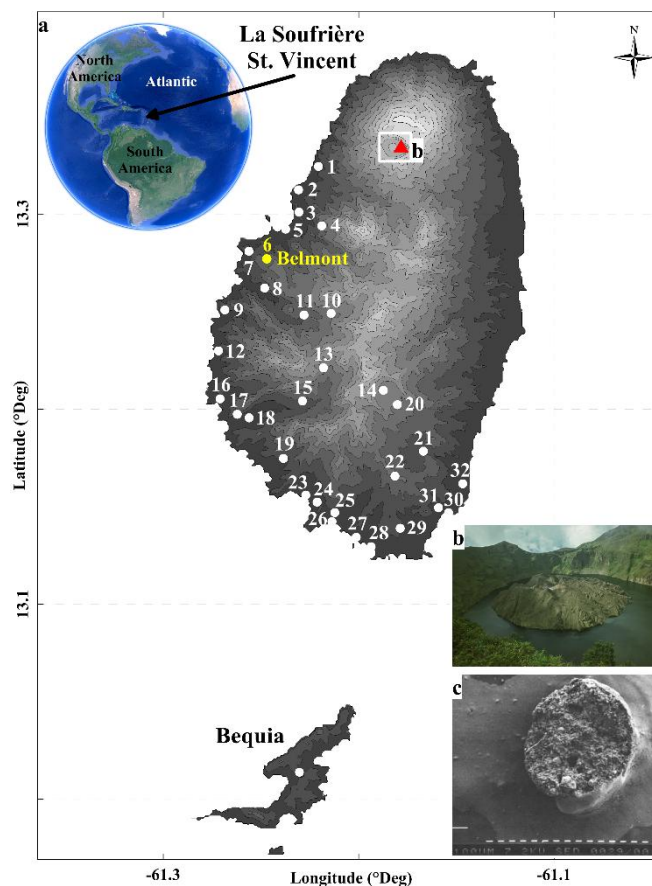
Figure VI.1: a) Location of La Soufrière St. Vincent volcano (West Indies). White dots are sample locations (detailed in Table VI.1) from the vent (red triangle) to Bequia Island. Location n°6 refers to the Belmont observatory (yellow dot). b) Photo of the permanent lake inside the summit crater before the April 1979 eruptive activity. Source: André Guyard. c) Example accretionary lapillus observed during the eruption. White bars are 100 μm in length. [Brazier et al., 1982 – modified]

This paper investigates the relevance of aggregation processes on the bulk tephra deposit for the 26th April, 1979 La Soufrière St. Vincent eruption. Different TGSDs are evaluated, including: i) the field-based TGSD derived from the sample analysis; ii) a parameterization of the latter using a bi-lognormal distribution and; iii) using a bi-Weibull distribution [Costa et al. 2016a; 2017]. Simulations also account for aggregation by considering three different aggregation schemes implemented in FALL3D. Results are compared with simulations in which aggregation is neglected. ESP optimal values are obtained through a computational inversion method previously presented by Folch et al. [2010] and Martí et al. [2016]. Simulation results are compared with field measurements by employing a criterion as the goodness-of-fit measure test, which selects consistent results that better reproduce the measured tephra loadings.

Next Section provides a short overview of the eruption. The followings describe the computational model and methodology. Then, we present the results of the comparative study on different TGSDs and aggregation schemes. The last Section discusses the results in terms of effect of the parameterization used to reconstruct the main features of a short-lived explosive eruption.

26th April 1979 eruption - La Soufrière St. Vincent

The 1979 La Soufrière St. Vincent eruptions started on the 8th April and lasted for more than two weeks with 11 eruption columns [Shepherd and Sigurdsson, 1982; Brazier et al., 1982; 1983]. After the previous event on 1971, a lava dome had slowly grown in the middle of the ~1.6 km wide summit crater lake (Figure VI.1b), creating an island that gradually filled up the crater. On the 26th April, a short-lived violent eruption started at 03:58 (midnight LT) and lasted up to 04:04, with a duration of 370 seconds (~6 min) according to the seismic records. Meteorological observations reported a cloudless night with no rain. Brazier et al. [1982] estimated the first eruptive column height around 7-8 km a.s.l. during the first minutes, which was measured from the Belmont Observatory (~10 km far from the vent; label 6 in Figure VI.1a). Then, the plume rose up to ~14 km a.s.l., giving an approximate rise velocity of around 25-30 m/s. The plume was strongly controlled by northerly winds that dispersed tephra southwards blanketing most of St. Vincent and Bequia Islands. The short duration of the 26th April event allowed the observation of a rapid disconnection of the rising plume from the vent of ~2-3 km after a few minutes (Brazier et al. [1982]; Figure 14 therein). Then, satellite observations showed a split of the plume into a major and a minor lobe. The latter one spread eastwards over the sea with no possibility for the tephra fallout to be sampled. In contrast, soon after the eruption the major lobe was sampled at 32 locations on the main island and 1 on Bequia Island (Figure VI.1a and Table VI.1). Deposit samples were analysed using the sieving method [Walker, 1971] down to d = 90 µm with a 0.5 Φ interval and, for ash finer than 90 µm, employing the electro-resistance technique with an Elzone PDll01 celloscope as described by Muerdter et al. [1981].

	Field observations			Computed loadings (kg/m^2)		
Location	X (°Deg)	Y (°Deg)	Load (kg/m^2)	Brazier TGSD	bi-Gaussian	bi-Weibull
1	-61.221877	13.321861	8.94	—	—	—
2	-61.231127	13.313686	14.15	—	—	—
3	-61.230555	13.301077	4.82	0.85	0.77	0.85
4	-61.218897	13.294033	5.25	3.94	3.40	3.80
5	-61.23738	13.292358	5.22	0.47	0.45	0.51
6	-61.247055	13.277122	0.95	0.60	0.61	0.69
7	-61.256228	13.28102	0.56	0.33	0.33	0.37
8	-61.248063	13.262062	1.06	0.57	0.61	0.68
9	-61.268513	13.250857	0.43	0.35	0.37	0.40
10	-61.214102	13.249161	1.79	6.69	6.71	7.61
11	-61.228019	13.248297	1.45	2.50	2.60	2.91
12	-61.27176	13.230013	0.30	0.14	0.15	0.15
13	-61.218021	13.221249	2.32	3.47	3.56	3.90
14	-61.18733	13.209672	1.91	2.79	2.90	3.28
15	-61.228753	13.204211	0.73	1.76	1.75	1.75
16	-61.270987	13.205405	0.23	0.67	0.65	0.62
17	-61.262154	13.197381	0.51	0.66	0.64	0.59
18	-61.256024	13.195622	0.44	0.71	0.68	0.63
19	-61.238466	13.174846	0.66	1.70	1.60	1.45
20	-61.180231	13.202388	1.73	2.02	2.10	2.37
21	-61.166841	13.178468	1.13	0.76	0.78	0.86
22	-61.181437	13.165772	1.10	1.03	1.02	1.00
23	-61.227063	13.155969	1.02	1.86	1.75	1.53
24	-61.221264	13.152389	0.95	1.85	1.74	1.51
25	-61.212177	13.147087	0.89	1.50	1.40	1.21
26	-61.21363	13.142312	0.75	1.38	1.29	1.11
27	-61.201249	13.134382	0.64	1.24	1.16	0.98
28	-61.19366	13.129567	0.44	1.03	0.96	0.80
29	-61.178734	13.138937	0.57	0.67	0.63	0.54
30	-61.154047	13.146989	0.39	0.23	0.22	0.21
31	-61.15914	13.149486	0.51	0.29	0.29	0.27
32	-61.146673	13.161864	0.43	0.19	0.19	0.20
Bequia	-61.230296	13.014004	0.45	0.05	0.06	0.16

Table VI.1: Coordinates and tephra loadings for the 33 samples. The computed loadings are related to the optimal results for the three input TGSDs (Brazier, bi-Gaussian and bi-Weibull TGSDs, respectively) with the Costa aggregation scheme (bottom panels in Figure VI.6).

One remarkable feature of this eruption was the formation of a significant amount of loose and weakly bounded aggregates and accretionary lapilli (Figure VI.1c). Due to disintegration during tephra fallout, in-situ observations [Brazier et al., 1982] estimated only an aggregate fraction of 10 wt% (accretionary lapillus), with a mean diameter between 1 and 3 mm. Brazier et al. [1982] showed that most of the collected samples clearly had a bi-modal distribution and reported the GSD of 4 samples (labels 3, 6, 25 and Bequia in Figure VI.1a), which show a fine sub-population mode at 4-5 Φ. These samples are used for a comparative study against the computed GSDs at the sample locations.

Computational models and best-fitting methodology

Tephra dispersal and plume models

Tephra deposits for the 26th April 1979 St. Vincent eruption are reconstructed using the tephra dispersal model FALL3D. The model requires the eruption source term parameters of the event together with the meteorological data over the corresponding domain (Figure VI.1a). We use FPlume [Folch et al., 2016] to obtain the MER and the effective particle grain-size distribution resulting from wet aggregation occurring within the plume. In our context, La Soufrière St. Vincent is a basaltic-andesitic volcano with around 6 wt% of water within magmas at 1100 K [Brazier et al., 1982; Heath et al., 1998].

Within FPlume, particle-particle aggregation is controlled by the presence of water from both magmatic and atmospheric origins [Costa et al., 2010; Folch et al., 2010; 2016]. Ash aggregation effects on the plume transport are investigated through a comparative study that first neglects (hereinafter *None*) and, then accounts for aggregation processes making use of:

i) Cornell scheme (hereinafter *Cornell*; Cornell et al. [1983]). This parameterization assumes an effective aggregated class with a diameter d_{Agg} (or Φ_{Agg}) and density ρ_{Agg}, formed by 50 wt% of particles with diameter 63-44 μm ash, 75 wt% of 44-31 μm, and 90 wt% of ash smaller than 31 μm.

ii) Percentage scheme (hereinafter *Percentage*; Sulpizio et al. [2012]) assumes an effective aggregated class with a diameter d_{Agg} (or Φ_{Agg}) and density ρ_{Agg}, composed by depleting of a constant percentage each particle class involved in aggregation (i.e. classes characterized by primary particle diameter lower than d_{Agg} or greater than Φ_{Agg}). The constant percentage is inverted to best-fit the field deposit.

iii) Costa scheme (hereinafter *Costa*; Costa et al. [2010]; Folch et al. [2010]) considers wet aggregation under an effective aggregated class characterized by a diameter d_{Agg} (or Φ_{Agg}) and density ρ_{Agg}. *Costa* is based on two pre-calibrated parameters, the fractal exponent (D_f) and the aggregate settling velocity correction factor (ψ_e) related to aggregate porosity. This option represents a compromise between the full aggregation processes described by the

Smoluchowski equation [Smoluchowski, 1917] and the need to reduce the bulk computational cost.

Meteorological model

FALL3D requires time-dependent wind fields and other meteorological variables such as air temperature and moisture over the computational domain. Here, we use the mesoscale WRF/ARW model [Skamarock et al., 2008] at two different spatial resolutions of 1 and 5 km to furnish meteorological data every 15 minutes. Initial and boundary conditions for WRF/ARW during the simulated period (i.e. from 25th April at 00 to 29th April at 00) were obtained from ECMWF, ERA-Interim-Reanalysis branch (www.ecmwf.int), which provides 4-times daily data at 37 pressure levels (up to 1 mb) and 0.75° horizontal resolution. A nested strategy was adopted with inner domains at 5 and 1 km spatial resolution in order to investigate the role of meteorological model resolution in case of a short-lived eruption on complex steep terrains like St. Vincent Island.

TGSD estimation

Figure VI.2 (bars) shows the TGSD estimated from 33 tephra deposits (Brazier et al. [1982]; hereinafter Brazier TGSD), ranging from -2 to 8Φ with two modes at 1Φ and 4Φ referring to the coarse- and fine-grain sub-populations, respectively. The TGSD bi-modality was originally interpreted as a result of the lack of ground measurements beyond 36 km from the volcano (Brazier et al., 1982). Later, this was attributed by Brazier et al. [1983] to the premature fallout of fine ash deposited as aggregates. More recently, Costa et al. [2016a; 2017] showed how the presence of two different sub-populations within the TGSD is a common feature for most eruptions when they are properly sampled up to distal region. In any case, bi-modal granulometry features within the individual grain-size distributions on tephra deposits from proximal to distal locations are a clear signature of ash aggregation [Brazier et al., 1983; Durant et al., 2009].

bi-Gaussian		bi-Weibull	
μ_1	0.557 ± 0.067	λ_1	0.269 ± 0.020
σ_1	1.146 ± 0.059	n_1	0.637 ± 0.039
μ_2	4.084 ± 0.049	λ_2	0.028 ± 0.001
σ_2	1.344 ± 0.045	n_2	0.875 ± 0.059
p	0.362 ± 0.020	q	0.495 ± 0.053

Table VI.2: Main parameters used to best-fit the Field TGSD.

Starting from Brazier's TGSD estimation, we described the TGSD as the sum of two lognormal distributions (Figure VI.2; bi-Gaussian in Φ; hereinafter bi-Gaussian distribution) and through the sum of two Weibull distributions (Figure VI.2; bi-Weibull in Φ; hereinafter bi-Weibull distribution) and discretized for each Φ-unit. The corresponding best-fit parameters for the two analytical curves are reported in Table VI.2. FALL3D uses the input TGSD as discrete size bins. While the Brazier TGSD provides the field-based GSDs for each bin, the GSDs derived from both the bi-Gaussian and bi-Weibull distributions are estimated through Equations I.1 and I.2 (Section I.4), respectively, and reported in Table VI.3. Additionally, we assigned the mean density for each size bin according to the simple parameterization of Bonadonna and Phillips [2003] for an andesitic magma.
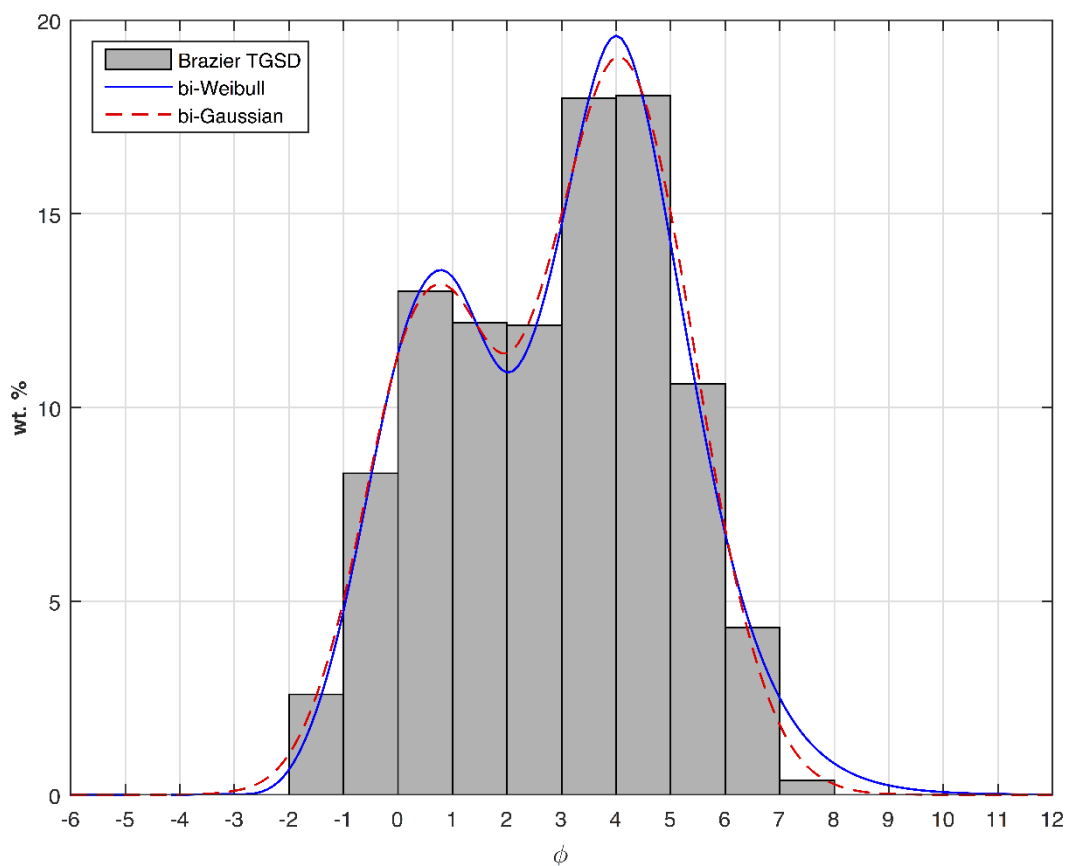
Figure VI.2: Histogram shows the field-based TGSD [Brazier et al., 1982]. The red dashed curve represents its best-fit with two lognormal distributions and the blue solid line with two Weibull distributions [Costa et al., 2016a; 2017]. Analytical curve parameters are reported in Table VI.2.

Diameter (Φ-unit)	Weight (in wt%)		
	Brazier TGSD	bi-Gaussian TGSD	bi-Weibull TGSD
-6	0.00	0.00	0.00
-5	0.00	0.00	0.00
-4	0.00	0.00	0.00
-3	0.00	0.10	0.02
-2	2.59	1.05	0.65
-1	8.30	5.02	4.74
0	12.99	11.37	11.40
1	12.19	13.04	13.37
2	12.13	11.39	10.90
3	17.98	14.99	14.72
4	18.05	19.05	19.60
5	10.61	15.03	14.23
6	4.32	6.86	6.74
7	0.38	1.80	2.50
8	0.00	0.27	0.81
9	0.00	0.02	0.24
10	0.00	0.00	0.07
11	0.00	0.00	0.02
12	0.00	0.00	0.01

Table VI.3: Grain-size distributions for the Brazier TGSD accompanied by the ones derived from the bi-Gaussian and bi-Weibull distributions (Figure VI.2).

Inverse problem-solving methodology

A set of FALL3D model runs was performed by exploring the ranges of the input parameters in Table VI.4 (see the Appendix VI.A for the complementary description of the models and parameterization used). Optimal ESP values were obtained by best-fitting the observed loadings with the field measurements through the evaluation of the goodness-of-fit making use of different statistical parameters. The goodness-of-fit method considered *RMSE* calculated using two different weights (i.e. *RMSE₁* and *RMSE₂*) by the following equations:

$$RMSE_j = \sqrt{\sum_i^N w_j (Sim_i - Obs_i)^2}$$

(VI.1)

where w_j refers to the weighting factors used to determine the *RMSE*. The index i corresponds to the ith sample over a set of N samples. The terms Obs_i and Sim_i are respectively the observed and simulated tephra loadings and:

$$w_{j=1} = \frac{1}{\sum_i^N Obs_i^2}$$

(VI.2)

$$w_{j=2} = \frac{1}{N \times Obs_i^2}$$

(VI.3)

These weights correspond to different assumptions on the error distribution [Costa et al., 2009]. The *RMSE₁* is calculated with w_1 and refers to the case of a constant absolute error, whereas the *RMSE₂* considers a constant relative error implying the proportional weighting factor w_2 [Folch et al., 2010]. In addition to these *RMSE* skills, we also computed the statistical indexes K (i.e. geometric average of the distribution) and k (i.e. geometric standard deviation of the distribution) introduced by Aida [1978]:

$$K = exp\left[\frac{1}{N}\sum_i^N \log\left(\frac{Obs_i}{Sim_i}\right)\right]$$

(VI.4)

$$k = exp\left[\sqrt{\frac{1}{N}\sum_i^N \log\left(\frac{Obs_i}{Sim_i}\right)^2 - \left(\frac{1}{N}\sum_i^N \log\left(\frac{Obs_i}{Sim_i}\right)\right)^2}\right]$$

(VI.5)

Simulations are considered reliable when K lies between 0.95 and 1.05 (i.e. ±5% of the mass estimation). The optimal simulations (Table VI.5) are selected when k is minimized together with *RMSE₁* and *RMSE₂*. Additionally, results of the simulations are chosen on the basis of the minimum *bias* and the maximum *correlation* [Costa et al, 2009; Folch et al., 2010], where the normalized *bias* is calculated as [Folch et al., 2010]:

$$Bias = \frac{\sum_i^N(Sim_i - Obs_i)}{\sum_i^N Obs_i}$$

(VI.6)

For solving the inversion, we sampled at regular intervals through the ranges of the main parameters governing the tephra transport and sedimentation. Then, we refined the search using finer steps around the values giving the best goodness-of-fit. We started with the eruptive column height by exploring from 10 to 16 km above the vent. Through the relationship between the column height and the MER [Folch et al., 2016], column heights were obtained varying MERs from 10^4 to 10^8 kg/s. The exit velocity, temperature and water fraction are sampled from 150 to 300 m/s, 1000 to 1200 K and 4 to 6.5 %, respectively. In addition to these ESPs, FPlume needs two entrainment coefficients (α and β), which were explored from 0.1 to 0.15 and from 0.3 to 1.0, respectively. Regarding the aggregation parameterization, the diameter (Φ_{Agg}) and density (ρ_{Agg}) of the aggregated class were chosen respectively within the ranges 0 to 2 Φ and 100 to 800 kg/m³.

Input Parameter	Explored Range	
Height (km above vent) [a]	10	16
MER (kg/s) [a]	10^4	10^8
Exit velocity (m/s)	150	300
Exit temperature (K)	1000	1200
Exit water fraction (%)[b]	4.0	6.5
Cross-flow entrainment coefficient (β) [c]	0.3	1.0
Radial entrainment coefficient (α) [c]	0.1	0.15
Aggregate diameter (Φ-unit)	0	2
Aggregate density (kg/m³)	100	800

Table VI.4: [a] The column height and MER are estimated using the FPlume model [Folch et al., 2016]. [b] The magma exit water fraction is set accordingly to the literature [Brazier et al., 1982; 1983; Heath et al., 1998]. [c] The entrainment coefficients (α and β) are set to a constant value (CONSTANT option in FPlume model). [d] Aggregation is investigated using the following schemes: *None* (i.e. no aggregation), *Cornell* (Cornell et al. [1983], modified), *Percentage* [Sulpizio et al., 2012], and *Costa* [Costa et al., 2010]. The complementary values are reported in Table VI.5.

Results

Here we present the results of the solution of the inverse problem together with sensitivity studies on tephra dispersal making use of: i) three different TGSD and ii) the effects of different ash aggregation parameterizations. A sensitivity study on the meteorological model spatial resolution was also performed and is available in the Supplement (Figure VI.S1).

ESP estimation solving an inverse problem for the different TGSD

For the sake of clarity, the following section reports the use of the *Costa* aggregation scheme but all the optimal sets of ESPs are summarized in Table VI.5 together with the statistical response. The interdependency of many of the input parameters implies that the reported optimal results are not unique [Anderson and Segall, 2013] and may differ with other ESP combinations [Connor and Connor, 2005; Scollo et al., 2008]. The inversion procedure consists of running hundreds of simulations covering the ranges of the main parameters (Table VI.4) and choosing the combination that optimizes the tephra transport and sedimentation.

Brazier TGSD	Aggregation scheme			
Input parameter	*None*	*Cornell*	*Percentage*	*Costa*
Column height (km above vent)	12	12	12	12
MER (kg/s)	6.8×10^6	5.5×10^6	7.1×10^6	6.5×10^6
Exit velocity (m/s)	250	250	250	250
Exit temperature (K)	1100	1100	1100	1100
Exit water fraction (%)[b]	6	6	6	6
Cross-flow entrainment coefficient (β) [c]	0.85	0.60	0.90	0.80
Radial entrainment coefficient (α) [c]	0.13	0.13	0.13	0.13
Aggregate diameter (Φ-unit)	—	1.5	1.5	1.5
Aggregate density (kg/m³)	—	450	450	450
Computed aggregate fraction (in wt%)	0.0	34.9	31.9	00.6
Statistical metric				
K	0.99	1.02	1.02	1.03
k	2.44	2.40	2.20	2.43
$RMSE_1$	0.85	0.80	0.84	0.83
$RMSE_2$	0.98	0.96	0.89	0.92
Bias	0.00	0.00	0.00	0.00
Correlation	0.60	0.50	0.60	0.60

Table VI.5: Summary of the optimal ESP values with the statistical response for the three input TGSDs for the four-different aggregation schemes (i.e. *None*, *Cornell*, *Percentage*, and *Costa*).

We reported in Figure VI.3 the main parameter (i.e. column height) having substantial effect on the resulting tephra loadings and therefor on the best-fit agreement with the measured loadings. Figure VI.3 summarizes the results in terms of $RMSE_1$, $RMSE_2$ and k showing how the goodness-of-fit is affected by varying pivotal parameters such as the column height (and the associated MER) with the *Costa* aggregation scheme. Sensitivity studies show that the effect of the column height (and associated MER) on k and $RMSEs$ is much more significant than on other parameters. As an example, the tephra loading appears to not be considerably affected by varying the aggregate density. However, k is a minimum for $\rho_{Agg} = 450$ kg/m^3 for the Brazier and bi-Gaussian TGSDs and 350 kg/m^3 for the bi-Weibull distribution.
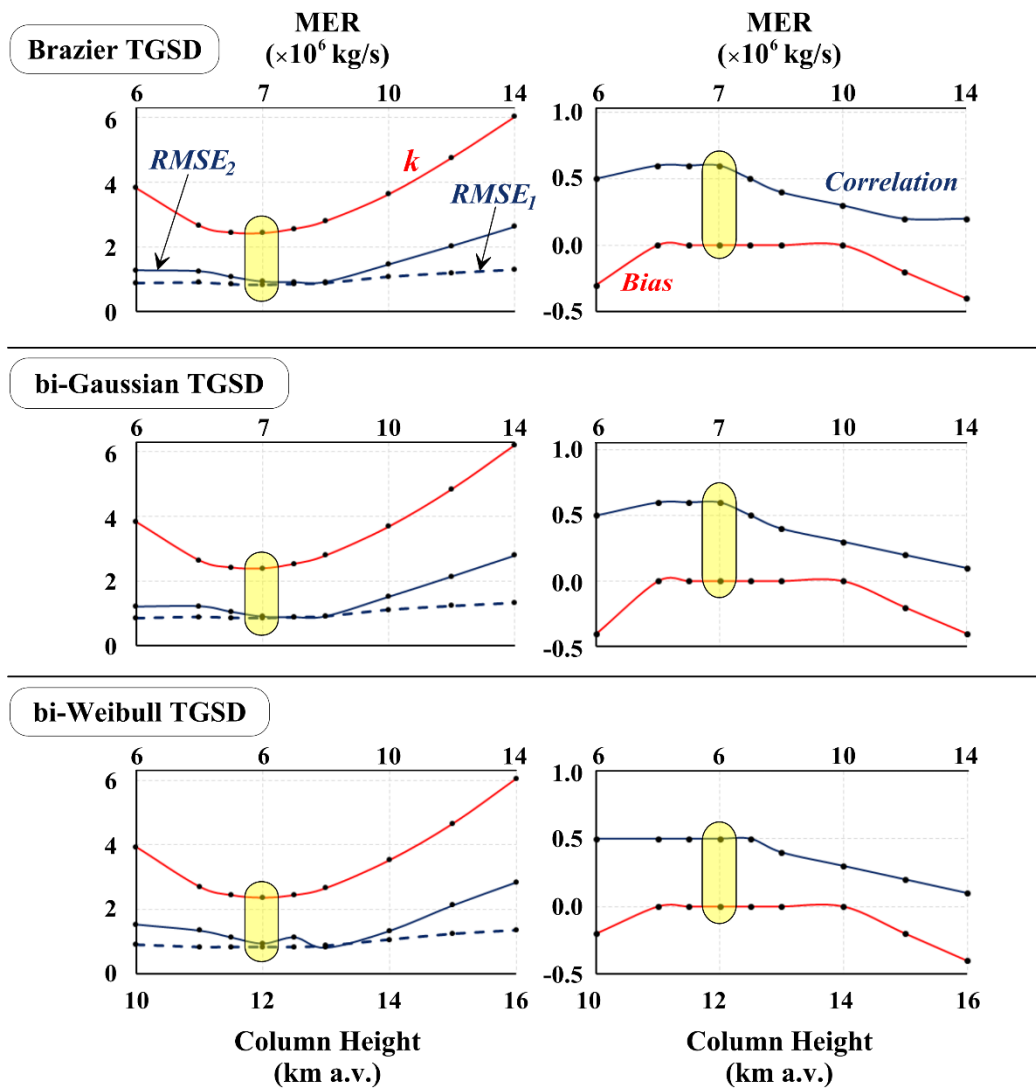
Figure VI.3: Summary of the procedure used to solve the inverse problem showing the statistical indices (*RMSE*s, *k*, *Bias* and *Correlation*) variations as function of total column height (and associated MER) for the three input TGSDs.

The optimal simulations for each TGSD with the *Costa* scheme suggest an eruptive column height of 12 km above the vent, a resulting TEM of ~2.5×10^9 kg, ~2.4×10^9 kg, and ~2.8×10^9 kg for the Brazier TGSD, bi-Gaussian and bi-Weibull distributions, respectively. These values are consistent with the TEM provided by Brazier et al. [1982], i.e. ~9.6×10^8 kg, which is ~40 % lower than our simulation results. Considering a constant MER through the 6 minutes of the eruption, the corresponding MERs for each distribution are of ~6.5×10^6 kg/s, ~6.6×10^6 kg/s, and ~7.8×10^6 kg/s, respectively. Regarding the plume air entrainment coefficients, the best-fit values for this short-lived eruption of La Soufrière St. Vincent volcano give a radial entrainment coefficient α of 0.13 and a cross-flow entrainment coefficient β of 0.95, which are within the typical ranges [Costa et al., 2016b].

bi-Gaussian TGSD	Aggregation scheme			
Input parameter	*None*	*Cornell*	*Percentage*	*Costa*
Column height (km above vent)	12	12	12	12
MER (kg/s)	6.8E+6	5.6E+6	7.1E+6	6.6E+6
Exit velocity (m/s)	250	250	250	250
Exit temperature (K)	1100	1100	1100	1100
Exit water fraction (%)[b]	6	6	6	6
Cross-flow entrainment coefficient (β) [c]	0.85	0.60	0.90	0.80
Radial entrainment coefficient (α) [c]	0.13	0.13	0.13	0.13
Aggregate diameter (Φ-unit)	—	1.5	1.5	1.5
Aggregate density (kg/m^3)	—	450	450	450
Computed aggregate fraction (in wt%)	0.0	41.1	34.7	2.2
Statistical metric				
K	1.01	1.01	1.00	1.05
k	2.46	2.42	2.23	2.39
RMSE$_1$	0.86	0.82	0.86	0.84
RMSE$_2$	0.94	0.98	0.91	0.89
Bias	0.00	0.00	0.00	0.00
Correlation	0.50	0.50	0.60	0.60

Table VI.5: Continued.

The bi-Weibull distribution combined with the *Costa* scheme give statistical indexes of $K = 1.02$ and $k = 2.18$ for the optimal simulation, whereas both the *RMSE$_1$* and *RMSE$_2$* are calculated at ~0.89 (see Table VI.5 for a full description of the results). These values indicate an error associated with the ESP estimation similar to the uncertainty associated with other classical

methods [Bonadonna and Costa 2012; 2013; Bonadonna et al., 2015c]. Figure VI.4a shows the comparison between the measured and the computed tephra loading values on a logarithmical scale at the 31 considered locations (Figure VI.1). Overall, the best simulations indicate that 94 % of the tracked samples fall between 1/5- and 5-times the observed values and 6 % (the 2 most proximal samples) fall near the 1/10- and 10-times. Figure VI.4a also compares the results obtained with the bi-Weibull distribution accounting for aggregation using the *Costa* scheme and no aggregation. It also displays the best simulations for the bi-Gaussian distribution and the Brazier TGSD with the *Costa* scheme. Overall, Figure VI.4a illustrates how accounting for aggregation improves the fit. Table VI.5 summarizes the goodness-of-fit results obtained for the three TGSD employed in combination with the different aggregation schemes.

bi-Weibull TGSD	Aggregation scheme			
Input parameter	*None*	*Cornell*	*Percentage*	*Costa*
Column height (km above vent)	12	12	12	12
MER (kg/s)	7.4E+6	6.6E+6	8.3E+6	7.4E+6
Exit velocity (m/s)	250	250	250	250
Exit temperature (K)	1100	1100	1100	1100
Exit water fraction (%)[b]	6	6	6	6
Cross-flow entrainment coefficient (β) [c]	0.95	0.80	1.00	0.95
Radial entrainment coefficient (α) [c]	0.13	0.13	0.14	0.13
Aggregate diameter (Φ-unit)	—	1.5	1.5	1.5
Aggregate density (kg/m^3)	—	350	350	350
Computed aggregate fraction (in wt%)	0.0	42.1	34.9	22.3
Statistical metric				
K	0.95	0.98	1.00	1.02
k	2.45	2.27	2.09	2.18
$RMSE_1$	0.91	0.86	0.95	0.89
$RMSE_2$	1.03	0.94	0.93	0.89
Bias	0.00	0.00	0.00	0.00
Correlation	0.60	0.60	0.70	0.60

Table VI.5: Continued.

The table shows similar *RMSEs* (i.e. $RMSE_1$, $RMSE_2$) and *k* index values, although obtained through different parameterizations. This reflects the convergence of the simulation to best-fit the field measurements. However, despite this similarity, Figure VI.4a suggests considerable differences associated with the tephra loading at the Bequia location (0.45 kg/m²). The

simulations under aggregation improve the fitting almost by a factor 6. The 31 different computed loadings can be compared with the field measurements in Table VI.1.
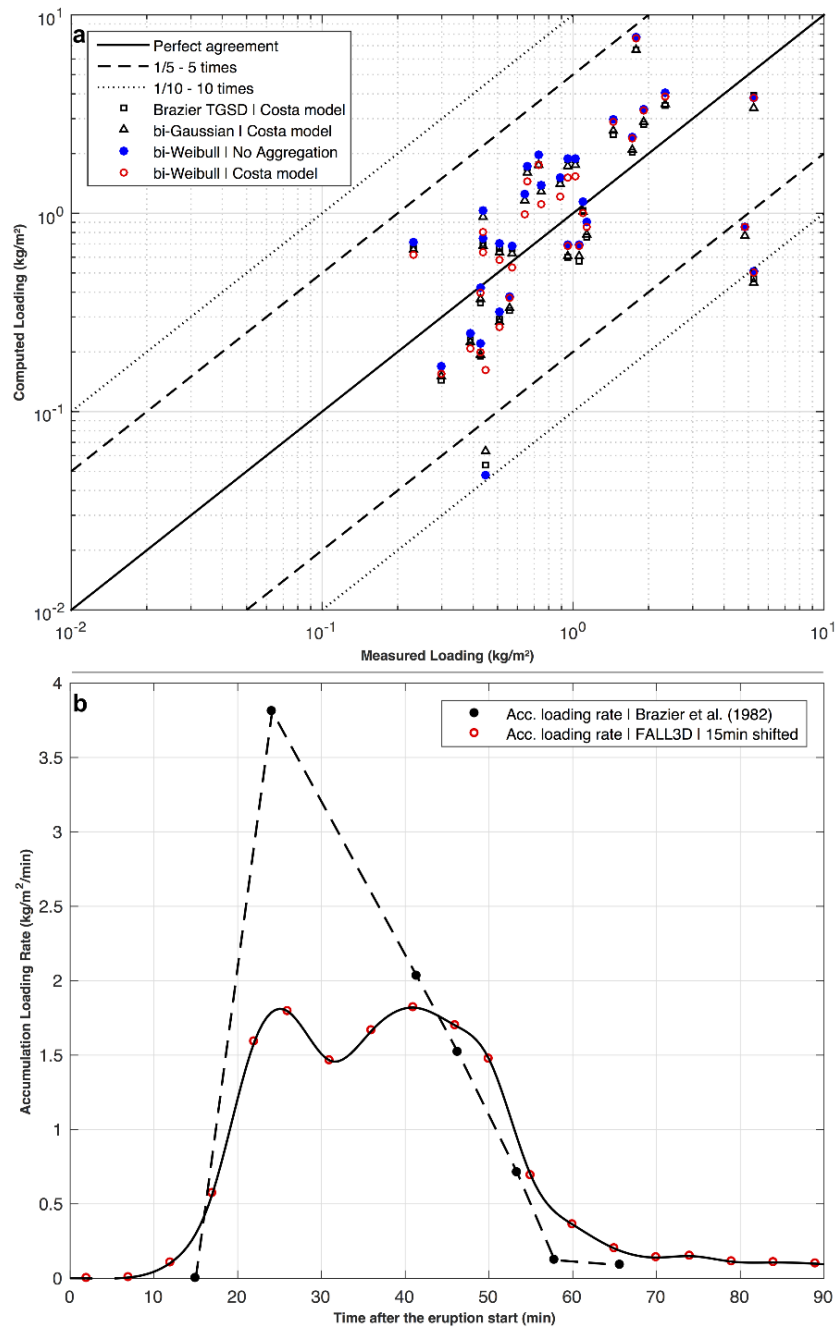
Figure VI.4: a) Comparison between the observed ground loadings and their best-fit computed values for the 31 sample locations (loading details in Table VI.1). Reported results refer to the use of the *Costa* scheme [Costa et al., 2010] with the Field TGSD (squares), the bi-Gaussian (triangles), and the bi-Weibull distributions (unfilled red circles). Blue spheres stand for the bi-Weibull distribution neglecting aggregation (i.e. *None* scheme). b) Comparison of the tephra accumulation loading rate from field-based observations [Brazier et al., 1982] at Belmont Observatory (black dots with dashed line) with the computed rate (red dots with solid line).

In addition to the best-fit tephra loadings, the observed accumulation rate (in kg/m²/min) made at the Belmont Observatory (label 6 in Figure VI.1a) is also compared against the modelled rate (Figure VI.4b). The dashed line indicates a maximum accumulation rate of ~3.8 kg/m²/min around 25 minutes after the eruption start. This trend is reproduced by the model but required a 15-minute time shift on the meteorological database to capture the proper accumulation-loading rate, which is attributed to a meteorological model phase error that does not represent correctly the meteorological fields. From a computational point of view, this operation is done by shifting the eruption start by -15 minutes. In this case, a maximum of ~1.8 kg/m²/min, which is of the same order of the measured value, is obtained around 25 minutes after the eruption start.

Figure VI.5 shows the tephra loading map for the optimal simulation, i.e. with the bi-Weibull distribution and the *Costa* scheme. Besides the tephra blanket covering most of the St. Vincent and Bequia islands, the map presents an area with an expanded maximum spreading south-westwards (i.e. following the load limit of 2 kg/m²), which is associated with the aggregate fallout (see the time-series Animation VI.A1 in the Supplement). In this case, ash aggregation is contributing to ~22.3 wt% of the tephra fallout deposit. A time-series animation of the computed aggregate deposition is available in the Supplement (see Animation VI.A2). Further details on the effects of ash aggregation scheme on simulation results are described in the following Section.
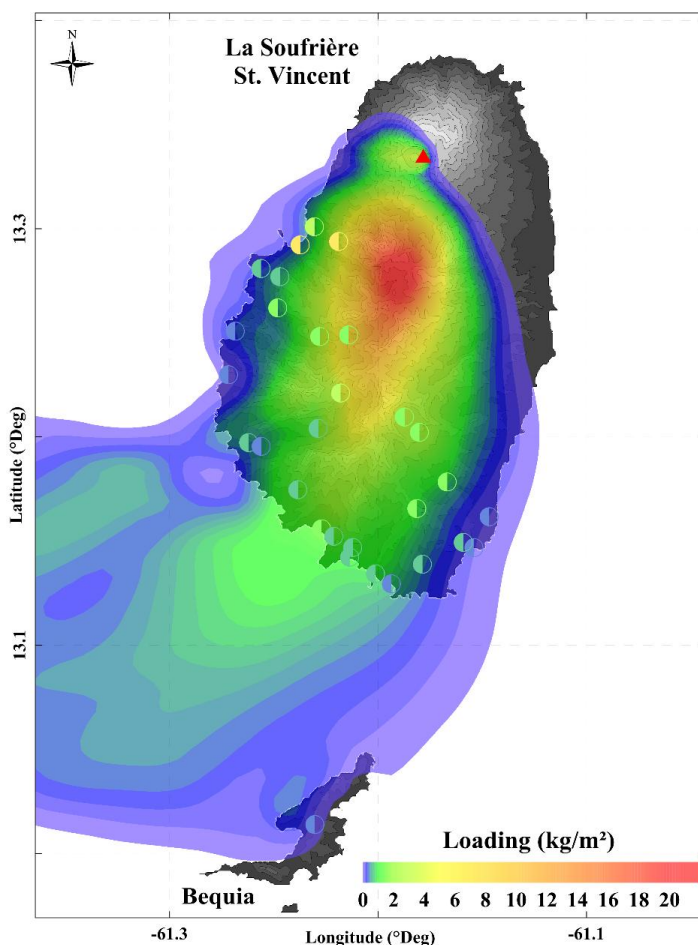

Figure VI.5: Best tephra loading map resulting from the use of the bi-Weibull distribution and the Costa scheme. Colour bar and samples colour scale are adjusted to match when computed loadings lie within the observed range value.

### *Sensitivity to parameterizations of ash aggregation*

For the sake of clarity, ash aggregation results are presented in sub-sections referring to the use of a TGSD (i.e. Brazier TGSD, bi-Gaussian and bi-Weibull distributions respectively). For each case, we show the tephra loading (Figure VI.6) and aggregate loading maps (Figure VI.7). The columns in Figures VI.6 and VI.7 display the results for each TGSD while rows illustrate the different aggregation schemes (i.e. *None*, *Cornell*, *Percentage* and *Costa*). Overall, Figure VI.6 highlights the effect of each aggregation parameterization on the tephra transport and deposition (the corresponding aggregate mass fractions are regrouped in Table VI.5). Regarding the aggregated class, simulation results give optimal values for the effective aggregate diameter of 0.35 mm (Φ_{Agg} = 1.5). The best density value is obtained at 450, 450 and 350 kg/m^3 for the Brazier TGSD, bi-Gaussian and bi-Weibull distributions respectively. The fractal exponent (D_f) required by the *Costa* scheme is set at 3. The optimal input aggregate fraction needed by the *Percentage* scheme is obtained at 50 wt% of the fines (~35 wt% for the TGSD).

Ash aggregation results for the Brazier TGSD

Tephra loading maps resulting from the use of the Brazier TGSD (left column in Figure VI.6) show the effect of the four aggregation scheme on the deposit. Results give computed aggregate mass fractions from 0 wt% (assuming no aggregation) to ~35 wt%. Although the maps show similar tephra deposits for *None*, *Cornell*, *Percentage* and *Costa* schemes, the aggregate mass fraction given by *Costa* is very low (~0.6 wt%), suggesting almost no presence of aggregates on the deposit. *Cornell* and *Percentage* schemes have a similar much higher aggregate fraction (~35 wt% and ~32 wt%, respectively), thus improving the reconstruction of the deposit at Bequia. *None* and *Costa* methods are not able to capture the field measurement at Bequia Island but *Cornell* and *Percentage* schemes do. Figure VI.7 (left column) presents the computed aggregate-loadings and shows the different contributions between the aggregation schemes.

Ash aggregation results for the bi-Gaussian TGSD

Tephra loading maps associated with the use of the bi-Gaussian distribution are summarized in Figure VI.6 (central column). The estimated aggregate mass fraction ranges from 0 wt% to ~41 wt%. As observed in the previous Section, *Costa* results in a low aggregate fraction (~2.2 wt%), explaining the similarity between the maps for *None* and *Costa*. Then, *Cornell* and *Percentage* schemes indicate similar but greater fractions (~41 wt% and ~35 wt%, respectively), increasing the deposit at Bequia visible on Figure VI.6. Again, *None* and *Costa* schemes are not able to capture the field measurement in Bequia Island, whereas *Cornell* and *Percentage* schemes show a better agreement (central column in Figure VI.7).
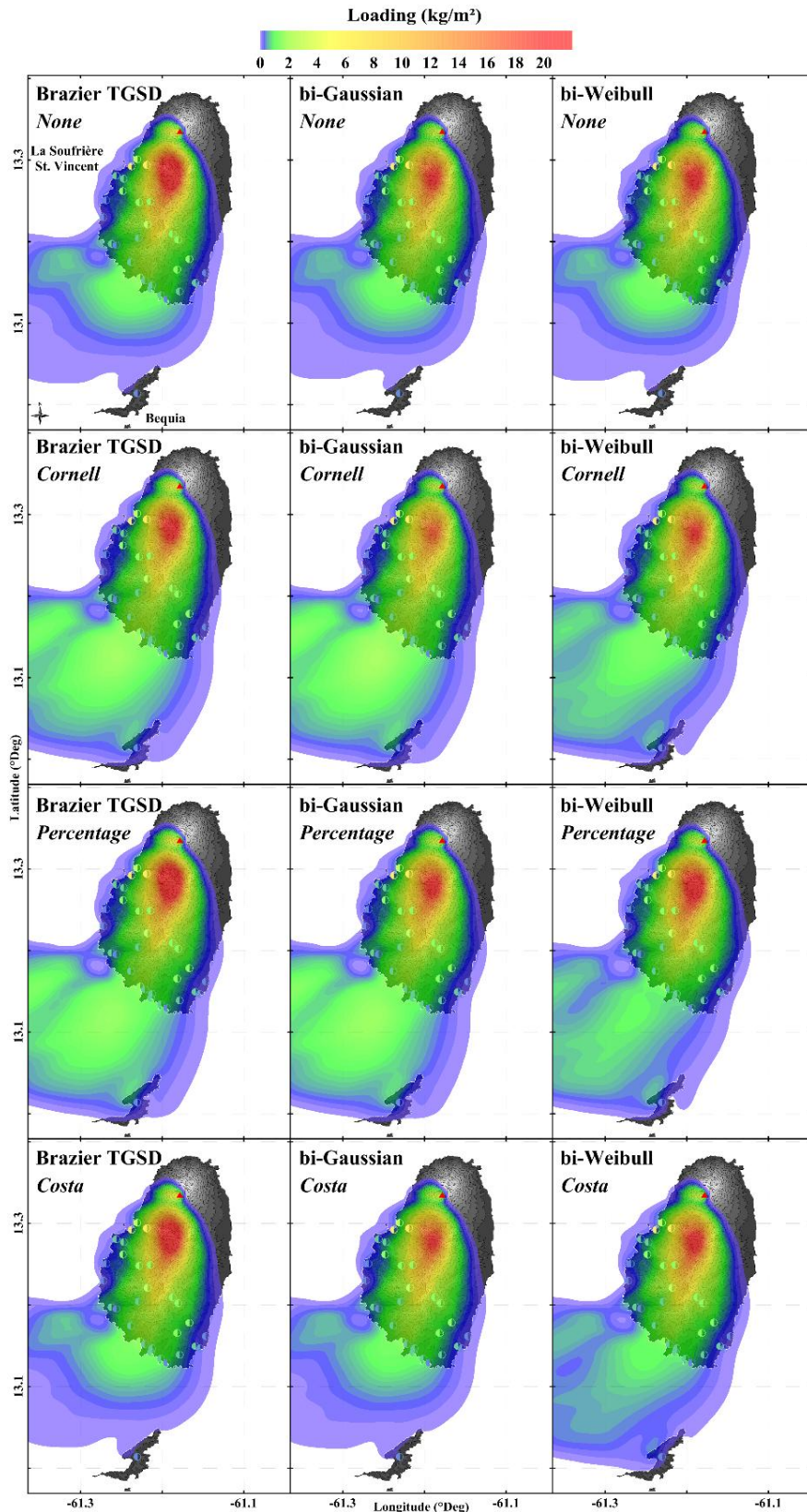
Figure VI.6: Overview of the tephra loading maps obtained for the three input TGSDs together with the four aggregation schemes (i.e. *None*, *Cornell*, *Percentage*, and *Costa*). The details are reported in Table VI.5. Colour bar and samples colour scale are adjusted to match when the computed loadings lie within the observed range value.

Ash aggregation results for the bi-Weibull TGSD

Tephra loading maps associated with the use of the bi-Weibull distribution are summarized in Figure VI.6 (right column). The computed aggregate mass fractions range from 0 wt% to ~42 wt%. The use of the bi-Weibull distribution gives a different behaviour with respect to the two latter sections. For this particular case, the *Cornell*, *Percentage* and *Costa* schemes show very similar tephra loadings together with similar aggregate fractions (~42 wt%, ~35 wt% and ~22 wt%, respectively). In particular, the statistical analysis (i.e. *RMSEs*, *K*, *k*, *bias* and *correlation*) in Table VI.5 shows the best performance for the *Costa* and *Percentage* schemes. The agreement is also visible through the simulated tephra deposits (Figure VI.6), capable to capture the loadings measured in Bequia. Figure VI.7 (right column) illustrates the aggregate loading maps, which are very similar in this case.
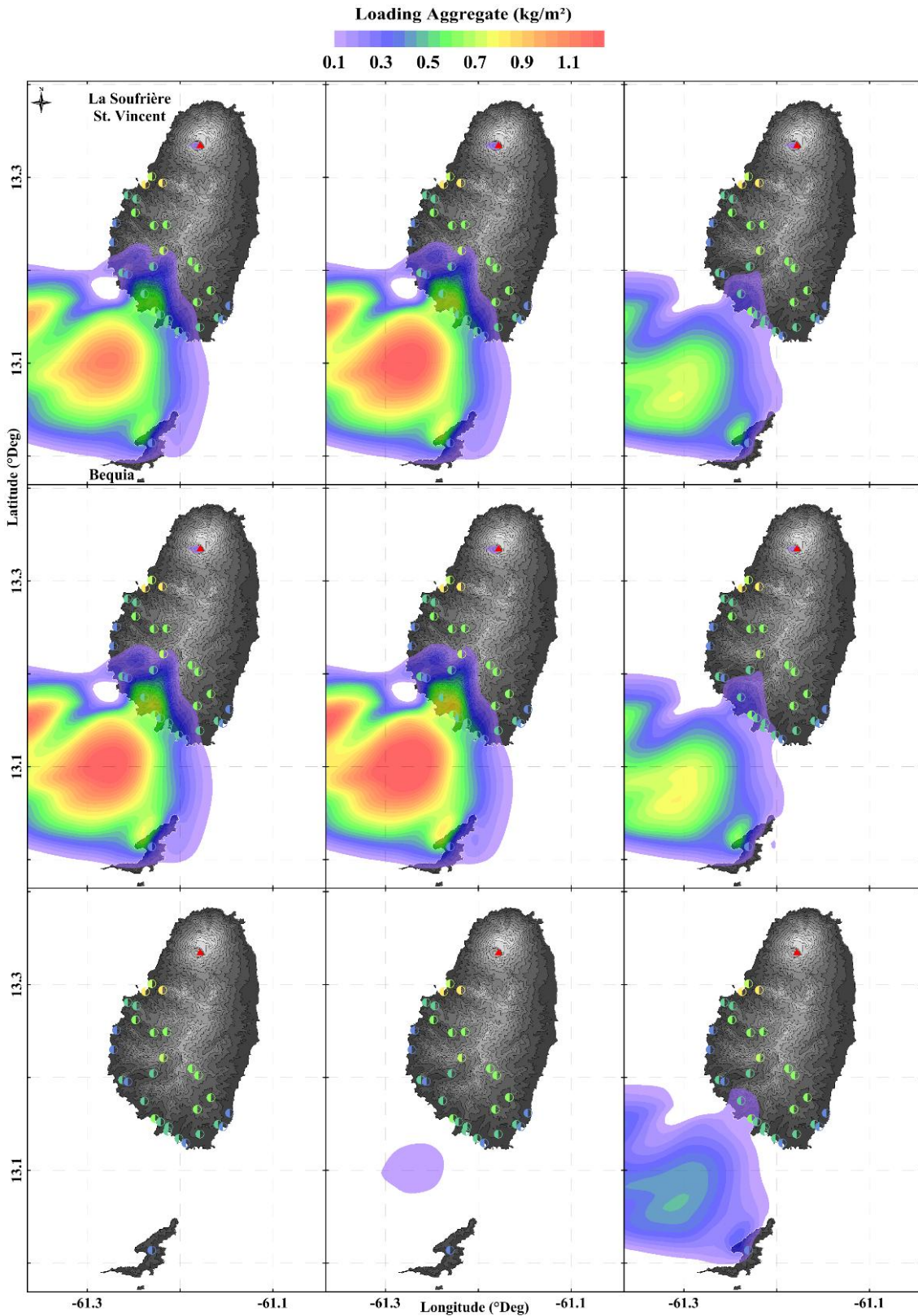
Figure VI.7: Overview of the aggregate loading maps obtained for the three explored TGSDs and the four aggregation schemes (i.e. *None*, *Cornell*, *Percentage*, and *Costa*). The details are reported in Table VI.5. Colour bar and samples colour scale are adjusted to match when the computed loadings lie within the observed range value.

Discussion

This study aims at reconstructing the main features of the 26th April 1979 eruption at La Soufrière St. Vincent volcano, constraining ESPs and ash aggregation processes using the FALL3D tephra dispersal model together with a 1 km resolution mesoscale meteorological model. Simulations are validated against all available data in terms of tephra loading, grain-size distribution and plume observations. This study allows us to gain insight into aggregation parameterizations as well as on the control of the driving meteorology on these processes.

Considering the proximal area (i.e. < 10 km from the vent), the deposit mapped may have fallen from the rising column rather than from the downwind cloud. Although the gravitational spreading [Costa et al., 2013] is taken into account by the FALL3D code, the resulting tephra loadings may show significant discrepancies due to the high unstable plume conditions and complex multiphase processes near the vent [Manzella et al., 2015; Cerminara et al., 2016; Del Bello et al., 2017]. Substantial differences between the computed and measured loadings were observed for the two closest points from the source (labels 1 and 2 in Figure VI.1). Because the tephra dispersal model limitations at very proximal region, we did not consider these two points. The eruptive column is described by the FPlume model which, for each grain-size bin (characterized by particle size, density, and shape), provides the mass flow over the entire range of elevations. Then, making use of the meteorological database FALL3D computes the transport and deposition for each grid node (i.e. longitudes and latitudes) and the elevation layers.

Amongst the main ESPs, the input TGSD plays a pivotal role in controlling tephra deposition [Costa et al., 2016a] and aggregation [Folch et al., 2016], but is particularly difficult to estimate, especially for the fine ash tail [Costa et al., 2016a and references therein]. For this reason, we carried out a sensitivity study on the TGSD by considering different estimations (Section TGSD estimation). Results associated with the TGSDs demonstrate ash aggregation to be highly dependent on the TGSD tail description (i.e. $\Phi > 5$), but also on the aggregation scheme (Table VI.5). While Brazier TGSD has only ~15.3 wt% of fine ash (bars in Figure VI.2) the bi-Gaussian distribution contains ~24.0 wt%, (red dashed line in Figure VI.2) and the bi-Weibull distribution ~24.6 wt% (blue solid line in Figure VI.2). In our context, fine ash enrichment implies a greater aggregation contribution on the medial bulk tephra fallout, which is illustrated in Figure VI.6. This figure shows (from left to right) that enriching in fine ash reproduces slightly better the tephra dispersal and deposition independently of the aggregation scheme used. This is observable by the extent of the computed tephra fallout towards the Bequia Island. However, neglecting aggregation (top panels in Figure VI.6) returns identical results regardless of the TGSD used, highlighting the non-uniqueness of the parameterization to best-fit the field observations. These results illustrate how important it is to consider aggregation together with the correct fine ash tail description of the distribution. In particular, results from the *Costa* parameterization give aggregate mass fractions from ~0.6-2.2 wt% (i.e. for Brazier TGSD and

bi-Gaussian distribution, respectively) to ~22.3 wt% (i.e. for the bi-Weibull distribution). These values indicate a strong dependency on TGSD estimation as indicated in Figures. VI.6 and VI.7. The *Percentage* (and *Cornell*) scheme indicates more stable loadings through the three TGSD and show a good agreement with the observed deposit. However, the *Percentage* scheme has a slightly better performance (Table VI.5) with respect to the optimal results obtained for the bi-Weibull TGSD with the *Costa* parameterization. The *Percentage* scheme, which has the lowest k and highest correlation, suggests similar ESPs to the other schemes but aggregate mass fraction of ~35 wt% (Table VI.5). Nonetheless, the remarkable result shown by Figure VI.6 is the non-uniqueness solution to best reproduce the field deposit, which is attributed to the interdependency of the main parameters that lead to a set of reliable parameterizations.

Figure VI.8 brings together the four GSD displayed in Brazier et al. [1982] for samples 3, 6, 25, and Bequia, respectively (located at 6, 10, 21, and 36 km from the vent; Figure VI.1a). For the sake of clarity, Figure VI.8 reports GSDs estimated with the bi-Weibull distribution. The paragraph and caption refer to the use of the *Costa* aggregation scheme. The figure shows the computed and measured GSD (hereinafter Field GSD) for all the diameter bins (i.e. $-4 < \Phi < 8$). Field GSDs present coarse and fine sub-populations. On one hand, the coarse sub-population peaks at $\Phi = 0$ (sample 3), $\Phi = 1$ (samples 6 and 25) and at $\Phi = 2$ (sample Bequia) representing tephra settling as free particles. The corresponding computed modes and variances of these GSDs are in agreement with the field observations. On the other hand, the fine sub-population, which is composed of particles that deposited as aggregates (mostly destroyed when impacting the ground, thereby releasing fine ash in the deposit) was not properly simulated, especially at proximal locations reflecting the difficulty to accurately describe the coarse tail of the TGSD without a proper sampling of the proximal area [Andronico et al., 2014a; Spanu et al., 2016]. Discrepancies for the fine sub-population can be explained by the ash aggregation schemes that consider only one single effective aggregate class rather than a distribution of aggregates with different sizes and densities [Mastin et al., 2016].

The best-case simulation results obtained for an effective aggregate diameter of $\Phi_{Agg} = 1.5$ and a density of 350 kg/m^3 using the *Costa* scheme with a bi-Weibull TGSD indicate aggregate fractions of ~0.1 wt%, ~0.4 wt%, ~5.8 wt% and ~78.2 wt%, respectively, for the samples 3, 6, 25 and Bequia (i.e. Agg class on each panel in Figure VI.8). These values can be compared with data from the relative Field GSDs, summing the measured mass fractions corresponding to the particle classes considered to settle as aggregates. The sum concerns the empty classes for *None* aggregation (Figure VI.8), i.e. $\Phi \geq 3$ for sample 3, 6, and 25 and $\Phi \geq 4$ for the Bequia sample. The resulting sums give ~68.0 wt%, ~56.0 wt%, ~61.1 wt% and ~43.6 wt%, respectively (Agg class in Figure VI.8). From a computational point of view, these latter fractions would be assigned, at least partially, in the aggregate class. While the values associated with the samples 3, 6 and 25 are not in agreement with the simulations, the performance for the Bequia is better.
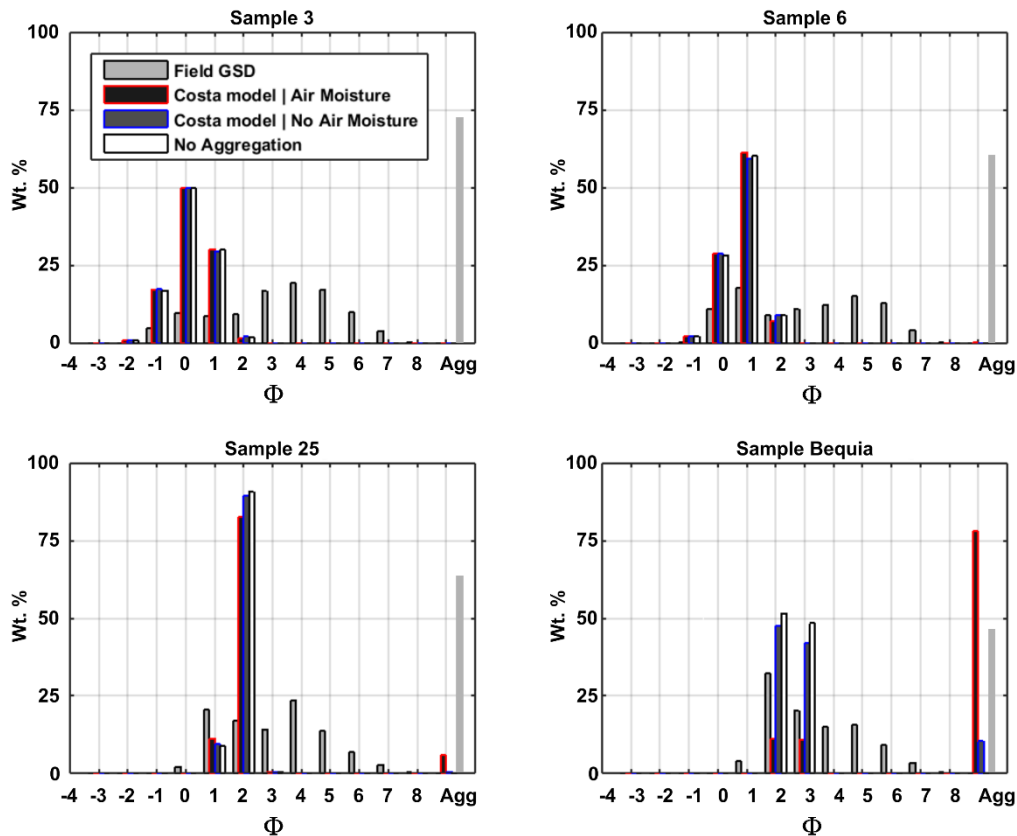
Figure VI.8: Comparison of the Field GSD (i.e. labels 3, 6, 25, and Bequia) provided by Brazier et al. [1982] with the corresponding GSD calculated by FALL3D. Light grey bars represent the sum of the fine particle classes assumed falling as aggregates.

The optimal simulation performed with the bi-Weibull distribution and the *Costa* scheme predicts an aggregate fraction of ~22.3 wt%, contributing to the tephra deposit with ~0.5 kg/m^2 as maximum. The time-series of the sedimentation associated with the effective aggregated class can be used to identify the area impacted by the deposition of aggregates, which is located south-westwards from the main island and over the ocean (see Animation VI.A2 in the Supplement). These results agree with the observation of a bi-modal grain-size distribution as well as a secondary thickening in the tephra fallout described in Brazier et al. [1983], and more recently in Mastin et al. [2016] for Mount St. Helens (18th May 1980).

Figure VI.8 highlights also the effect of air moisture on tephra dispersal and deposition by comparing GSDs obtained with the *Costa* scheme. Samples 3, 6 and 25 indicate a weak effect of the air moisture on the deposits, which is consistent with the local atmospheric conditions reported in Brazier et al. [1982] together with the phreatomagmatic nature of the eruption [Shepherd and Sigurdsson, 1982]. In contrast, effect of air moisture are significant for the Bequia deposit (bottom right panel in Figure VI.8). While the best results in Figure VI.5 are obtained considering air moisture (~22.3 wt% of aggregation), this fraction drops to ~0.8 wt%

when assuming only dry entrained air in the atmosphere. This indicates that atmospheric moisture significantly contributed to ash aggregation processes for the 26th April 1979 eruption. This also highlights the model sensitivity to air moisture, especially in tropical zones.

Conclusions

On 26th April 1979, a short-lived explosive eruption occurred at La Soufrière St. Vincent volcano generating an eruptive plume that rose about 13 km above the vent. Tephra dispersal was mainly governed by a wind blowing southwards, allowing tephra samples to be collected at 33 locations from the vent up to Bequia Island at 36 km southwards. Field measurements were used to estimate ESP. A previously estimated TGSD [Brazier et al., 1982] was complemented with both the sum of two lognormal and the sum of two Weibull distributions. Starting from these three input TGSDs, we best-fitted all the available data including tephra loading, grain-size distribution and plume observations. The effect of ash aggregation was also investigated by comparing three aggregation schemes with simulations neglecting aggregation. In order to better reconstruct the main eruption features, several hundred simulations were run with aggregation under wet conditions. The optimal results obtained using the FALL3D tephra dispersal model were selected through a goodness-of-fit method. These indicate a column height of ~12 km above the vent, a mean MER of ~7.8×10^6 kg/s, and a total erupted mass of ~2.8×10^9 kg obtained for an eruption duration of 6 minutes. Best results suggest an estimation of ~22 wt% for the fine ash fraction involved in aggregation processes. This work highlights the need for further field-based aggregation studies to better characterize the aggregation processes.

Supplement

The supplement for this chapter serves for illustrating the results reported above. The supplement files are available through the following link:

http://doi.org./10.1016j.jvolgeores.2017.09.012

Figure VI.S1: Comparison of two different meteorological database resolutions (i.e. 1 and 5 km). The figure serves for illustrating the sensitivity of the resolution on the resulting tephra dispersal and deposition. It shows the discrepancies on capturing the sampled sites in terms of tephra loading. The computed differences is attributed to the resolution and is displayed by the meteorological profiles (i.e. temperature, air moisture, and wind speed).

Animation VI.A1: The time-series animation refers to the dynamic evolution of the tephra depositing from the source. The results are computed through FALL3D.

Animation VI.A2: The time-series animation corresponds to the same simulation as for Animation VI.A1, but displays the aggregate class only to show the affected areas by the aggregates in the deposit.

Acknowledgements

Chapter VII – Concluding remarks and outlook

Concluding remarks

Stating the volcanic risk (e.g. tephra loading, airborne ash dispersal), this thesis raised the necessity for improving methods to assess ESP, in particular the tephra TGSD generated by magma fragmentation. Within the TGSD, a special attention is given to the quantification of the fine and very fine ash released during basaltic explosive eruptions. Indeed, better estimating such fractions is needed to mitigate substantially the volcanic risk, especially for air traffic safety. In the introduction, we highlighted the substantial uncertainty related to the estimation of the TGSD, used as input into plume and tephra dispersal models to forecast or reconstruct numerically the tephra loading and far-travelling airborne ash dispersal. The methodology consists on integrating available data in terms of tephra loading and airborne ash mass from different instruments to characterize the TGSD from bomb-sized to very fine ash. The methodology is applied to two Etna eruptions (i.e. 23rd February and 23rd November 2013; Chapters IV and V, respectively), whose dispersal was controlled by atypical wind conditions that dispersed the plume toward the mainland.

These studies use FPlume into FALL3D model for showing the need of reconstructing the TGSD up to the very fine ash, which is used as input parameter. Regardless of the two studies, I first reconstructed the field-based TGSD. Then, to integrate the satellite retrievals of airborne ash dispersal for the 23rd February 2013 Etna eruption, I tried to extrapolate the tail of the distribution by parameterizing the field-TGSD through lognormal or Weibull distributions. The paucity of data prevents covering the missing information relative to fine and very fine ash. Considering the fail of using either the field-TGSD, lognormal or Weibull distributions within simulations for capturing the far-travelling ash dispersal, I achieved the TGSD by empirically modifying it assuming a power law decay of the tail of the TGSD to add the mass fraction of the very fine ash classes. Besides assessing ESP, such a methodology aims at reproducing simultaneously the tephra loading and airborne ash dispersal. This work is currently accepted pending revision for publication to the Journal of Geophysical Research – Solid Earth.

Analysis of the 23rd November 2013 Etna eruption, includes also weather radar retrievals, from which radar-derived GSD was estimated, for the first time for Etna's eruptions. To integrate the field- and radar-based TGSDs, I produced a weighting average integrated TGSD (field + radar) best reproducing the tephra loading. Although the integrated TGSD aims at being more realistic from bomb-sized to fine ash, the very fine ash information retrieved from satellite are not covered. The fail of reproducing any airborne ash dispersal motivated the use of the same empirical modification (as for the 23rd February 2013 eruption) to assess the whole TGSD. This methodology emerging from the synergic use of field, radar and satellite data, serves for

numerically reconstructing both the tephra loading and airborne ash dispersal. This work is in press for publication to the Journal of Atmospheric, Chemistry and Physics Discussion.

Among ESP, this thesis highlighted the benefit from integrating observational data (Chapter III) for better characterizing the eruption start and duration (e.g. seismic tremor), eruptive column height (e.g. visible and infrared images, weather radar, satellite) and ejection velocities (e.g. Doppler radar), which are then used within plume and tephra dispersal models. As described in Chapter V, numerical results were improved by modifying the simulation scheme, which consists of discretizing the eruption into a set a phases with a better estimation of the TGSD. In this scope, this study aims at encouraging further work on describing the eruption source conditions.

Regarding ash aggregation, the thesis compares different aggregation schemes and TGSDs to explore their synergic effects on tephra dispersal and deposition (Chapter VI). The methodology is applied to the well documented eruption of La Soufrière St. Vincent (West Indies) volcano, which occurred the 26th April 1979. The numerical results highlight the necessity for ash aggregation to be more thoroughly considered. Indeed, the study resulted in the non-uniqueness solution of ESPs combination that could match the main eruptive features (e.g. tephra loading). It also highlighted that depending on the fine ash enrichment of the TGSD, the outcomes indicate significant contributions of aggregates on the tephra loadings. This yields the important effect of the aggregation scheme based on (simplified or growth-based). The work of this study (Chapter VI) is published in Journal of Volcanology and Geothermal Research.

Outlook

This thesis aims at better quantifying the proportion of ash (and the sub-classes of ash) released from the volcano, and therefore the dispersal with or without ash aggregation. As overall perspective, the studies reported the broad interest of the TGSD in Volcanology, Climatology, and Natural hazard emphasizing the need for integrating data (e.g. field sampling, X-band radars, satellite, AERONET). As starting point for further investigations, the methodology presented for assessing TGSDs from different instruments could serve for future works to retrieve distribution from other sensors to converge towards the full spectrum TGSD. For instance, during explosive eruptions (e.g. Chapter IV and V), the TGSDs are missing grain-size information relative to very proximal area (i.e. < 5 km from Etna's craters), where field sampling is difficult to carry out. However, it has been demonstrated that such fraction can represent up to 70 wt% of the erupted mass [Spanu et al., 2016]. An interesting perspective would be to make the TGSD benefit from implementing the near-source L-band Doppler radar data by inverting the grain-size distribution relative to the coarser tephra (i.e. $\Phi \leq 1$). By exploring this scope, numerical simulations would expand the input TGSD up to bloc-sized tephra, providing more realistic model predictions of ash transport and fallout.

Besides coarse tephra, this thesis also reported sensitivity studies on the very fine ash (i.e. PM_{20}) measured from satellite (SEVIRI). However, SEVIRI retrievals are based on the assumption made on the partial GSD corresponding to the satellite operative grain-size window, which has a mathematical shape (lognormal). Comparative analysis between satellite measurements and model results would benefit from further studies focusing on retrieving accurately the satellite-derived GSD. Moreover, implementing such GSD within the TGSD estimation would improve the characterization of the TGSD, encouraging more sophisticated integrated approach instead of an empirical modification of the field-TGSD.

Although Volcanology and Climatology need accurate TGSD for predicting or reconstructing the eruption features through numerical investigations, the models (e.g. FALL3D) have some limitations. In particular, FALL3D has difficulties for simulating the proximal areas due to the complexities associated with the plume dynamics near the vent (e.g. < 15 km). It becomes more significant if accounting for other processes (e.g. wind coupling, latent heat, ash aggregation). In addition, the bulk computational cost for computing the tephra dispersal and deposition also limits the performance of the models. Simulations are run by means of the meteorological database describing the atmospheric fields for each time interval and vertical layer. A possibility for encompassing these limitations could be to develop an auto-adaptive mesh procedure to improve the accuracy and the computational time to run a simulation. Such a procedure was developed successfully for predicting and reconstructing the emplacement of a lava flow on the Piton de la Fournaise volcano (Reunion Island, France; Bernabeu et al. [2014]).

As final point, Chapter V of this thesis illustrated the advantage to account for all the observations provided by a wide range of instrumentation. The 23rd November 2013 Etna lava fountain showed a peculiar phenomenon by releasing a large quantity of water/gas together with the tephra, which was observable from the source up to hundreds of kilometres. The volcanic ash cloud dispersed northerly (~6 km a.s.l.), whereas the water/gas cloud spread out north-easterly (~11 km a.s.l.). Such feature was recorded from satellite but the ash component within the water/gas cloud was not quantifiable. This study highlighted the importance of being able to measure the masses of water, gas (e.g. SO_2) and ash, respectively, to prevent any substantial under-estimation of airborne ash, being potentially above the air traffic safety threshold (i.e. 2 g/m^2). The recent eruption of Agung volcano (Bali) in October 2017 also showed the presence of a large amount of water or gas released from the volcano, which may not be retrieved from satellite-based measurements. Further investigations on developing a tool capable to measure and track all the different quantities released from the volcanoes all around the world would be of high interest for modelling purposes.

Appendix

Appendix IV.A

Appendix IV.A completes Tables IV.2 and IV.4 by reporting the other parameters and models used to run the simulations.

Parameterization	Description
Eruption duration (min)	66
Vent elevation (m a.s.l.)	3200
Vent longitude (°Deg)	15.002012
Vent latitude (°Deg)	37.746548
Time step meteo data (min)	30
Longitude nodes	100
Latitude nodes	111
Altitude layers (from 0 m a.s.l., 500 m step)	10000
Eruption column model	FPlume [a]
Terminal velocity model	Ganser [b]
Vertical turbulence model	Similarity [c]
Horizontal turbulence model	CMAQ [d]
Gravity current	Yes [e]

The computational domain extension starts at 9.75 and 34.5 (Longitude/Latitude in °Deg) and ends at 40.5 and 52.5 (Longitude/Latitude in °Deg).

[a] The eruption column model uses the buoyant plume theory [Folch et al., 2016]. [b] The terminal settling velocity is calculated with the Ganser model [Ganser, 1993]. [c] The vertical component of the eddy diffusivity tensor (K_z) is estimated using the similarity option [Costa et al., 2006; Ulke, 2000]. [d] The horizontal component of the eddy diffusivity tensor (K_h) is evaluated as in Byun and Schere [2006] by the CMAQ option. [e] The gravity current effects in the umbrella region, although negligible were considered in the simulations [Costa et al., 2013; Suzuki and Koyaguchi, 2009].

Appendix IV.B

The input parameters are inverted by means of the normalized root mean square error (*RMSE*) as defined by the following:

$$RMSE_j = \sqrt{\sum_i^N w_j (Sim_i - Obs_i)^2}$$

$$w_{j=1} = \frac{1}{\sum_i^N Obs_i^2}$$

$$w_{j=2} = \frac{1}{N \times Obs_i^2}$$

where w_j refers to the weighting factor used within the *RMSE* calculation, i corresponds to the ith sample over a set of *N*. *Obs$_i$* and *Sim$_i$* are the observed and simulated tephra loadings, respectively. The weights correspond to different assumptions on the error distribution [Aitken 1935; Costa et al., 2009]. The *RMSE$_1$* is calculated with w_1 referring to a constant absolute error, whereas the *RMSE$_2$* considers a constant relative error by implying the proportional weighting factor w_2 [Folch et al., 2010; Bonasia et al., 2012; Poret et al., 2017].

Appendix V

Appendix completes Table V.2 in terms of parameterizations (i.e. parameters and models) used to run the simulations under the ARPAE and ERA-Interim meteorological databases.

Parameterization	ARPAE	ERA-Interim
Vent elevation (m a.s.l.)	3300	3300
Vent longitude (°Deg)	15.002012	15.002012
Vent latitude (°Deg)	37.746548	37.746548
Time step meteo data (min)	30	30
Longitude nodes	160	115
Latitude nodes	100	100
Grid resolution (km²)	1	5
Altitude layers (from 0 m a.s.l., 500 m step)	12000	12000
Eruption column model	FPlume [a]	FPlume [a]
Terminal velocity model	Ganser [b]	Ganser [b]
Vertical turbulence model	Similarity [c]	Similarity [c]
Horizontal turbulence model	CMAQ [d]	CMAQ [d]
Gravity current	Yes [e]	Yes [e]

[a] The eruption column model uses the buoyant plume theory [Folch et al., 2016]. [b] The terminal settling velocity is calculated through the Ganser model [Ganser, 1993]. [c] The vertical component of the eddy diffusivity tensor (Kz) is estimated using the similarity option [Costa et al., 2006; Ulke, 2000]. [d] The horizontal component of the eddy diffusivity tensor (Kh) is evaluated as in Byun and Schere [2006] by the CMAQ option. [e] The gravity current effects in the umbrella region are negligible in the far-field region, but were considered in the simulations [Costa et al., 2013; Suzuki and Koyaguchi, 2009].

Appendix VI

This section displays the others parameters and models used to run the simulations associated with the Chapter VI.

Parameters and models		
Time meteo domain	From 25/04/1979	To 28/04/1979
Grid: bottom left (Longitude / Latitude)	-61.31	-12.93
Grid: top right (Longitude / Latitude)	-61.08	13.40
Time step meteo data (min)	—	30
Grid nodes: (Longitude / Latitude)	70	101
Altitude layers (500 m step)	0	14500
Vent coordinates: (Longitude / Latitude)	-61.180743	13.333557
Vent elevation (m)	—	1220
Eruption duration (sec)	—	370
Eruption column model	—	FPlume [a]
Terminal velocity model	—	Ganser [b]
Vertical turbulence model	—	Similarity [c]
Horizontal turbulence model	—	RAMS [d]
RAMS C_s	—	0.3
Wet deposition	—	No

[a] The eruption column model used is based on the BPT as described in Folch et al. [2016]. [b] The semi-empirical parameterization for the terminal settling velocity calculation is done through the Ganser option as described in Ganser [1993]. [c] The vertical component of the eddy diffusivity tensor, Kz, is estimated using the Similarity option as in Costa et al. [2006] and Ulke [2000]. [d] The horizontal component of the eddy diffusivity tensor, Kh, is evaluated as in Pielke et al. [1992] by the RAMS option.

References

Aida, I. (1978). Reliability of a tsunami source model derived from fault parameters. *J. Phys. Earth*, 26, 57–73

Aitken, A.C. (1935). On least squares and linear combinations of observations. *Proc. R. Soc. Edinb.* 55, 42–48

Allard, P., Burton, M., and Murè, F. (2005). Spectroscopic evidence for a lava fountain driven by previously accumulated magmatic gas. *Nature* 433, 407–410

Alparone, S., Andronico, D., Lodato, L., and Sgroi, T. (2003). Relationship between tremor and volcanic activity during the Southeast Crater eruption on Mount Etna in early 2000. *J. Geophys. Res.*, 108, B5, 2241. doi:10.1029/2002JB001866

Anderson, K., and Segall, P. (2013). Bayesian inversion of data from effusive volcanic eruptions using physics-based models: Application to Mount St. Helens 2004-2008. *J. Geophys. Res. – Solid Earth* 118, 2017–2037. doi:10.1002/jgrb.50169

Andronico, D., Cristaldi, A., and Scollo, S. (2008a). The 4–5 September 2007 lava fountain at South-East Crater of Mt. Etna, Italy. *J. Volcanol. Geotherm. Res.*, 173:325–328

Andronico, D., Scollo, S., Cristaldi, A., and Caruso, S. (2008b). The 2002–03 Etna explosive activity: tephra dispersal and features of the deposit. *J. Geophys. Res.* 113:B04209. doi:10.1029/2007JB005126

Andronico, D., Scollo, S., Cristaldi, A., and Lo Castro, M.D. (2014a). Representivity of incompletely sampled fall deposits in estimating eruption source parameters: a test using the 12–13 January 2011 lava fountain deposit from Mt. Etna volcano, Italy. *Bull. Volcanol.* 76 (861). doi:10.1007/s00445-014-0861-3

Andronico, D., Scollo, S., Lo Castro, M.D., Cristaldi, A., Lodato, L., and Taddeucci, J. (2014b). Eruption dynamics and tephra dispersal from the 24 November 2006 paroxysm at South-East Crater, Mt. Etna, Italy. *J. Volcanol. Geotherm. Res.* 274, 78–91. doi:10.1016/j.jvolgeores.2014.01.009

Andronico, D., Scollo, S., and Cristaldi, A. (2015). Unexpected hazards from tephra fallouts at Mt. Etna: The 23 November 2013 lava fountain. *J. Volcanol. Geotherm. Res.* 304, 118-125. doi:10.1016/j.jvolgeores.2015.08.007

Andronico, D., and Del Carlo, P. (2016). PM10 measurements in urban settlements after lava fountain episodes at Mt. Etna, Italy: Pilot test to assess volcanic ash hazard on human health. *Nat. Hazards Earth Syst. Sci.* 16, 29–40

Armienti, P., Macedonio, G., and Pareschi, M.T. (1988). A numerical model for simulation of Tephra transport and deposition: Applications to May 18, 1980, Mount St. Helens eruption. *J. Geophys. Res.* 93, B6, 6463–6476

Ayris, P.M., and Delmelle, P. (2012). The immediate environmental effects of tephra emission. *Bull. Volcanol.* 74, 1905–1936

Azzopardi, F., Ellul, R., Prestifilippo, M., Scollo, S., and Coltelli, M. (2013). The effect on Etna volcanic ash clouds on the Maltese Islands. *J. Volcanol. Geotherm. Res.* 260, 13–26

Bagheri, G., and Bonadonna, C. (2016). On the drag of freely falling non-spherical particles. *Powder Technology*, 301, 526–544. doi:10.1016/j.powtec.2016.06.015

References

Barsotti, S., Neri, A., and Scire, J. (2008). The VOL-CALPUFF model for atmospheric ash dispersal. I. Approach and physical formulation. *J. Geophys. Res.* 113 (B03208). doi:10.1029/2006JB004623

Barsotti, S., Andronico, D., Neri, A., Del Carlo, P., Baxter, P. J., Aspinall, W. P., and Hincks, T. (2010). Quantitative assessment of volcanic ash hazards for health and infrastructure at Mt. Etna (Italy) by numerical simulation. *J. Volcanol. Geotherm. Res.* 192, 85–96. doi:10.1016/j.jvolgeores.2010.02.011

Beckett, F.M., Witham, C.S., Hort, M.C., Stevenson, J.A., Bonadonna, C., and Millington, S.C. (2014). The sensitivity of NAME forecasts of the transport of volcanic ash clouds to the physical characteristics assigned to the particles. Met Office, *Forecasting Research*, Technical report n°592

Beckett, F.M., Witham, C.S., Hort, M.C., Stevenson, J.A., Bonadonna, C., and Millington, S.C. (2015). Sensitivity of dispersion model forecasts of volcanic ash clouds to the physical characteristics of the particles, *J. Geophys. Res. – Atmos.*, 120. doi:10.1002/2015JD023609

Behncke, B., Branca, S., Corsaro, R.A., De Beni, E., Miraglia, L., and Proietti, P. (2014). The 2011–2012 summit activity of Mount Etna: birth, growth and products of the new SE crater. *J. Volcanol. Geotherm. Res.* 270, 10–21

Bernabeu, N., Saramito, P., and Smutek, C. (2014). A new shallow approximation for tridimensional non-isothermal viscoplastic lava flows. hal-01059334

Bey, I., Jacob, D.J., Yantosca, R.M., Logan, J.A., Field, B.D., Fiore, A.M., Li, Q., Liu, H.Y., Mickley, L.J., and Schultz, M.G. (2001). Global modelling of tropospheric chemistry with assimilated meteorology: model description and evaluation. *J. Geophys. Res.* 106 (D19), 23073–23096

Boichu, M., Chiapello, A., Brogniez, C., Péré, J.C., Thieuleux, F., Torres, B., Blarel, L., Mortier, A., Podvin, T., Goloub, P., Söhne, N., Clarisse, L., Bauduin, S., Hendrick, F., Theys, N., Van Roozendael, M., and Tanré, D. (2016). Tracking far-range air pollution induced by the 2014-15 Bardarbunga fissure eruption (Iceland). *Atmos. Chem. Phys. Discuss.* doi:10.5194/acp-2016-159

Bonaccorso, A., Calvari, S., Linde, A., and Sacks, S (2014). Eruptive processes leading to the most explosive lava fountain at Etna volcano: The 23 November 2013 episode, *Geophys. Res. Lett.*, 41, 4912–4919. doi:10.1002/2014GL060623

Bonadonna, C., Macedonio, G., and Sparks, R.S.J. (2002). Numerical modelling of tephra fallout associated with dome collapses and Vulcanian explosions: application to hazard assessment on Montserrat. *Geological Society*, London, Memoirs, 21, 517–537

Bonadonna, C., and Phillips, J.C. (2003). Sedimentation from strong volcanic plumes. *J. Geophys. Res.* 108, B7, 2340. doi:10.1029/2002JB002034

Bonadonna, C., and Houghton, B.F. (2005). Total grain-size distribution and volume of tephra-fall deposits. *Bull. Volcanol.* 67, 441–456. doi:10.1007/s00445-004-0386-2

Bonadonna, C., Connor, C.B., Houghton, B., Connor, L., Byrne, M., Laing, A., and Hincks, T.K. (2005). Probabilistic modelling of tephra dispersal: Hazard assessment of a multiphase rhyolitic eruption at Tararewa, New Zealand. *J. Geophys. Res.* 110, B03203. doi:10.1029/2003JB002896

Bonadonna, C, Genco, R, Gouhier, M, Pistolesi, M, Cioni, R, Alfano, F, Hoskuldsson, A, and Ripepe, M. (2011). Tephra sedimentation during the 2010 Eyjafjallajokull eruption (Iceland) from deposit, radar, and satellite observations. *J. Geophys. Res. – Solid Earth.* doi*:*10.1029/2011JB008462

References

Bonadonna, C., Folch, A., Loughlin, S., and Puempel, H. (2012). Future developments in modelling and monitoring of volcanic ash clouds: outcomes from the first IAVCEI-WMO workshop on ash dispersal forecast and civil aviation. *Bull. Volcanol.* 74, 1–10

Bonadonna, C., and Costa, A. (2012). Estimating the volume of tephra deposits: a new simple strategy. *Geology* 40, 415–418. doi:10.1130/G32769.1

Bonadonna, C., and Costa, A. (2013). Plume height, volume, and classification of explosive volcanic eruptions based on the Weibull function. *Bull. Volcanol.* 75 (8), 742. doi:10.1007/s00445-013-0742-1

Bonadonna, C., Cioni, R., Pistolesi, M., Elissondo, M., and Baumann, V. (2015a). Sedimentation of long-lasting wind-affected volcanic plumes: the example of the 2011 rhyolitic Codon Caulle eruption, Chile. *Bull. Volcanol.* 77:13. doi:10.1007/s00445-015-0900-8

Bonadonna, C., Pistolesi, M., Cioni, R., Degruyter, W., Elissondo, V., and Baumann, V. (2015b). Dynamics of wind-affected volcanic plumes: The example of the 2011 Cordon Caulle eruption, Chile. *J. Geophys. Res – Solid Earth* 120, 2242–2261. doi:10.1002/2014JB011478

Bonadonna, C., Biass, S., and Costa, A. (2015c). Physical characterization of explosive volcanic eruptions based on tephra deposits: propagation of uncertainties and sensitivity analysis. *J. Volcanol. Geotherm. Res.* 296, 80–100. doi:10.1016/j.jvolgeores.2015.03.009

Bonasia, R., Macedonio, G., Costa, A., Mele, D., and Sulpizio, R. (2010). Numerical inversion and analysis of tephra fallout deposits from the 472 AD sub-Plinian eruption at Vesuvius (Italy) through a new best-fit procedure. *J. Volcanol. Geotherm. Res.* 189, 238–246. doi:10.1016/j.jvolgeores.2009.11.009

Bonasia, R., Costa, A., Folch, A., Macedonio, G., and Capra, L. (2012). Numerical simulation of tephra transport and deposition of the 1982 El Chichón eruption and implications for hazard assessment. *J. Volcanol. Geotherm. Res.* 231–232, 39–49. doi:10.1016/j.jvolgeores.2012.04.006

Boutahar, J., Lacour, S., Mallet, V., Quélo, D., Roustan, Y., and Sportisse, B. (2004). Development and validation of a fully modular platform for numerical modelling of air pollution: Polair3D. *Int. J. Env. Poll.* 22, 17–28

Brazier, S., Davis, A.N., Sigurdsson, H., and Sparks, R.S.J. (1982). Fall-out and deposition of volcanic ash during the 1979 explosive eruption of the Soufriere of St. Vincent. *J. Volcanol. Geotherm. Res.* 14, 3-4, 335-359. doi:10.1016/0377-0273(82)90069-5

Brazier, S., Sparks, R.S.J., Carey, S.N., Sigurdsson, H., and Westgate, J.A. (1983). Bimodal distribution and secondary thickening in air-fall ash layers. *Nature* 301

Brown, R.J., Bonadonna, C., and Durant, A.J. (2012). A Review of Volcanic Ash Aggregation. *Physics and Chemistry of the Earth*, parts A/B/C, 45–46, 65–78. doi:10.1016/j.pce.2011.11.001

Bursik, M.I., Sparks, R.S.J., Gilbert, J.S., and Carey S.N. (1992). Sedimentation of tephra by volcanic plumes. I – Theory and its comparison with a study of the Fogo A Plinian deposit, Sao Miguel (Azores). *Bull. Volcanol.* 54, 329–344

Bursik, M. (2001). Effect of wind on the rise height of volcanic plumes. *Geophys. Res. Lett.*, 28, 3621–3624. doi:10.1029/2001GL013393

References

Byun, D., and Schere, K. L. (2006). Review of the governing equations, computational algorithms, and other components of the Models-3 Community Multiscale Air Quality (CMAQ) modelling system. *Applied Mechanics Reviews* 59, 51-77. doi:10.1115/1.2128636

Carbone, D., Zuccarello, L., Messina, A., Scollo, S., and Rymer, H. (2015). Balancing bulk gas accumulation and gas output before and during lava fountaining episodes at Mt. Etna. *Nature – Sci. Rep.* 5, 18049. doi:10.1038/srep18049

Carey, S.N., and Sparks, R.S.J. (1986). Quantitative models of the fallout and dispersal of tephra from volcanic eruption columns. *Bull. Volcanol.* 48, 109–125

Casadevall, T.J. (1994). Volcanic ash and aviation safety. Proceedings of the First International Symposium on Volcanic Ash and Aviation Safety. *USGS Bull.* 2047, p. 450

Casadevall, T.J., Thompson, T.B., and Fox, T. (1999). World Map of Volcanoes and Principal Aeronautical Features. *USGS Map* I-2700, scale 1:34,268,000, reprinted 2001

Cerminara, M., Esposti Ongaro, T., and Neri, A. (2016). Large eddy simulation of gos-particle kinematic decoupling and turbulent entrainment in volcanic plumes. *J. Volcanol. Geotherm. Res.* 326, 143–171. doi:10.1016/j.jvolgeores.2016.06.018

Chan, K.L., and Chan, K.L. (2017). Aerosol optical depths and their contributing sources in Taiwan. J. *Atmos. Env.* 148, 364-375. doi:10.1016/j.atmosenv.2016.11.011

Chhabra, R.P., Agarwall, L., and Sinha, N.K. (1999). Drag on non-spherical particles: an evaluation of available methods. *Powder Technology* 101 (3), 288–295

Cigala, V., Kueppers, U., Peña Fernández, J.J., Taddeucci, J., Sesterhenn, J., and Dingwell, D.B. (2017). The dynamics of volcanic jets: Temporal evolution of particles exit velocity from shock-tube experiments. *J. Geophys. Res. – Solid Earth* 122. doi:10.1002/2017JB014149

Connor, C., Hill, B., Winfrey, B., Franklin, M., and La Femina, P. (2001). Estimation of volcanic hazards from tephra fallout. *Natural Hazards Review* 2, 33–42

Connor, L.J., and Connor, C.B. (2005). Inversion is the key to dispersion: understanding eruption dynamics by inverting tephra fallout. Statistics in volcanology. *Geological Society*, London, 231–242

Cornell, W., Carey, S., and Sigurdsson, H. (1983). Computer simulation of transport and deposition of Campanian Y-5 ash. *J. Volcanol. Geotherm. Res.* 17, 89–109. doi:10.1016/0377-0273(83)90063-X

Corradini, S., Spinetti, C., Carboni, E., Tirelli, C., Buongiorno, M.F., Pugnaghi, S., and Gangale, G. (2008). Mt. Etna tropospheric ash retrieval and sensitivity analysis using Moderate Resolution Imaging Spectroradiometer measurements. *J. Applied Remote Sens.* 2, 023550. doi:10.1117/1.3046674

Corradini, S., Montopoli, M., Guerrieri, L., Ricci, M., Scollo, S., Merucci, L., Marzano, F. S., Pugnaghi, S., Prestifilippo, M., Ventress, L., Grainger, R. G., Carboni, E., Vulpiani, G., and Coltelli, M. (2016). A multi-sensor approach for the volcanic ash cloud retrievals and eruption characterization. *Remote Sensing*, Special Issue on Volcano Remote Sensing 8(1), 58. doi:10.3390/rs8010058

Corsaro, R.A., and Miraglia, L., 2013a. Composizione dei vetri dei prodotti emessi dal Nuovo Cratere di Sud-Est durante le fontane di lava del 23 e 28 febbraio 2013, *INGV Report*, at http://www.ct.ingv.it/it/rapporti/vulcanologia.html?view=docman

References

Corsaro, R.A., and Miraglia, L., 2013b. Composizione dei vetri dei prodotti emessi dal Nuovo Cratere di Sud-Est durante la fontana di lava del 23 novembre 2013, *INGV Report*, at http://www.ct.ingv.it/it/rapporti/vulcanologia.html?view=docman

Corsaro, R.A., Andronico, D., Behncke, B., Branca, S., De Beni, E., Caltabiano, T., Ciancitto, F., Cristaldi, A., La Spina, A., Lodato, L., Giammanco, S., Miraglia, L., Neri, M., Salerno, G., Scollo, S., and Spada, G. (2017). Monitoring the December 2015 summit eruptions of Mt. Etna (Italy): implications on eruptive dynamics. *J. Volcanol. Geotherm. Res.* 341, 53–69. doi:10.1016/j.jvolgeores.2017.04.018

Costa, A., Macedonio, G., and Folch, A. (2006). A three-dimensional Eulerian model for transport and deposition of volcanic ashes. *Earth Planet. Sci. Lett.* 241, 634–647. doi:10.1016/j.epsl.2005.11.019

Costa, A., Dell'Erba, F., Di Vito, M.A., Isaia, R., Macedonio, G., Orsi, G., and Pfeiffer, T. (2009). Tephra fallout hazard assessment at the Campi Flegrei caldera (Italy). *Bull. Volcanol.* 71:259-273. doi:10.1007/s00445-008-0220-3

Costa, A., Folch, A., and Macedonio, G. (2010). A model for wet aggregation of ash particles in volcanic plumes and clouds: 1. Theoretical formulation. *J. Geophys. Res.* 115, B09201. doi:10.1029/2009JB007175

Costa, A., Folch, A., Macedonio, G., Giaccio, B., Isaia, R., and Smith, V. C. (2012). Quantifying volcanic ash dispersal and impact from Campanian Ignimbrite super-eruption. *Geophys. Res. Lett.* 39. doi:10.1029/2012GL051605

Costa, A., Folch, A., and Macedonio, G. (2013). Density-driven transport in the umbrella region of volcanic clouds: implications for tephra dispersion models. *Geophys. Res. Lett.* 40, 4823–4827. doi:10.1002/grl.50942

Costa, A., Smith, V.C., Macedonio, G., and Matthews, N.E. (2014). The magnitude and impact of the Youngest Toba Tuff super-eruption. *Frontiers in Earth Sci.* 2, 16. doi:10.3389/feart.2014.00016

Costa, A., Pioli, L., and Bonadonna, C. (2016a). Assessing tephra total grain-size distribution: Insights from field data analysis. *Earth and Planetary Sci. Lett.* 443, 90–107

Costa, A., Suzuki, Y.J., Cerminara, M., Devenish, B., Esposti Ongaro, T., Herzog, M., Van Eaton, A., Denby, L.C., Bursik, M., de Michieli Vitturi, M., Engwell, S., Neri, A., Barsotti, S., Folch, A., Macedonio, G., Girault, F., Carazzo, G., Tait, S., Kaminski, E., Mastin, L., Woodhouse, M., Phillips, J.C., Hogg, A.J., Degruyter, W.J., and Bonadonna, C. (2016b). Results of the eruption column model inter-comparison study, *J. Volcanol. Geotherm. Res.* 326. doi:10.1016/j.jvolgeores.2016.01.017

Costa, A., Pioli, L., and Bonadonna, C. (2017). Corrigendum to "Assessing tephra total grain-size distribution: Insights from field data analysis". [*Earth and Planetary Sci. Lett.* 443, 90-107, 2016]; *Earth and Planetary Sci. Lett.* doi:10.1016/j.epsl.2017.03.003

Crompton, E., and Husson, P. (2015). Volcanic Ash Advisories: how the VAACs use the 'Discernible Ash' definition to draw their lines now and in the future, *7th International Workshop on Volcanic Ash (IWVA/7)*, Anchorage (Alaska), USA, 19–23 October. https://www.wmo.int/aemp/sites/default/files/P-09_Crompton-Husson.pdf

D'Amours, R., and Malo, A. (2004). A zero[th] order Lagrangian particle dispersion model MLDP0. *Internal Publication, Canadian Meteorological Center, Environmental Emergency Response Section*, Dorval, QC, Canada, 19

References

Dacre, H.F., Grant, A.L.M., Hogan, R.J., Belcher, S.E., Thomson, D.J., Devenish, B.J., Marenco, F., Hort, M.C., Haywood, J.M., Ansmann, A., Mattis, I., and Clarisse, L. (2011). Evaluating the structure and magnitude of the ash plume during the initial phase of the 2010 Eyjafjallajökull eruption using lidar observations and Name simulations. *J. Geophys. Res.* 116, D00U03. doi:10.1029/2011JD015608

De Beni, E., Behncke, B., Branca, S., Nicolosi, I., Carluccio, R., D'Ajello Caracciolo, F., and Chiappini, M. (2015). The continuing story of Etna's New Southeast Crater (2012-2014): Evolution and volume calculations based on field surveys and aerophotogrammetry. *J. Volcanol. Geotherm. Res.* 303, 175–186. doi:10.1016/j.jvolgeores.2015.07.021

Degruyter, W., and Bonadonna, C. (2012). Improving on mass flow rate estimates of volcanic eruptions. *Geophys. Res. Lett.* 39, L16308. doi:10.1029/2012GL052566

Del Bello, E., Taddeucci, J., Scarlato, P., Giacalone, E., and Cesaroni, C. (2015). Experimental investigation of the aggregation-disaggregation of colliding volcanic ash particles in turbulent, low-humidity suspensions. *Geophys. Res. Lett.* 42, 1068–1075. doi:10.1002/2014GL062292

Del Bello, E., Taddeucci, J., de' Michieli Vitturi, M., Scarlato, P., Andronico, D., Scollo, S., Kueppers, U., and Ricci, T. (2017). Effect of particle volume fraction on the settling velocity of volcanic ash particles: insights from joint experimental and numerical simulations. *Nature – Sci. Rep.* 6:39620. doi:10.1038/srep39620

Dellino, P., and Kyriakopoulos, K. (2003). Phreatomagmatic ash from the ongoing eruption of Etna reaching the Greek island of Cefalonia. *J. Volcanol. Geotherm. Res.* 126, 3-4, 341–345. doi:10.1016/S0377-0273(03)00154-9

Devenish, B.J., Rooney, G.G., Webster, H.N., and Thomson, D.J. (2010). The entrainment rate for buoyant plumes in a crossflow, *Boundary-Layer Meteorol.* 134, 411–439. doi:10.1007/s10546-009-9464-5

Dingwell, D.B. (1996). Volcanic dilemma: Flow or blow? *Science*, 273, 1054–1055

Donnadieu F., Freville P., Rivet S., Hervier C., and Cacault P. (2015). The Volcano Doppler radar data base of Etna (VOLDORAD 2B). Université Clermont Auvergne – CNRS. http://wwwobs.univ-bpclermont.fr/SO/televolc/voldorad/bddtr.php. doi:10.18145/VOLDORAD.ETNA.2009, 2015.

Donnadieu F., Freville P., Hervier C., Coltelli M., Scollo S., Prestifilipo M., Valade S., Rivet S., and Cacault P. (2016). Near-source Doppler radar monitoring of tephra plumes at Etna. *J. Volcanol. Geotherm. Res.* 312, 26–39, 2016.

Donnadieu, F., Freret-Lorgeril, V., Coltelli, M., Scollo, S., Gouhier, M., Fréville, P., Hervier, C., and Prestifilippo, M. (2017) Lava fountaining paroxysms generating tephra plumes at Mt. Etna: Remote sensing retrievals, *IAVCEI meeting*, Portland, 14-18 August 2017, USA, Poster VO43A-139

Draxler, R.R., and Hess, G.D. (1998). An overview of the Hysplit_4 modelling system of trajectories, dispersion, and deposition. *Australian Meteorological Magazine* 47, 295–308

Dubovik, O., and King, M. D. (2000). A flexible inversion algorithm for retrieval of aerosol optical properties from Sun and sky radiance measurements. *J. Geophys. Res.* 105, 20, 673–20, 696

Dubovik, O., Smirnov, A., Holben, B.N., King, M.D., Kaufman, Y. J., Eck, T.F., and Slutsker, I. (2000). Accuracy assessment of aerosol optical properties retrieval from AERONET sun and sky radiance measurements. *J. Geophys. Res.* 105, 9791–9806

References

Dubovik, O. (2004). Optimization of Numerical Inversion in Photopolarimetric Remote Sensing. Photopolarimetry in *Remote Sensing* [G. Videen, Y. Yatskiv and M. Mish-chenko, Eds.], Kluwer Academic Publishers, Dordrecht, Netherlands, 65–106

Dubovik, O., Sinyuk, A., Lapyonok, T., Holben, B.N., Mishchenko, M., Yang, P., Eck, T.F., Volten, H., Muñoz, O., Veihelmann, B., van der Zande, W.J., Leon, J.F., Sorokin, M., and Slutsker, I. (2006). Application of spheroid models to account for aerosol particle nonsphericity in remote sensing of desert dust. *J. Geophys. Res.* 111, D11208. doi:10.1029/2005JD006619

Durant, A.J., Rose, W.I., Sarna-Wojcicki, A.M., Carey, S., and Volentik, A.C.M. (2009). Hydrometeor-enhanced tephra sedimentation: Constraints from the 18 May 1980 eruption of Mount St. Helens. *J. Geophys. Res.* 114, B03204. doi:10.1029/2008JB005756

Esposti Ongaro, T., Cavazzoni, C., Erbacci, G., Neri, A., and Salvetti, M.V. (2007). A parallel multiphase flow code for the 3D simulation of explosive volcanic eruptions. *Parallel Computing* 541–560

Fairlie, T.D., Jacob, D.J., and Park, R.J. (2007). The impact of transpacific transport of mineral dust in the United States. *J. Atmos. Env.* 41, 1251-1266. doi:10.1016/j.atmosenv.2006.09.048

FALL3D website: http://datasim.ov.ingv.it/models/fall3d.html

Feng, J. (2008). A size-resolved model and a four-mode parameterization of dry deposition of atmospheric aerosols. *J. Geophys. Res.* 113, D12201. doi:10.1029/2007JD009004

Folch, A., Cavazzoni, C., Costa, A., and Macedonio, G. (2008). An automatic procedure to forecast tephra fallout. *J. Volcanol. Geophys. Res.* 177, 767–777

Folch, A., Costa, A., and Macedonio, G. (2009). FALL3D: A computational model for transport and deposition of volcanic ash. *Comp. Geosci.* 35, 1334–1342. doi:10.1016/j.cageo.2008.08.008

Folch, A., Costa, A., Durant, A., and Macedonio, G. (2010). A model for wet aggregation of ash particles in volcanic plumes and clouds: 2. Model application. *J. Geophys. Res.* 115, B09202. doi:10.1029/2009JB007176

Folch, A. (2012). A review of tephra transport and dispersal models: Evolution, current status, and future perspectives. *J. Volcanol. Geotherm. Res.* 235–236, 96–115. doi:10.1016/j.volgeores.2012.05.020

Folch, A., Costa, A., and Basart, S. (2012). Validation of the FALL3D ash dispersion model using observations of the 2010 Eyjafjallajökull volcanic ash clouds. *Atmos. Env.* 48, 165–183. doi:10.1016/j.atmosenv.2011.06.072

Folch, A., Mingari, L., Osores, M. S., and Collini, E. (2014). Modelling volcanic ash resuspension - application to the 14-18 October 2011 outbreak episode in Central Patagonia, Argentina. *Nat. Hazards Earth Syst. Sci.* 14, 119–133. doi:10.5194/nhess-14-119-2014

Folch, A., Costa, A., and Macedonio, G. (2016). FPLUME-1.0: An integral volcanic plume model accounting for ash aggregation. *Geosci. Model Dev.* 9, 431–450. doi:10.5194/gmd-9-431-2016

Freret-Lorgeril, V., Donnadieu, F., Coltelli, M., Scollo, S., Fréville, P., Hervier, C., and Prestifilippo, M. (2016). Doppler radar retrievals from lava fountaining paroxysms generating tephra plumes at Mt. Etna. *EGU General Assembly*, Vienna, 23-28 April, Poster

References

Ganser, G.H. (1993). A rational approach to drag prediction of spherical and non-spherical particles. *Powder Technol.* 77, 143–152. doi:10.1016/0032-5910(93)80051-B

Gouhier, M., Harris, A., Calvari, S., Labazuy, P., Guéhenneux, Y., Donnadieu, F., and Valade, S. (2012). Lava discharge during Etna's January 2011 fountain tracked using MSG-SEVIRI. *Bull. Volcanol.* 74, 787–793. doi:10.1007/s00445-011-0572-y

Gouhier, M., Guéhenneux, Y., Labazuy, P., Cacault, P., Decriem, J., and Rivet, S. (2016). HOTVOLC: a web-based monitoring system for volcanic hot spots. *Geological Society*, London, Special Publications, 426, SP426-31

Grindle, T.J., and Burcham, F.W.J. (2003). Engine Damage to a NASA DC-8-72 Airplane From a High-Altitude Encounter With a Diffuse Volcanic Ash Cloud. *Technical Report* NASA/TM-2003-212030, NASA Dryden Flight Research Center, Edwards, California

Guéhenneux, Y., Gouhier, M., and Labazuy, P. (2015). Improved space borne detection of volcanic ash for real-time monitoring using 3-Band method. *J. Volcanol. Geotherm. Res.* 293, 25–45

Guffanti, M., Ewert, J.W., Gallina, G.M., Bluth, G.J.S., Swanson, G.L. (2005). Volcanic-ash hazard to aviation during the 2003-2004 eruption activity of Anatahan volcano Commonwealth of the Northern Mariana Islands. *J. Volcanol. Geotherm. Res.* 146, 241–255, doi:10.1016/j.volgeores.2004.12.011

Guffanti, M., Mayberry, G.C., Casadevall, T.J., and Wunderman, R. (2009). Volcanic hazards to airports. *Nat. Hazards*. doi:10.1007/s11069-008-9254-2

Guffanti, M., Casadevall, T.J., and Budding, K. (2010). Encounters of Aircraft with Volcanic Ash Clouds: A Compilation of Known Incidents, 1953-2009. *U.S. Geological Survey Data Series 545*, ver. 1.0, 12 p., plus 4 appendixes including the compilation database, available only at http://pubs.usgs.gov/ds/545.

Heath, E., Macdonald, R., Belkin, H., Hawkesworth, C., and Sigurdsson, H. (1998). Magmagenesis at Soufriere Volcano, St. Vincent, Lesser Antilles Arc. *J. Petrology* 39, 10, 1721–1764

Herzog, M., and Graf, H.F. (2010). Applying the three-dimensional model ATHAM to volcanic plumes: Dynamic of large co-ignimbrite eruptions and associated injection heights for volcanic gases. *Geophys. Res Lett.* 37, L19807. doi:10.1029/2010GL044986

Holben, B.N., Eck, T.F., Slutsker, I., Tanré, D., Buis, J.P., Setzer, A., Vermote, E., Reagan, J.A., Kaufman, Y.J., Nakajima, T., Lavenu, F., Jankowiak, I., and Smirnov, A. (1998). AERONET – A Federated Instrument Network and Data Archive for Aerosol Characterization. *Remote Sens. Env.* 66, 1–16

Holben, B.N., Eck, T.F., Slutsker, I., Smirnov, A., Sinyuk, A., Schafer, J., Giles, D., and Dubovik, O. (2006). Aeronet's Version 2.0 quality assurance criteria, Proc. SPIE 6408, *Remote Sensing of the Atmosphere and Clouds*, 64080Q. doi:10.1117/12.706524

Horwell, C.J. (2007). Grain size analysis of volcanic ash for the rapid assessment of respiratory health hazard. *J. Environ. Monit*. 9, 1107–1115

Horwell, C.J., Baxter, P.J., Hillman, S.E., Calkins, J.A., Damby, D.E., Delmelle, P., Donaldson, K., Dunster, C., Fubini, B., Kelly, F.J., Le Blond, J.S., Livi, K.J.T., Murphy, F., Nattrass, C., Sweeney, S., Tetley, T.D., Thordarson, T. and Tomatis, M. (2013). Physicochemical and toxicological profiling of ash from the 2010 and 2011 eruptions of Eyjafjallajökull and Grímsvötn volcanoes, Iceland using a rapid respiratory hazard assessment protocol. *Environ. Res*. 127, 63–73

References

Horwell, C.J., Sargent, P., Andronico, D., Lo Castro, M.D., Tomatis, M., Hillman, S.E., Michnowicz, S.A.K., and Fubini, B. (2017). The iron-catalysed surface reactivity and health-pertinent physical characteristics of explosive volcanic ash from Mt. Etna, Italy. *J. Appl. Volcanol.* doi:10.1186/s13617-017-0063-8

HOTVOLC Website: http://hotvolc.opgc.fr

Hurst, A.W., and Turner, R. (1999). Performance of the program ASHFALL for forecasting ashfall during the 1995 and 1996 eruptions of Ruapehu volcano. *New Zealand J. Geol. and Geophys.* 42, 615–622

Hurst, T., and Smith, W. (2004). A Monte Carlo methodology for modelling ashfall hazards. *J. Volcanol. Geotherm. Res.* 138, 393–403. doi:10.1016/j.volgeores.2004.08.001

INGV – OE Website: http://www.ct.ingv.it/it/tremore-vulcanico.html

Iwasaki, T., Maki, T., and Takayama, K. (1998). Tracer transport model at Japan Meteorological Agency and its application to the ETEX data. *Atmos. Env.* 32, 24, 4285–4295

Jarvis, A., Reuter, H.I., Nelson, A., and Guevara, E. (2008). Hole-filled seamless SRTM data V4 *International Centre for Tropical Agriculture*, available from http://srtm.csi.cgiar.org

Jones, A.R., Thomson, D.J., Hort, M., and Devenish, B. (2007). The U.K. Met Office's next-generation atmospheric dispersion model, NAME III. [In: Borrego, C., Norman, A.L. (Eds), Air Pollution Modelling and its Application XVII (Proceedings of the 27th *NATO/CCMS Int. Technical Meeting* on Air Pollution Modelling and its Application. Springer, 580–589

Kaminski, E., Tait, S., and Carazzo, G. (2005). Turbulent entrainment in jets with arbitrary buoyancy. *J. Fluid Mech.* 526, 361–376. doi:10.1017/S0022112004003209

Kravitz, B., Robock, A., and Bourassa, A. (2010). Negligible climatic effects from the 2008 Okmok and Kasatochi volcanic eruptions. *J. Geophys. Res.* 115, D00L05. doi:10.1029/2009JD013525

Krumbein, W.C. (1934). Size frequency distributions of sediments. *J. Sediment. Res.* 4, 65–67

Langmann, B. (2000). Numerical modelling of regional scale transport and photochemistry directly together with meteorological processes. *Atmos. Env.* 34, 3585–3598

Lecointre, J., Hodgson, K., Neall, V., Cronin, S. (2004). Lahar-triggering mechanisms and hazard at Ruapehu volcano, New Zealand. *Nat. Hazards* 31 (1), 85–109

Lo Castro, M.D., and Andronico, D. (2008). Operazioni di base per la misura della distribuzione granulometrica di particelle vulcaniche tramite il CAMSIZER. *Rapporti Tecnici INGV* 79, 1–35

Macedonio, G., Costa, A., and Longo, A. (2005). A computer model for volcanic ash fallout and assessment of subsequent hazards. *Computer and Geosciences* 31, 837–845

Macedonio, G., and Costa, A. (2012). Brief Communication "Rain effect on the load of tephra deposits". *Nat. Hazards Earth Syst. Sci.* 12, 1229–1233. doi:10.5194/nhess-12-1229-2012

Macedonio, G., Costa, A., Scollo, S., and Neri, A. (2016). Effects of eruption source parameter variation and meteorological dataset on tephra fallout hazard assessment: example from Vesuvius (Italy). *J. Applied Volcanol.* 5:5. doi:10.1186/s13617-016-0045-2

References

Manzella, I., Bonadonna, C., Phillips, J.C., and Monnard, H. (2015). The role of gravitational instabilities in deposition of volcanic ash. *Geology*, 43, 3, 211–214. doi:10.1130/G36252.1

Marenco, F., Johnson, B., Turnbull, K., Newman, S., Haywood, J., Webster, H., and Ricketts, H. (2011). Airborne lidar observations of the 2010 Eyjafjallajökull volcanic ash plume. *J. Geophys. Res.* 116, D00U05. doi:10.1029/2011JD016396

Martet, M., Peuch, V.H., Laurent, B., Martícorena, B., and Bergametti, G. (2009). Evaluation of long-range transport and deposition of desert dust with the CTM MOCAGE. *Tellus* 61B, 449–463. doi:10.1111/j.16..-0889.2008.00413.x

Martí, A., Folch, A., Costa, A., and Engwell, S. (2016). Reconstructing the Plinian and co-ignimbrite sources of large volcanic eruptions: A novel approach for the Campanian Ignimbrite. *Nature comm. – Sci. Rep.* 6, 21220. doi:10.1038/srep21220

Maryon, R.H., Ryall, D.B., and Malcolm, A.L. (1999). The NAME 4 Dispersion Model: - Science Documentation. *Turbulence and Diffusion* Note N° 262, Met Office

Mastin, L.G., Guffanti, M., Servranckx, R., Webley, P., Barsotti, S., Dean, K., Durant, A., Ewert, J. W., Neri, A., Rose, W.I., Schneider, D., Siebert, L., Stunder, B., Swanson, G., Tupper, A., Volentik, A., and Waythomas, C.F. (2009). A multidisciplinary effort to assign realistic source parameters to models of volcanic ash-cloud transport and dispersion during eruptions. *J. Volcanol. Geotherm. Res.* 186, 10–21. doi:10.1016/j.jvolgeores.2009.01.008

Mastin, L.G., Schwaiger, H., Schneider, D.J., Wallace, K.L., Schaefer, J., and Denlinger, R.P. (2013). Injection, transport, and deposition of tephra during event 5 at Redoubt Volcano, 23 March, 2009. *J. Volcanol.Geotherm. Res.* 259, 201–213. doi:10.1016/j.jvolgeores.2012.04.025

Mastin, L.G., Van Eaton, A.R., and Durant, A.J. (2016). Adjusting particle-size distributions to account for aggregation in tephra-deposit model forecasts. *Atmos. Chem. Phys.* 16, 9399–9420. doi:10.5194/acp-16-9399-2016

Matthias, V., Aulinger, A., Bieser, J., Cuesta, J., Geyer, B., Langmann, B., Serikov, I., Mattis, I., Minikin, A., Mona, L., Quante, M., Schumann, U., and Weinzierl, B. (2012). The ash dispersion over Europe during the Eyjafjallajökull eruption – Comparison of CMAQ simulations to remote sensing and air-borne in-situ observations. *Atmos. Env.* 48, 184–194. doi:10.1016/j.j.atmosenv.2011.06.077

Melnik, O., Barmin, A.A., Sparks, R.S.J. (2004). Dynamics of magma flow inside volcanic conduits with bubble overpressure buildup and gas loss through permeable magma. *J. Volcanol. Geotherm. Res.*, 143, 53–68

Metrich, N., and Rutherford, M.J. (1998). Low pressure crystallization paths of H_2O-saturated basaltic-hawaiitic melts from Mt. Etna: Implications for open-system degassing volcanoes. *Geochim. Cosmochim. Acta.* 62, 1195–1205. doi:10.1016/S0016-7037(98)00048-9

Metrich, N., Allard, P., Spilliaert, N., Andronico, D., and Burton, M. (2004). 2001 flank eruption of the alkali- and volatile-rich primitive basalt responsible for Mount Etna's evolution in the last three decades. *Earth Planet. Sci. Lett.* 228, 1–17. doi:10.1016/ j.epsl.2004.09.036

Montopoli, M. (2016). Velocity profiles inside volcanic clouds from three-dimensional scanning microwave dual-polarization Doppler radars. *J. Geophys. Res. Atmos.* 121. doi:10.1002/2015JD023464

References

Morton, B.R., Taylor, G.I., and Turner, J.S. (1956). Turbulent gravitational convection from maintained and instantaneous source. Phil. Trans. *Royal Society*, London, A 234, 1–23

Mueller, S.B., Kueppers, U., Ayris, P.M., Jacob, M., and Dingwell, D.B. (2016). Experimental volcanic ash aggregation: Internal structuring of accretionary lapilli and the role of liquid bonding. *Earth and Planetary Sci. Lett.* 433, 232–240. doi:10.1016/j.epsl.2015.11.007

Mueller, S.B., Ayris, P.M., Wadsworth, F.B., Kueppers, U., Casas, A.S., Delmelle, P., Taddeucci, J., Jacob, M., and Dingwell, D.B. (2017a). Ash aggregation enhanced by deposition and redistribution of salt on the surface of volcanic ash in eruption plumes. *Nature comm. – Sci. Rep.* 7, 45762. doi:10.1038/srep45762

Mueller, S.B., Kueppers, U., Ametsbichler, J., Cimarelli, C., Merrison, J.P., Poret, M., Wadsworth, F.B., and Dingwell, D.B. (2017b). Stability of volcanic ash aggregates and break-up processes. *Nature comm. – Sci. Rep.* 7, 7440. doi:10.1038/s41598-017-07927-w

Muerdter, D.R., Dauphin, J.P. and Steele, G. (1981). An interactive computerised system for grain size analysis of silt using electro-resistance. *J. Sediment. Petrol.* 51, 647–650

O'Neill, N.T., Eck, T.F., Smirnov, A., Holben, B.N., and Thulasiraman, S. (2003). Spectral discrimination of coarse and fine mode optical depth. *J. Geophys. Res.* 108, 4559

Park, R.J., Jacob, D.J., Field, B.D., Yantosca, R.M, and Chin, M. (2004). Natural and transboundary pollution influences on sulfate-nitrate-ammonium aerosols in the United States: Implications for policy. *J. Geophys. Res.*, 109, D15204. doi:10.1029/2003JD004473

Pavolonis, M.J., Feltz, W.F., Heidinger, A.K., and Gallina, G.M. (2006). A daytime complement to the reverse absorption technique for improved automated detection of volcanic ash. *J. Atmos. Ocean. Technol.* 23 (11), 1422. doi:10.1175/JTECH1926.1

Pfeiffer, T., Costa, A., and Macedonio, G. (2005). A model for the numerical simulation of tephra fall deposits. *J. Volcanol. Geotherm. Res.* 140, 273–294. doi:10.1016/j.jvolgeores.2004.09.001

Pielke, R.A., Cotton, W.R., Walko, R.L., Tremback, C.J., Nicholls, M.E., Moran, M.D., Wesley, D.A., Lee, T.J., and Copeland, J.H. (1992). A comprehensive meteorological modelling system-RAMS. *Meteor. Atmos. Phys.* 49, 69–91

Pompilio, M., Bertagnini, A., Del Carlo, P., and Di Roberto, A. (2017). Magma dynamics within a basaltic conduit revealed by textural and compositional features of erupted ash: the December 2015 Mt. Etna paroxysms. *Nature comm. – Sci. Rep.* 7, 4805. doi:10.1038/s41598-017-05065-x

Poret, M., Costa, A., Andronico, D., and Scollo, S. (2015). Quantification of the volume and the total-grain-size distribution of the 23rd February 2013 Etna lava fountain. 26th *IUGG General Assembly*, Prague, Poster

Poret, M., Costa, A., Folch, A., and Martì, A. (2017). Modelling tephra dispersal and ash aggregation: The 26th April 1979 eruption, La Soufrière St. Vincent. *J. Volcanol. Geotherm. Res.* 347, 207–220. doi:10.1016/j.jvolgeores.2017.09.012

Poret, M., Corradini, S., Merucci, L., Costa, A., Andronico, D., Montopoli, M., Vulpiani, G., Freret-Lorgeril, V. (2018). Reconstructing volcanic plume evolution integrating satellite, and ground-based data: Application to the 23rd November 2013 Etna eruption. *Atmos. Chem. and Phys. Discuss., In press*. doi:10.5194/acp-2017-1146

References

Poret, M., Costa, A., Andronico, D., Scollo, S., Gouhier, M., and Cristaldi, A. Modelling eruption source parameters by integrating field, ground-based and satellite-based measurements: The case of the 23rd February 2013 Etna paroxysm. *J. Geophys. Res. – Solid Earth, Accepted pending revision*

Potts, R.J., and Ebert, E.E. (1996). On the detection of volcanic ash in NOAA AVHRR infrared satellite imagery. Paper Presented at 8th *Australian Remote Sens*. Conf. Canberra, 25–29

Prata, A.J. (1989a). Observations of volcanic ash clouds in the 10-12 μm window using AVHRR/2 data. *Int. J. Remote Sensing* 10, n°4-5, 751–761

Prata, A.J. (1989b). Radiative transfer calculations for volcanic ash clouds. *Geophys. Res. Lett.* 16 (11), 1293–1296, doi:10.1029/GL016i011p01293

Prata, A.J., and Grant, I.F. (2001). Retrieval of microphysical and morphological properties of volcanic ash plumes from satellite data: Application to Mt Ruapehu, New Zealand. *Q. J. R. Meteorol. Soc.* 127, 2153–2179

Prata, A.J., and Kerkmann, J. (2007). Simultaneous retrieval of volcanic ash and SO2 using MSGSEVIRI measurements. *Geophys. Res. Lett.* 34, L05813, doi:10.1029/2006GL0228691

Pyle, D.M. (1989). The thickness, volume and grainsize of the tephra fall deposits. *Bull. Volcanol.* 51, 1–15

Robock, A. (2000). Volcanic eruptions and climate. *Reviews of Geophys.* 38, 2, 191–219, 1998RG000054

Rodgers, C.D. (2000). Inverse Methods for Atmospheric Sounding: Theory and Practice, *World Scientific Pub Co Inc*., Singapore, 2000.

Rose, W.I., Bluth, G.J.S., Schneider, D.J., Ernst, G.G.J., Riley, C.M., Henderson, L.J., McGimsey, R.G. (2001). Observations of volcanic clouds in their first few days of atmospheric residence: The 1992 eruptions of Crater Peak, Mount Spurr Volcano, Alaska. *J. Geol.* 109(6), 677–694. doi:10.1086/323189

Rose, W.I., Riley, C.M., and Dartevelle, S. (2003). Sizes and shapes of 10-Ma distal fall pyroclasts in the Ogallala Group, Nebraska. *J. Geol.* 111(1), 115–124. doi:10.1086/344668

Rose, W.I., and Durant, A.J. (2009). Fine ash content of explosive eruptions. J. Volcanol. Geoth. Res. doi:10.1016/j.jvolgeores.2009.01.010

Schwaiger, H.F., Denlinger, R.P, and Mastin, L.G. (2012). Ash3d: A finite-volume, conservative numerical model for ash transport and tephra deposition. *J. Geophys. Res.* 117, B04204. doi:10.1029/2011JB008968

Scollo, S., Folch, A., and Costa, A. (2008). A parametric and comparative study of different tephra fallout models. *J. Volcanol. Geoth. Res.* 176, 199–211. doi:10.1016/j.jvolgeores.2008.04.002

Scollo, S., Prestifilippo, M., Spata, G., D'Agostino, M., and Coltelli, M. (2009). Monitoring and forecasting Etna volcanic plumes. *Nat. Hazards Earth Syst. Sci.* 9, 1573–1585

Scollo, S., Boselli, A., Coltelli, M., Leto, G., Pisani, G., Spinelli, N., and Wang, X. (2012). Monitoring Etna volcanic plumes using a scanning LiDAR. *Bull. Volcanol.* doi:10.1007/s00445-012-0669-y

Scollo, S., Coltelli, M., Bonadonna, C., and Del Carlo, P. (2013). Tephra hazard assessment at Mt. Etna (Italy). *Nat. Hazards Earth Syst. Sci. Discuss.* 1, 2945–2981. doi:10.5194/nhessd-1-2945-2013

References

Scollo, S., Prestifilippo, M., Pecora, E., Corradini, S., Merucci, L., Spata, G., and Coltelli, M. (2014). Eruption column height estimation of the 2011-2013 Etna lava fountains. *Annals of Geophys.* 57, 2, S0214. doi:10.4401/ag-6396

Scollo, S., Boselli, A., Coltelli, M., Leto, G., Pisani, G., Prestifilippo, M., Spinelli, N., and Wang, X. (2015). Volcanic ash concentration during the 12 August 2011 Etna eruption, *Geophys. Res. Lett.*, 42. doi:10.1002/2015GL063027

Searcy, C., Dean, K., and Stringer, W. (1998). PUFF: a high-resolution volcanic ash tracking model. *J. Volcanol. Geoth. Res.* 80, 1–16

Shepherd, J.B., and Sigurdsson, H. (1982). Mechanism of the 1979 explosive eruption of Soufriere volcano, St. Vincent. *J. Volcanol. Geotherm. Res.* 13, 1–2, 119-130. doi:10.1016/0377-0273(82)90023-3

Sič, B., El Amraoui, L., Marécal, V., Josse, B., Arteta, J., Guth, J., Joly, M., and Hamer, P.D. (2015). Modelling of primary aerosols in the chemical transport model MOCAGE: development and evaluation of aerosol physical parameterizations. *Geosci. Model. Dev.* 8, 381–408. doi:10.5194/gmd-8-381-2015

Skamarock, W.C., Klemp, J.B., Dudhia, J., Gill, D.O., Barker, D.M., Duda, M.G., Huang, X.Y., Wang, W., and Powers, J.G. (2008). A description of the advanced research WRF version 3, NCAR *technical note*, NCAR/TN–475+ STR

Smoluchowski, M. (1917). Veruch einer mathematischen Theorie der Koagulationkinetic kolloider Lösungen, Z. *Phys. Chem.* 92, 128–168

Spanu, A., Vitturi, M.M., and Barsotti, S. (2016). Reconstructing eruptive source parameters from tephra deposit: a numerical study of medium-sized explosive eruptions at Etna volcano. *Bull. Volcanol.* 78, 59. doi:10.1007/s00445-016-1051-2

Sparks, R.S.J., Bursik, M.I., Ablay, G., Thomas, R.M.E., and Carey, S.N. (1992). Sedimentation of tephra by volcanic plumes: part 2. Controls on thickness and grain-size variations of tephra fall deposits. *Bull Volcanol.* 54, 685–695

Spilliaert, N., Allard, P., Metrich, N., and Sobolev, A.V. (2006). Melt inclusion record of the conditions of ascent, degassing, and extrusion of volatile-rich alkali basalt during the powerful 2002 flank eruption of Mount Etna (Italy). *J. Geophys. Res.* 111, B04203. doi:10.1029/2005JB003934

Steppeler, J., Doms, G., Schättler, U., Bitzer, H.W., Gassmann, A., Damrath, U., Gregoric, G. (2003). Meso-gamma scale forecasts using the nonhydrostatic model LM. *Meteorol. Atmos. Phys.* 82, 75–96. doi:10.1007/s00703-001-0592-9

Stevenson, J.A., Millington, S.C., Beckett, F.M., Swindles, G.T., and Thordarson, T. (2015). Big grains go far: understanding the discrepancy between tephrochronology and satellite infrared measurements of volcanic ash. *Atmos. Meas. Tech.*, *8*(5), 2069–2091

Stohl, A., Hittenberger, M., and Wotawa, G. (1998). Validation of the Lagrangian particle dispersion model FLEXPART against large-scale tracer experiment data. *Atmos. Env.* 32, 24, 4245–4264

Stohl, A., Forster, C., Franck, A., Seibert, P., and Wotawa, G. (2005). Technical note: The Lagrangian particle dispersion model FLEXPART version 6.2. *Atmos. Chem. Phys.* 5, 2461–2474

References

Stunder, B., Heffter, J.L., and Draxler, R.R. (2007). Airborne volcanic ash forecast area reliability. *Weather and Forecasting* 22, 1132–1139

Sulpizio, R., Folch, A., Costa, A., Scaini, C., and Dellino, P. (2012). Hazard assessment of far-range volcanic ash dispersal from a violent Strombolian eruption at Somma-Vesuvius volcano, Naples, Italy: Implications on civil aviation, *Bull. Volcanol.* 74, 2205–2218. doi:10.1007/s00445-012-0656-3

Suzuki, T. (1983). A theoretical model for dispersion of tephra. *Arc Volcanism: Phys. & Tect.*, Shimozuru, D. and Yokohama, I. Eds, 95–113

Suzuki, Y.J., and Koyaguchi, T. (2009). A three-dimensional numerical simulation of spreading umbrella clouds, *J. Geophys. Res.* 114, B03209. doi:10.1029/2007JB005369

Suzuki, Y.J., and Koyaguchi, T. (2015). Effects of wind on entrainment efficiency in volcanic plumes. *J. Geophys. Res. – Solid Earth* 120, 6122–6140. doi:10.1002/2015JB012208

Taddeucci, J., Scarlato, P., Montanaro, C., Cimarelli, C., Del Bello, E., Freda, C., Andronico, D., Gudmundsson, M.T., and Dingwell, D.B. (2011). Aggregation-dominated ash settling from the Eyjafjallajökull volcanic cloud illuminated by field and laboratory high-speed imaging. *Geology* 39, n°9, 891–894. doi:10.1130/G32016.1

Taylor, M., Kazadzis, S., and Gerasopoulos, E. (2014). Multi-modal analysis of aerosol robotic network size distributions for remote-sensing applications: dominant aerosol type cases. *Atmos. Meas. Tech.* 7, 839–858. doi:10.5194/atm-7-839-2014

Tomašek, I., Horwell, C.J., Damby, D.E., Barošová, H., Geers, C., Petri-Fink, A., Rothen-Rutishauser, B., and Clift, M.J.D. (2016). Combined exposure of diesel exhaust particles and respirable Soufrière Hills volcanic ash causes a (pro-)inflammatory response in an in vitro multicellular epithelial tissue barrier model. *Particle and Fibre Toxicology* 13 (1), 67. doi:10.1186/s12989-016-0178-9

Twomey, S. (1996). Introduction to the Mathematics of Inversion in Remote Sensing and Indirect Measurements, *Dover Publications*, New York

Ulke, A.G. (2000). New turbulent parameterization for a dispersion model in atmospheric boundary layer. *Atmos. Env.* 34, 1029–1042

Van Eaton, A.R., Muirhead, J.D., Wilson, C.J.N., and Cimarelli, C. (2012). Growth of volcanic ash aggregates in the presence of liquid water and ice: an experimental approach. *Bull. Volcanol.* 74, 1963–1984. doi:10.1007/s00445-012-0634-9

Van Eaton, A.R., and Wilson, C.J.N. (2013). The nature, origins and distribution of ash aggregates in a large-scale wet eruption deposit: Oruanui, New Zealand. *J. Volcanol. Geoth. Res.* 250, 129–154. doi:10.1016/jvolgeores.2012.10.016

Vulpiani, G., Ripepe, M., and Valade, S. (2016). Mass discharge rate retrieval combining weather radar and thermal camera observations. *J. Geophys. Res. – Solid Earth* 121, 5679–5695. doi:10.1002/2016JB013191

Walker, G.P.L. (1971). Grain-size characteristics of pyroclastic deposits. *J. Geol.* 79, 696–714

Walker, G.P.L. (1973). Explosive volcanic eruptions – a new classification scheme. *Geologische Rundschau*, 62, 2, 431–446

References

Walker, G.P.L. (1980). The Taupo pumice: product of the most powerful known (ultra-Plinian) eruption? *J. Volcanol. Geoth. Res.* 8, 69–94

Watkin, S.C. (2003). The application of AVHRR data for the detection of volcanic ash in a Volcanic Ash Advisory Centre. *Meteorol. Appl.* 10, 301–311. doi:10.1017/S1350482703001063

Watson, I.M., and Oppenheimer, C. (2001). Photometric observations of Mt. Etna's different aerosol plumes. *Atmos. Env.* 35, 3561–3572

Watson, I.M., Realmuto, V.J., Rose, W.I., Prata, A.J., Bluth, G.J.S., Gu, Y., Bader, C.E., and Yu, T. (2004). Thermal infrared remote sensing of volcanic emissions using the moderate resolution imaging spectroradiometer. J. Volcanol. Geoterm. Res. 135, 75–89. doi:10.1016/j.jvolgeores.2003.12.017

Watt, S.F.L., Gilbert, J.S., Folch, A., and Phillips, J.C. (2015). An example of enhanced tephra deposition driven by topographic induced atmospheric turbulence. *Bull. Volcanol.* 77, 35. doi:10.1007/s00445-015-0927-x

Webley, P.W., Dean, K., Peterson, R., Steffke, A., Harrild, M., and Groves, J. (2012). Dispersion modelling of volcanic ash clouds: North Pacific eruptions, the past 40 years: 1970–2010. *Nat. Hazards* 61, 661–671. doi:10.1007/s11069-011-0053-9

Wen, S., and Rose, W.I. (1994). Retrieval of sizes and total masses of particles in volcanic clouds using AVHRR bands 4 and 5. *J. Geophys. Res*. 99 (D3), 5421–5431. doi:10.1029/93JD03340

Wikimedia Commons: https://commons.wikimedia.org/wiki/File:Vulcanian_Eruption-numbers.svg

Wilkins, K.L., Watson, I.M., Kristiansen, N.I., Webster, H.N., Thomson, D.J., Dacre, H.F., and Prata, A.J. (2016). Using data insertion with the NAME model to simulate the 8 May 2010 Eyjafjallajökull volcanic ash cloud. *J. Geophys. Res. Atmos.* 121, 306–323. doi:10.1002/2015JD023895

Wilson, L., and Walker, G.P.L. (1987). Explosive volcanic eruptions – VI. Ejecta dispersal in plinian eruptions: the control of eruption conditions and atmospheric properties. *Geophys. J. R. Astr. Soc.* 89, 657–679

Wilson, T., Cole, J., Cronin, S., Stewart, C., Johnston, D. (2011). Impacts on agriculture following the 1991 eruption of Vulcan Hudson, Patagonia: lessons for recovery. *Nat. Hazards* 57(2), 185–212

Wilson, T., Stewart, C., Sword-Daniels, V., Leonard, G., Johnston, D. Cole, J., Wardman, J., Wilson, G., and Bernard, S. (2012). Volcanic ash impacts on critical infrastructure. *Phys. Chem. Earth* Parts A/B/C, 45–46, 5–23

Witham, C.S., Hort, M.C., Potts, R., Servranckx, R., Husson, P., and Bonnardot, F. (2007). Comparison of VAAC atmospheric dispersion models using the 1 November 2004 Grimsvötn eruption. *Meteorol. Appl.* 14, 27–38. doi:10.1002/met.3

Wolke, R., Hellmuth, O., Knoth, O., Schröder, W., Heinrich, B., and Renner, E. (2004). The Chemistry-Transport Modelling System lm-Muscat: Description and citydelta Applications. [In: Borrego, C., and Incecik, S. (Eds) *Air Pollution Modelling and Its Application* XVI.] Springer, Boston, MA. doi:10.1007/978-1-4419-8867-6

Woodhouse, M.J., Hogg, A.J., Phillips, J.C., and Sparks, R.S.J. (2013). Interaction between volcanic plumes and wind during the 2010 Eyjafjallajökull eruption, Iceland. *J. Geophys. Res. – Solid Earth*, 118, 92–109. doi:10.1029/2012JB009592